First Run II Measurement of the W Boson Mass

T. Aaltonen,[23] A. Abulencia,[24] J. Adelman,[13] T. Akimoto,[54] M.G. Albrow,[17] B. Álvarez González,[11]
S. Amerio,[42] D. Amidei,[34] A. Anastassov,[51] A. Annovi,[19] J. Antos,[14] G. Apollinari,[17] A. Apresyan,[47]
T. Arisawa,[56] A. Artikov,[15] W. Ashmanskas,[17] A. Attal,[3] A. Aurisano,[52] F. Azfar,[41] P. Azzi-Bacchetta,[42]
P. Azzurri,[45] N. Bacchetta,[42] W. Badgett,[17] A. Barbaro-Galtieri,[28] V.E. Barnes,[47] B.A. Barnett,[25]
S. Baroiant,[7] V. Bartsch,[30] G. Bauer,[32] P.-H. Beauchemin,[33] F. Bedeschi,[45] P. Bednar,[14] S. Behari,[25]
G. Bellettini,[45] J. Bellinger,[58] A. Belloni,[32] D. Benjamin,[16] A. Beretvas,[17] J. Beringer,[28] T. Berry,[29]
A. Bhatti,[49] M. Binkley,[17] D. Bisello,[42] I. Bizjak,[30] R.E. Blair,[2] C. Blocker,[6] B. Blumenfeld,[25] A. Bocci,[16]
A. Bodek,[48] V. Boisvert,[48] G. Bolla,[47] A. Bolshov,[32] D. Bortoletto,[47] J. Boudreau,[46] A. Boveia,[10]
B. Brau,[10] L. Brigliadori,[5] C. Bromberg,[35] E. Brubaker,[13] J. Budagov,[15] H.S. Budd,[48] S. Budd,[24]
K. Burkett,[17] G. Busetto,[42] P. Bussey,[21] A. Buzatu,[33] K. L. Byrum,[2] S. Cabrera[r],[16] M. Campanelli,[35]
M. Campbell,[34] F. Canelli,[17] A. Canepa,[44] D. Carlsmith,[58] R. Carosi,[45] S. Carrillo[l],[18] S. Carron,[33]
B. Casal,[11] M. Casarsa,[17] A. Castro,[5] P. Catastini,[45] D. Cauz,[53] M. Cavalli-Sforza,[3] A. Cerri,[28]
L. Cerrito[p],[30] S.H. Chang,[27] Y.C. Chen,[1] M. Chertok,[7] G. Chiarelli,[45] G. Chlachidze,[17] F. Chlebana,[17]
K. Cho,[27] D. Chokheli,[15] J.P. Chou,[22] G. Choudalakis,[32] S.H. Chuang,[51] K. Chung,[12] W.H. Chung,[58]
Y.S. Chung,[48] C.I. Ciobanu,[24] M.A. Ciocci,[45] A. Clark,[20] D. Clark,[6] G. Compostella,[42] M.E. Convery,[17]
J. Conway,[7] B. Cooper,[30] K. Copic,[34] M. Cordelli,[19] G. Cortiana,[42] F. Crescioli,[45] C. Cuenca Almenar[r],[7]
J. Cuevas[o],[11] R. Culbertson,[17] J.C. Cully,[34] D. Dagenhart,[17] M. Datta,[17] T. Davies,[21] P. de Barbaro,[48]
S. De Cecco,[50] A. Deisher,[28] G. De Lentdecker[d],[48] G. De Lorenzo,[3] M. Dell'Orso,[45] L. Demortier,[49]
J. Deng,[16] M. Deninno,[5] D. De Pedis,[50] P.F. Derwent,[17] G.P. Di Giovanni,[43] C. Dionisi,[50] B. Di Ruzza,[53]
J.R. Dittmann,[4] M. D'Onofrio,[3] S. Donati,[45] P. Dong,[8] J. Donini,[42] T. Dorigo,[42] S. Dube,[51] J. Efron,[38]
R. Erbacher,[7] D. Errede,[24] S. Errede,[24] R. Eusebi,[17] H.C. Fang,[28] S. Farrington,[29] W.T. Fedorko,[13]
R.G. Feild,[59] M. Feindt,[26] J.P. Fernandez,[31] C. Ferrazza,[45] R. Field,[18] G. Flanagan,[47] R. Forrest,[7]
S. Forrester,[7] M. Franklin,[22] J.C. Freeman,[28] I. Furic,[18] M. Gallinaro,[49] J. Galyardt,[12] F. Garberson,[10]
J.E. Garcia,[45] A.F. Garfinkel,[47] H. Gerberich,[24] D. Gerdes,[34] S. Giagu,[50] P. Giannetti,[45] K. Gibson,[46]
J.L. Gimmell,[48] C. Ginsburg,[17] N. Giokaris[a],[15] M. Giordani,[53] P. Giromini,[19] M. Giunta,[45] V. Glagolev,[15]
D. Glenzinski,[17] M. Gold,[36] N. Goldschmidt,[18] J. Goldstein[c],[41] A. Golossanov,[17] G. Gomez,[11]
G. Gomez-Ceballos,[32] M. Goncharov,[52] O. González,[31] I. Gorelov,[36] A.T. Goshaw,[16] K. Goulianos,[49]
A. Gresele,[42] S. Grinstein,[22] C. Grosso-Pilcher,[13] R.C. Group,[17] U. Grundler,[24] J. Guimaraes da Costa,[22]
Z. Gunay-Unalan,[35] C. Haber,[28] K. Hahn,[32] S.R. Hahn,[17] E. Halkiadakis,[51] A. Hamilton,[20] B.-Y. Han,[48]
J.Y. Han,[48] R. Handler,[58] F. Happacher,[19] K. Hara,[54] D. Hare,[51] M. Hare,[55] S. Harper,[41] R.F. Harr,[57]
R.M. Harris,[17] M. Hartz,[46] K. Hatakeyama,[49] J. Hauser,[8] C. Hays,[41] M. Heck,[26] A. Heijboer,[44]
B. Heinemann,[28] J. Heinrich,[44] C. Henderson,[32] M. Herndon,[58] J. Heuser,[26] S. Hewamanage,[4] D. Hidas,[16]
C.S. Hill[c],[10] D. Hirschbuehl,[26] A. Hocker,[17] S. Hou,[1] M. Houlden,[29] S.-C. Hsu,[9] B.T. Huffman,[41]
R.E. Hughes,[38] U. Husemann,[59] J. Huston,[35] J. Incandela,[10] G. Introzzi,[45] M. Iori,[50] A. Ivanov,[7]
B. Iyutin,[32] E. James,[17] B. Jayatilaka,[16] D. Jeans,[50] E.J. Jeon,[27] S. Jindariani,[18] W. Johnson,[7] M. Jones,[47]
K.K. Joo,[27] S.Y. Jun,[12] J.E. Jung,[27] T.R. Junk,[24] T. Kamon,[52] D. Kar,[18] P.E. Karchin,[57] Y. Kato,[40]
R. Kephart,[17] U. Kerzel,[26] V. Khotilovich,[52] B. Kilminster,[38] D.H. Kim,[27] H.S. Kim,[27] J.E. Kim,[27]
M.J. Kim,[17] S.B. Kim,[27] S.H. Kim,[54] Y.K. Kim,[13] N. Kimura,[54] L. Kirsch,[6] S. Klimenko,[18] M. Klute,[32]
B. Knuteson,[32] B.R. Ko,[16] S.A. Koay,[10] K. Kondo,[56] D.J. Kong,[27] J. Konigsberg,[18] A. Korytov,[18]
A.V. Kotwal,[16] J. Kraus,[24] M. Kreps,[26] J. Kroll,[44] N. Krumnack,[4] M. Kruse,[16] V. Krutelyov,[10] T. Kubo,[54]
S. E. Kuhlmann,[2] T. Kuhr,[26] N.P. Kulkarni,[57] Y. Kusakabe,[56] S. Kwang,[13] A.T. Laasanen,[47] S. Lai,[33]
S. Lami,[45] S. Lammel,[17] M. Lancaster,[30] R.L. Lander,[7] K. Lannon,[38] A. Lath,[51] G. Latino,[45] I. Lazzizzera,[42]
T. LeCompte,[2] J. Lee,[48] J. Lee,[27] Y.J. Lee,[27] S.W. Lee[q],[52] R. Lefèvre,[20] N. Leonardo,[32] S. Leone,[45]
S. Levy,[13] J.D. Lewis,[17] C. Lin,[59] C.S. Lin,[17] M. Lindgren,[17] E. Lipeles,[9] T.M. Liss,[24] A. Lister,[7]
D.O. Litvintsev,[17] T. Liu,[17] N.S. Lockyer,[44] A. Loginov,[59] M. Loreti,[42] L. Lovas,[14] R.-S. Lu,[1] D. Lucchesi,[42]
J. Lueck,[26] C. Luci,[50] P. Lujan,[28] P. Lukens,[17] G. Lungu,[18] L. Lyons,[41] J. Lys,[28] R. Lysak,[14] E. Lytken,[47]
P. Mack,[26] D. MacQueen,[33] R. Madrak,[17] K. Maeshima,[17] K. Makhoul,[32] T. Maki,[23] P. Maksimovic,[25]
S. Malde,[41] S. Malik,[30] G. Manca,[29] A. Manousakis[a],[15] F. Margaroli,[47] C. Marino,[26] C.P. Marino,[24]

A. Martin,[59] M. Martin,[25] V. Martin[j],[21] M. Martínez,[3] R. Martínez-Ballarín,[31] T. Maruyama,[54]
P. Mastrandrea,[50] T. Masubuchi,[54] M.E. Mattson,[57] P. Mazzanti,[5] K.S. McFarland,[48] P. McIntyre,[52]
R. McNulty[i],[29] A. Mehta,[29] P. Mehtala,[23] S. Menzemer[k],[11] A. Menzione,[45] P. Merkel,[47] C. Mesropian,[49]
A. Messina,[35] T. Miao,[17] N. Miladinovic,[6] J. Miles,[32] R. Miller,[35] C. Mills,[22] M. Milnik,[26] A. Mitra,[1]
G. Mitselmakher,[18] H. Miyake,[54] S. Moed,[20] N. Moggi,[5] C.S. Moon,[27] R. Moore,[17] M. Morello,[45]
P. Movilla Fernandez,[28] J. Mülmenstädt,[28] A. Mukherjee,[17] Th. Muller,[26] R. Mumford,[25] P. Murat,[17]
M. Mussini,[5] J. Nachtman,[17] Y. Nagai,[54] A. Nagano,[54] J. Naganoma,[56] K. Nakamura,[54] I. Nakano,[39]
A. Napier,[55] V. Necula,[16] C. Neu,[44] M.S. Neubauer,[24] J. Nielsen[f],[28] L. Nodulman,[2] M. Norman,[9]
O. Norniella,[24] E. Nurse,[30] S.H. Oh,[16] Y.D. Oh,[27] I. Oksuzian,[18] T. Okusawa,[40] R. Oldeman,[29] R. Orava,[23]
K. Osterberg,[23] S. Pagan Griso,[42] C. Pagliarone,[45] E. Palencia,[17] V. Papadimitriou,[17] A. Papaikonomou,[26]
A.A. Paramonov,[13] B. Parks,[38] S. Pashapour,[33] J. Patrick,[17] G. Pauletta,[53] M. Paulini,[12] C. Paus,[32]
D.E. Pellett,[7] A. Penzo,[53] T.J. Phillips,[16] G. Piacentino,[45] J. Piedra,[43] L. Pinera,[18] K. Pitts,[24] C. Plager,[8]
L. Pondrom,[58] X. Portell,[3] O. Poukhov,[15] N. Pounder,[41] F. Prakoshyn,[15] A. Pronko,[17] J. Proudfoot,[2]
F. Ptohos[h],[17] G. Punzi,[45] J. Pursley,[58] J. Rademacker[c],[41] A. Rahaman,[46] V. Ramakrishnan,[58] N. Ranjan,[47]
I. Redondo,[31] B. Reisert,[17] V. Rekovic,[36] P. Renton,[41] M. Rescigno,[50] S. Richter,[26] F. Rimondi,[5]
L. Ristori,[45] A. Robson,[21] T. Rodrigo,[11] E. Rogers,[24] S. Rolli,[55] R. Roser,[17] M. Rossi,[53] R. Rossin,[10]
P. Roy,[33] A. Ruiz,[11] J. Russ,[12] V. Rusu,[17] H. Saarikko,[23] A. Safonov,[52] W.K. Sakumoto,[48] G. Salamanna,[50]
O. Saltó,[3] L. Santi,[53] S. Sarkar,[50] L. Sartori,[45] K. Sato,[17] P. Savard,[33] A. Savoy-Navarro,[43] T. Scheidle,[26]
P. Schlabach,[17] E.E. Schmidt,[17] M.P. Schmidt,[59] M. Schmitt,[37] T. Schwarz,[7] L. Scodellaro,[11] A.L. Scott,[10]
A. Scribano,[45] F. Scuri,[45] A. Sedov,[47] S. Seidel,[36] Y. Seiya,[40] A. Semenov,[15] L. Sexton-Kennedy,[17]
A. Sfyrla,[20] S.Z. Shalhout,[57] M.D. Shapiro,[28] T. Shears,[29] P.F. Shepard,[46] D. Sherman,[22] M. Shimojima[n],[54]
M. Shochet,[13] Y. Shon,[58] I. Shreyber,[20] A. Sidoti,[45] P. Sinervo,[33] A. Sisakyan,[15] A.J. Slaughter,[17]
J. Slaunwhite,[38] K. Sliwa,[55] J.R. Smith,[7] F.D. Snider,[17] R. Snihur,[33] M. Soderberg,[34] A. Soha,[7]
S. Somalwar,[51] V. Sorin,[35] J. Spalding,[17] F. Spinella,[45] T. Spreitzer,[33] P. Squillacioti,[45] M. Stanitzki,[59]
R. St. Denis,[21] B. Stelzer,[8] O. Stelzer-Chilton,[41] D. Stentz,[37] J. Strologas,[36] D. Stuart,[10] J.S. Suh,[27]
A. Sukhanov,[18] H. Sun,[55] I. Suslov,[15] T. Suzuki,[54] A. Taffard[e],[24] R. Takashima,[39] Y. Takeuchi,[54]
R. Tanaka,[39] M. Tecchio,[34] P.K. Teng,[1] K. Terashi,[49] J. Thom[g],[17] A.S. Thompson,[21] G.A. Thompson,[24]
E. Thomson,[44] P. Tipton,[59] V. Tiwari,[12] S. Tkaczyk,[17] D. Toback,[52] S. Tokar,[14] K. Tollefson,[35]
T. Tomura,[54] D. Tonelli,[17] S. Torre,[19] D. Torretta,[17] S. Tourneur,[43] W. Trischuk,[33] Y. Tu,[44] N. Turini,[45]
F. Ukegawa,[54] S. Uozumi,[54] S. Vallecorsa,[20] N. van Remortel,[23] A. Varganov,[34] E. Vataga,[36] F. Vázquez[l],[18]
G. Velev,[17] C. Vellidis[a],[45] V. Veszpremi,[47] M. Vidal,[31] R. Vidal,[17] I. Vila,[11] R. Vilar,[11] T. Vine,[30]
M. Vogel,[36] I. Volobouev[q],[28] G. Volpi,[45] F. Würthwein,[9] P. Wagner,[44] R.G. Wagner,[2] R.L. Wagner,[17]
J. Wagner,[26] W. Wagner,[26] R. Wallny,[8] S.M. Wang,[1] A. Warburton,[33] D. Waters,[30] M. Weinberger,[52]
W.C. Wester III,[17] B. Whitehouse,[55] D. Whiteson[e],[44] A.B. Wicklund,[2] E. Wicklund,[17] G. Williams,[33]
H.H. Williams,[44] P. Wilson,[17] B.L. Winer,[38] P. Wittich[g],[17] S. Wolbers,[17] C. Wolfe,[13] T. Wright,[34] X. Wu,[20]
S.M. Wynne,[29] A. Yagil,[9] K. Yamamoto,[40] J. Yamaoka,[51] T. Yamashita,[39] C. Yang,[59] U.K. Yang[m],[13]
Y.C. Yang,[27] W.M. Yao,[28] G.P. Yeh,[17] J. Yoh,[17] K. Yorita,[13] T. Yoshida,[40] G.B. Yu,[48] I. Yu,[27]
S.S. Yu,[17] J.C. Yun,[17] L. Zanello,[50] A. Zanetti,[53] I. Zaw,[22] X. Zhang,[24] Y. Zheng[b],[8] and S. Zucchelli[5]
(CDF Collaboration[*])

[1]*Institute of Physics, Academia Sinica, Taipei, Taiwan 11529, Republic of China*
[2]*Argonne National Laboratory, Argonne, Illinois 60439*
[3]*Institut de Fisica d'Altes Energies, Universitat Autonoma de Barcelona, E-08193, Bellaterra (Barcelona), Spain*
[4]*Baylor University, Waco, Texas 76798*
[5]*Istituto Nazionale di Fisica Nucleare, University of Bologna, I-40127 Bologna, Italy*
[6]*Brandeis University, Waltham, Massachusetts 02254*
[7]*University of California, Davis, Davis, California 95616*
[8]*University of California, Los Angeles, Los Angeles, California 90024*
[9]*University of California, San Diego, La Jolla, California 92093*
[10]*University of California, Santa Barbara, Santa Barbara, California 93106*
[11]*Instituto de Fisica de Cantabria, CSIC-University of Cantabria, 39005 Santander, Spain*
[12]*Carnegie Mellon University, Pittsburgh, PA 15213*
[13]*Enrico Fermi Institute, University of Chicago, Chicago, Illinois 60637*

[14] *Comenius University, 842 48 Bratislava, Slovakia; Institute of Experimental Physics, 040 01 Kosice, Slovakia*
[15] *Joint Institute for Nuclear Research, RU-141980 Dubna, Russia*
[16] *Duke University, Durham, North Carolina 27708*
[17] *Fermi National Accelerator Laboratory, Batavia, Illinois 60510*
[18] *University of Florida, Gainesville, Florida 32611*
[19] *Laboratori Nazionali di Frascati, Istituto Nazionale di Fisica Nucleare, I-00044 Frascati, Italy*
[20] *University of Geneva, CH-1211 Geneva 4, Switzerland*
[21] *Glasgow University, Glasgow G12 8QQ, United Kingdom*
[22] *Harvard University, Cambridge, Massachusetts 02138*
[23] *Division of High Energy Physics, Department of Physics,*
University of Helsinki and Helsinki Institute of Physics, FIN-00014, Helsinki, Finland
[24] *University of Illinois, Urbana, Illinois 61801*
[25] *The Johns Hopkins University, Baltimore, Maryland 21218*
[26] *Institut für Experimentelle Kernphysik, Universität Karlsruhe, 76128 Karlsruhe, Germany*
[27] *Center for High Energy Physics: Kyungpook National University,*
Taegu 702-701, Korea; Seoul National University, Seoul 151-742,
Korea; SungKyunKwan University, Suwon 440-746,
Korea; Korea Institute of Science and Technology Information, Daejeon,
305-806, Korea; Chonnam National University, Gwangju, 500-757, Korea
[28] *Ernest Orlando Lawrence Berkeley National Laboratory, Berkeley, California 94720*
[29] *University of Liverpool, Liverpool L69 7ZE, United Kingdom*
[30] *University College London, London WC1E 6BT, United Kingdom*
[31] *Centro de Investigaciones Energeticas Medioambientales y Tecnologicas, E-28040 Madrid, Spain*
[32] *Massachusetts Institute of Technology, Cambridge, Massachusetts 02139*
[33] *Institute of Particle Physics: McGill University, Montréal,*
Canada H3A 2T8; and University of Toronto, Toronto, Canada M5S 1A7
[34] *University of Michigan, Ann Arbor, Michigan 48109*
[35] *Michigan State University, East Lansing, Michigan 48824*
[36] *University of New Mexico, Albuquerque, New Mexico 87131*
[37] *Northwestern University, Evanston, Illinois 60208*
[38] *The Ohio State University, Columbus, Ohio 43210*
[39] *Okayama University, Okayama 700-8530, Japan*
[40] *Osaka City University, Osaka 588, Japan*
[41] *University of Oxford, Oxford OX1 3RH, United Kingdom*
[42] *University of Padova, Istituto Nazionale di Fisica Nucleare,*
Sezione di Padova-Trento, I-35131 Padova, Italy
[43] *LPNHE, Universite Pierre et Marie Curie/IN2P3-CNRS, UMR7585, Paris, F-75252 France*
[44] *University of Pennsylvania, Philadelphia, Pennsylvania 19104*
[45] *Istituto Nazionale di Fisica Nucleare Pisa, Universities of Pisa,*
Siena and Scuola Normale Superiore, I-56127 Pisa, Italy
[46] *University of Pittsburgh, Pittsburgh, Pennsylvania 15260*
[47] *Purdue University, West Lafayette, Indiana 47907*
[48] *University of Rochester, Rochester, New York 14627*
[49] *The Rockefeller University, New York, New York 10021*
[50] *Istituto Nazionale di Fisica Nucleare, Sezione di Roma 1,*
University of Rome "La Sapienza," I-00185 Roma, Italy
[51] *Rutgers University, Piscataway, New Jersey 08855*
[52] *Texas A&M University, College Station, Texas 77843*
[53] *Istituto Nazionale di Fisica Nucleare, University of Trieste/ Udine, Italy*
[54] *University of Tsukuba, Tsukuba, Ibaraki 305, Japan*
[55] *Tufts University, Medford, Massachusetts 02155*
[56] *Waseda University, Tokyo 169, Japan*
[57] *Wayne State University, Detroit, Michigan 48201*
[58] *University of Wisconsin, Madison, Wisconsin 53706*
[59] *Yale University, New Haven, Connecticut 06520*

We describe a measurement of the W boson mass m_W using 200 pb^{-1} of $\sqrt{s}$=1.96 TeV $p\bar{p}$ collision data taken with the CDF II detector. With a sample of 63,964 $W \to e\nu$ candidates and 51,128 $W \to \mu\nu$ candidates, we measure $m_W = [80.413 \pm 0.034(\text{stat}) \pm 0.034(\text{sys}) = 80.413 \pm 0.048]$ GeV/c^2. This is the single most precise m_W measurement to date. When combined with other

measured electroweak parameters, this result further constrains the properties of new unobserved particles coupling to W and Z bosons.

PACS numbers: 13.38.Be, 14.70.Fm, 13.85.Qk, 12.15.Ji

I. INTRODUCTION

The discovery of the W and Z bosons in 1983 [1] confirmed a central prediction of the unified model of electromagnetic and weak interactions [2]. Initial W and Z boson mass measurements verified the tree-level predictions of the theory, with subsequent measurements probing the predicted $\mathcal{O}(3 \text{ GeV}/c^2)$ [3, 4] radiative corrections to the masses. The current knowledge of these masses and other electroweak parameters constrains additional radiative corrections from unobserved particles such as the Higgs boson or supersymmetric particles. These constraints are however limited by the precision of the W boson mass m_W, making improved measurements of m_W a high priority in probing the masses and electroweak couplings of new hypothetical particles. We describe in this article the single most precise m_W measurement [5] to date.

The W boson mass can be written in terms of other precisely measured parameters in the "on-shell" scheme as [4]:

$$m_W^2 = \frac{\hbar^3}{c} \frac{\pi \alpha_{EM}}{\sqrt{2} G_F (1 - m_W^2/m_Z^2)(1 - \Delta r)}, \quad (1)$$

where α_{EM} is the electromagnetic coupling at the renormalization energy scale $Q = m_Z c^2$, G_F is the Fermi weak coupling extracted from the muon lifetime, m_Z is the Z boson mass, and Δr includes all radiative corrections. Fermionic loop corrections increase the W boson mass by terms proportional to

$\ln(m_Z/m_f)$ for $m_f \ll m_Z$ [4], while the loop containing top and bottom quarks (Fig. 1) increases m_W according to [6]:

$$\Delta r_{tb} = \frac{c}{\hbar^3} \frac{-3 G_F m_W^2}{8\sqrt{2}\pi^2 (m_Z^2 - m_W^2)} \times \left[m_t^2 + m_b^2 - \frac{2 m_t^2 m_b^2}{m_t^2 - m_b^2} \ln(m_t^2/m_b^2) \right],$$
$$(2)$$

where the second and third terms can be neglected since $m_t \gg m_b$. Higgs loops (Fig. 2) decrease m_W with a contribution proportional to the logarithm of the Higgs mass (m_H). Contributions from possible supersymmetric particles are dominated by squark loops (Fig. 3) and tend to increase m_W. Generally, the lighter the squark masses and the larger the squark weak doublet mass splitting, the larger the contribution to m_W. The total radiative correction from supersymmetric particles can be as large as several hundred MeV/c^2 [7].

Table I [8] shows the change in m_W for $+1\sigma$ changes in the measured standard model input parameters and the effect of doubling m_H from 100 GeV/c^2 to 200 GeV/c^2. In addition to the listed parameters, a variation of ± 1.7 MeV/c^2 on the predicted m_W arises from two-loop sensitivity to α_s, e.g. via gluon exchange in the quark loop in Fig. 1. Theoretical corrections beyond second order, which have yet to be calculated, are estimated to affect the m_W prediction by ± 4 MeV/c^2 [8].

*With visitors from [a]University of Athens, 15784 Athens, Greece, [b]Chinese Academy of Sciences, Beijing 100864, China, [c]University of Bristol, Bristol BS8 1TL, United Kingdom, [d]University Libre de Bruxelles, B-1050 Brussels, Belgium, [e]University of California, Irvine, Irvine, CA 92697, [f]University of California Santa Cruz, Santa Cruz, CA 95064, [g]Cornell University, Ithaca, NY 14853, [h]University of Cyprus, Nicosia CY-1678, Cyprus, [i]University College Dublin, Dublin 4, Ireland, [j]University of Edinburgh, Edinburgh EH9 3JZ, United Kingdom, [k]University of Heidelberg, D-69120 Heidelberg, Germany, [l]Universidad Iberoamericana, Mexico D.F., Mexico, [m]University of Manchester, Manchester M13 9PL, England, [n]Nagasaki Institute of Applied Science, Nagasaki, Japan, [o]University de Oviedo, E-33007 Oviedo, Spain, [p]Queen Mary's College, University of London, London, E1 4NS, England, [q]Texas Tech University, Lubbock, TX 79409, [r]IFIC(CSIC-Universitat de Valencia), 46071 Valencia, Spain,
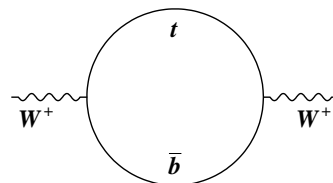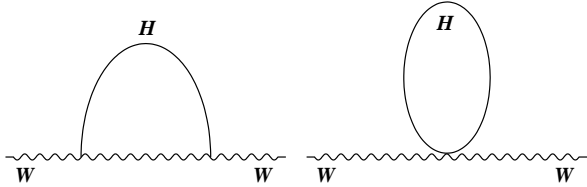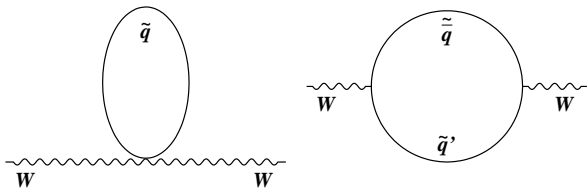
FIG. 1: The one-loop contribution to the W boson mass from top and bottom quarks.

The uncertainties on the m_W prediction can be compared to the 29 MeV/c^2 uncertainty on the world average from direct m_W measurements (Table II),

H **H**

W **W** **W** **W**

FIG. 2: Higgs one-loop contributions to the W boson mass.

$\tilde{q}$ $\tilde{\tilde{q}}$

W **W** $\tilde{q}'$

W **W**

FIG. 3: One-loop squark contributions to the W boson mass.

Parameter Shift	m_W Shift (MeV/c^2)
$\Delta \ln m_H = +0.693$	-41.3
$\Delta m_t = +1.8$ GeV/c^2 [9]	11.0
$\Delta \alpha_{EM}(Q = m_Z c^2) = +0.00035$ [10]	-6.2
$\Delta m_Z = +2.1$ MeV/c^2 [11]	2.6

TABLE I: The effect on m_W of $+1\sigma$ increases of the input parameters dominating the uncertainty on the m_W prediction. Since the Higgs boson has not been observed, we show the effect of doubling the Higgs boson mass from 100 GeV/c^2 to 200 GeV/c^2 [8].

Experiment	m_W (GeV/c^2)
ALEPH [12]	80.440 ± 0.051
OPAL [13]	80.416 ± 0.053
L3 [14]	80.270 ± 0.055
DELPHI [15]	80.336 ± 0.067
CDF Run I [16]	80.433 ± 0.079
DØ Run I [17, 18]	80.483 ± 0.084
LEP Average [19]	80.376 ± 0.033
Tevatron Run I Average [20]	80.456 ± 0.059
World Average	80.392 ± 0.029

TABLE II: Direct measurements of the W boson mass, the preliminary combined LEP average, the combined Tevatron Run I average, and the preliminary world average.

which include results from four experiments, ALEPH [12], DELPHI [15], L3 [14], and OPAL [13], studying $\sqrt{s} = 161 - 209$ GeV e^+e^- collisions at the Large Electron Positron collider (LEP), and from two experiments, CDF [16] and DØ [17, 18], studying $\sqrt{s} = 1.8$ TeV $p\bar{p}$ collisions in Run I of the Fermilab Tevatron. The current experimental m_W uncertainty is a factor of two larger than the uncertainty from radiative corrections, excluding the Higgs contribution (Table I). The Higgs mass constraint extracted from the W boson mass is thus limited by the direct m_W measurement. The precise m_W measurement described in this article has a significant impact on the world average m_W.

The leptonic decays of singly produced Z bosons provide important control samples, since both leptons from Z boson decay are well measured. The production and decay uncertainties on the measurement of m_W from $p\bar{p}$ and e^+e^- collider data are almost completely independent [22].

We present in this Section an overview of W and Z boson production at the Tevatron, a description of the coordinate definitions and symbol conventions used for this measurement, and a broad discussion of our m_W measurement strategy.

II. OVERVIEW

A measurement of m_W at a $p\bar{p}$ collider [21] is complementary to that at an e^+e^- collider. Individual u (d) quarks inside the proton can interact with $\bar{d}$ ($\bar{u}$) quarks inside the anti-proton (or vice versa), allowing single W^+ (W^-) boson production, which is not possible at an e^+e^- collider. In addition, $p\bar{p}$ colliders have higher center of mass energies and W boson production cross sections. This provides high statistics for the leptonic decays of the W boson, which are studied exclusively because of the overwhelming hadronic-jet background in the quark decay channels.

A. W and Z Boson Production and Decay

W and Z bosons are produced in $\sqrt{s} = 1.96$ TeV $p\bar{p}$ collisions primarily through $s-$channel annihilation of valence u and/or d quarks (Fig. 4), with a smaller O(20%) contribution from sea quarks. The quark (antiquark) has a fraction x_p ($x_{\bar{p}}$) of the pro-

ton's (antiproton's) total momentum, producing a W or Z boson at center of mass energy $\sqrt{\hat{s}} \equiv Q$ equal to its mass times c^2. The rate of production can be predicted from two components: (1) the momentum fraction distributions of the quarks, $f_q(x, Q^2)$, which are determined from fits to world data [23, 24]; and (2) a perturbative calculation of the $q\bar{q}' \to W$ or Z boson process [25].
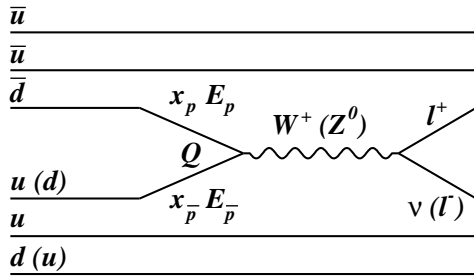

FIG. 4: Leading-order annihilation of a quark and antiquark inside the proton and antiproton, respectively, producing a W^+ or Z^0 boson. The quark (antiquark) has energy $x_p E_p$ ($x_{\bar{p}} E_{\bar{p}}$), where E_p ($E_{\bar{p}}$) represents the total proton (antiproton) energy. The production occurs at a partonic center-of-mass energy Q. The $u\bar{u} \to Z^0$ and $d\bar{u} \to W^-$ processes are similar.

W and Z bosons can decay to lepton or quark pairs. Decays to quark pairs are not observable given the large direct $q\bar{q}'$ background, and decays to $\tau \to \nu_\tau$+hadrons are not as precisely measured as boson decays to electrons or muons. For these reasons we restrict ourselves to the direct electronic and muonic decays ($W \to e\nu$, $W \to \mu\nu$, $Z \to ee$, and $Z \to \mu\mu$), with the corresponding decays to $\tau \to$ leptons considered as backgrounds to these processes (Section VIII). The branching ratio for each leptonic decay $W \to l\nu$ ($Z \to ll$) is $\approx 11\%$ (3.3%), and the measured cross section times branching ratio is (2749 ± 174) pb [(254.9 ± 16.2) pb] [26].

B. Conventions

We use both Cartesian and cylindrical coordinate systems, in which $+z$ points in the direction of the proton beam (east) and the origin is at the center of the detector. In the right-handed Cartesian coordinate system, $+x$ points north (outward from the ring) and $+y$ points upwards; in the cylindrical system, ϕ is the azimuthal angle and r is the radius from the center of the detector in the $x - y$ plane. The rapidity $y = -\frac{1}{2} \ln[(E - p_z c)/(E + p_z c)]$ is additive
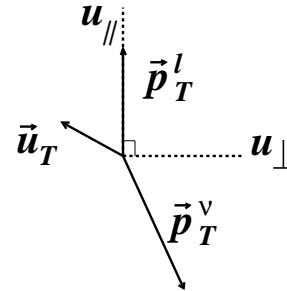

FIG. 5: A W boson event, with the recoil hadron momentum ($\vec{u}_T$) separated into axes parallel ($u_{||}$) and perpendicular ($u_\perp$) to the charged lepton.

under Lorentz boosts along the z axis. For massless particles, this quantity is equal to the pseudorapidity $\eta = -\ln[\tan(\theta/2)]$, where θ is the polar angle with respect to the z axis. All angles are quoted in radians unless otherwise indicated.

Because the interacting quarks' longitudinal momenta p_z are not known for each event, we generally work with momenta transverse to the beam line. The interacting protons and antiprotons have no net transverse momentum. Electron energy (muon momentum) measured using the calorimeter (tracker) is denoted as E ($\vec{p}$), and the corresponding transverse momenta $\vec{p}_T$ are derived using the measured track direction and neglecting particle masses. The event calorimetric $\vec{p}_T$, excluding the lepton(s), is calculated assuming massless particles using calorimeter tower energies (Section III A 2) and the lepton production vertex, and provides a measurement of the recoil momentum vector $\vec{u}_T$. The component of recoil projected along the lepton direction is denoted $u_{||}$ and the orthogonal component is $u_\perp$ (Fig. 5). The transverse momentum imbalance in a W boson event is a measure of the neutrino transverse momentum $\vec{p}_T^\nu$ and is given by $\vec{p}_T = -(\vec{p}_T^l + \vec{u}_T)$, where $\vec{p}_T^l$ is the measured charged lepton transverse momentum.

When electromagnetic charge is not indicated, both charges are considered. We use units where $\hbar = c \equiv 1$ for the remainder of this paper.

C. Measurement Strategy

The measurement of the final state from $W \to l\nu$ decays involves a measurement of $\vec{p}_T^l$ and the total recoil $\vec{u}_T$. The neutrino escapes detection and the unknown initial partonic p_z precludes the use of p_z conservation in the measurement. The boson invariant mass is thus not reconstructable; rather, the 2-

dimensional "transverse mass" m_T is used in the m_W fit:

$$m_T = \sqrt{2 p_T^l \not{p}_T \left(1 - \cos \Delta\phi\right)}, \qquad (3)$$

where $\Delta\phi$ is the angle in the transverse plane between the leptons, whose masses are negligible. The fit to the m_T distribution provides the statistically most precise measurement of m_W.

The charged lepton, which can be measured precisely, carries most of the observable mass information in the event. We calibrate the muon momentum using high statistics samples of the meson decays $J/\psi \to \mu\mu$ and $\Upsilon \to \mu\mu$, which are fully reconstructable and have well known masses. This results in a precise track momentum calibration, which we transfer to the calorimeter with a fit to the ratio of calorimeter energy to track momentum (E/p) of electrons from W boson decays. The accuracy of these calibrations is demonstrated by applying them to measurements of the Z boson mass in the muon and electron decay channels. We then incorporate the known Z boson mass as an additional calibration constraint.

The other directly measurable quantity needed for the calculation of m_T is the recoil transverse momentum $\vec{u}_T$. Since the W and Z bosons are produced at a similar Q^2, they have similar recoil distributions. We use the leptons from the Z boson decay to measure the p_T of the Z boson. We then calibrate our model of $\vec{u}_T$ by measuring the balance between the recoil and Z boson $\vec{p}_T$. The Z boson statistics are sufficient to perform a recoil calibration to 1% accuracy, which leads to a systematic uncertainty commensurate with other uncertainties on m_W.

To accurately model the shape of the m_T distribution, we use a fast Monte Carlo simulation of the $p\bar{p} \to W \to l\nu$ process including the recoil and the detector response. The custom fast simulation allows flexibility in parametrizing the detector response and in separating the effects of the detector model components. We use a binned likelihood to fit the measured m_T distributions to templates (Section II D) generated from the fast simulation, with m_W as the free parameter. All m_W and lepton energy scale fits are performed with this procedure.

Though less statistically precise, the p_T^l and $\not{p}_T$ distributions provide additional information on the W boson mass and are used as important tests of consistency. We separately fit these distributions for m_W and combine all fits in our final result.

During the measurement process, all W boson mass fits were offset by a single unknown random number chosen from a flat distribution in the range [-100,100] MeV. The fit result was thus blinded to the authors until the analysis was complete [27]. The final measured m_W and its uncertainty have not changed since the random offset was removed from the fit results.

We give a brief overview of the template likelihood fitting procedure in Section II D. Section III describes the detector and the fast detector simulation used in the analysis. The W boson measurement samples are defined in Section IV. We describe the precision measurements of muons and electrons in Sections V and VI, respectively. These sections include event selection, calibration, and resolution studies from the dilepton and W boson data samples. Measurement of the recoil response and resolution is presented in Section VII. The backgrounds to the W boson sample are discussed in Section VIII. Theoretical aspects of W and Z boson production and decay, including constraints from the current data sample, are described in Section IX. We present the W boson mass fits and cross-checks in Section X. Finally, in Section XI we show the result of combining our measurement with previous measurements, and the corresponding implications on the predicted standard model Higgs boson mass.

D. Template Likelihood Fits

All the fits involving mass measurements and the energy scale (Sections V, VI, and X) are performed with a template binned likelihood fitting procedure. A given distribution to be fit is generated as a discrete function of the fit parameter, using the fast simulation. These simulated distributions are referred to as "templates." For each value of the fit parameter, the simulated distribution is compared to the data distribution and the logarithm of a binned likelihood is calculated. The binned likelihood is the Poisson probability for each bin to contain the n_i observed data events given m_i expected events, multiplied over the N bins in the fit range:

$$\mathcal{L} = \prod_{i=1}^{N} \frac{e^{-m_i} m_i^{m_i}}{n_i!}. \qquad (4)$$

We calculate the logarithm of the likelihood using the approximation $\ln n! \approx (n + 1/2) \ln(n+1) - n$:

$$\ln \mathcal{L} \approx \sum_{i=1}^{N} [n_i \ln m_i - m_i - (n_i + 1/2) \ln(n_i + 1) + n_i].$$
$$(5)$$

The best-fit value of the parameter maximizes the likelihood (or equivalently minimizes $-\ln \mathcal{L}$), and the $\pm 1\sigma$ values are those that increase $-\ln \mathcal{L}$ by 1/2. The

approximation for $\ln n!$ only affects the shape of the likelihood about the minimum and not the position of the minimum. The procedure is validated by fitting simulated data ("pseudoexperiments") and no bias is found. We symmetrize the uncertainty by taking half the difference between the $+1\sigma$ and -1σ values. For the E/p fits in the W boson sample, we reduce the effect of finite template statistics by fitting $-\ln\mathcal{L}$ to a parabola, and extracting the best-fit value and the uncertainty from this parabola.

III. DETECTOR AND MODEL

The CDF II detector [26, 28] is well suited for the m_W measurement. Its high-resolution tracker and calorimeter measure individual charged lepton momenta from W and Z boson decays with a resolution of $\approx 2\%$. It has similar acceptance and resolution for central electrons and muons, giving the two channels similar weight in a combined mass measurement.

A. Detector Components

The CDF II detector (Fig. 6) is a multi-purpose detector consisting of: an inner silicon tracker designed to measure the production vertex of charged particles with high precision; an outer tracking drift chamber to measure charged particle momenta; a solenoid to provide a uniform 1.4 T magnetic field inside the trackers; electromagnetic calorimeters to contain and measure electron and photon showers; hadronic calorimeters for hadron energy measurements; and a muon system to detect muons escaping the calorimeters. The detector information is read out on-line and saved for later analysis when event topologies consistent with a particular physics process (or class of processes) are selected. The read-out decision is made with a fast three-level trigger system that has high efficiency for selecting the W and Z bosons to be used in the offline analysis.

1. Tracking System

The silicon tracker (Fig. 7) consists of three separate detectors: Layer 00, SVX II, and ISL. Layer 00 is a single layer of 300 μm thick sensors attached to the beam pipe at a radius of 1.3 cm. Five additional layers of sensors at radii ranging from 2.5 cm to 10.6 cm comprise SVX II. Surrounding these sensors are port cards, which transport deposited charge information

from the silicon wafers to the readout system. The intermediate silicon layers (ISL) are located at radii of 20.2 cm and 29.1 cm. The SVX II is segmented longitudinally into three barrels in the region $|z| < 45$ cm. This covers the $p\bar{p}$ interaction region, which is well approximated by a Gaussian distribution with $\sigma_z \approx 30$ cm. We do not use the silicon measurements in this analysis, though we model the tracker's effects on leptons and photons (Section III B).

An open-cell drift chamber, the central outer tracker (COT) [29], surrounds the silicon tracker and covers the region $|z| < 155$ cm ($|\eta| \lesssim 1$) and 40 cm $< r <$ 137 cm. The COT consists of eight concentric 'superlayers,' separated azimuthally into cells. Each cell contains 12 sense wires to measure the ionization produced by a charged particle in the ambient argon-ethane gas mixture. The superlayers alternate between a purely axial configuration, with sense wires parallel to the beam line, and a small-angle stereo configuration, with sense wires at a $2°$ angle relative to the z axis.

The sense wires are strung from end to end in z and held under tension at each aluminum endplate (Fig. 8). The wires are azimuthally sandwiched by field sheets, which provide a 1.9 kV/cm electric field. All cells are rotated at a $35°$ angle relative to a radial line, such that the ionized electrons travel approximately azimuthally to the wire under the combined influence of the local electric field and the global magnetic field from the solenoid.

Within a given cell the sense wires are slightly off-center relative to the field sheets. In addition, the sense wires and field sheets sag under the influence of gravity, with the field sheets sagging more due to their larger masses. These effects cause a small electrostatic deflection of the sense wires toward a particular field sheet. To prevent the relative deflection of sense wires within a cell, a support rod connects the sense wires at the center of the detector. The support rod results in a small (≈ 2 mm) region at $z = 0$ cm where charged particles are not measured.

Between the solenoid and the COT is a time-of-flight system (TOF) consisting of scintillator bars that precisely measure the time of incidence of charged particles. From this measurement and the tracker information, a particle's velocity and mass can be inferred. The TOF is not utilized in this analysis.

2. Calorimeter System

The CDF calorimeter is segmented radially into electromagnetic and hadronic sections. The central
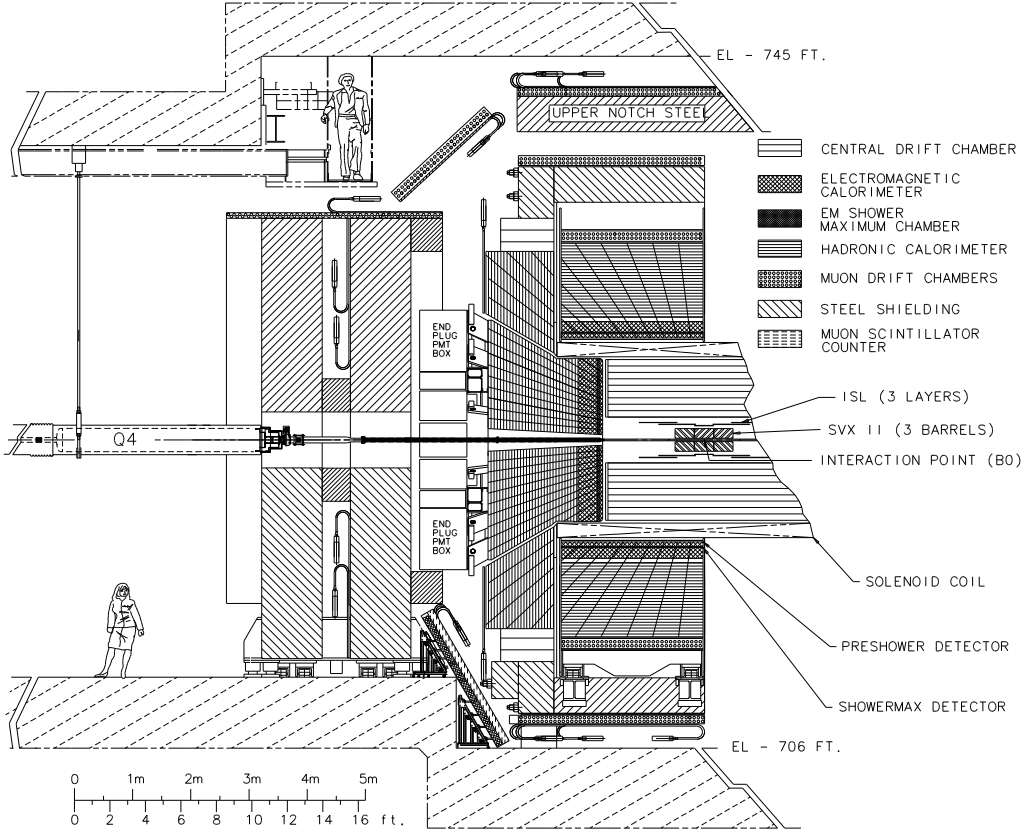
FIG. 6: A cut-away view of a section of the CDF detector. The slice is along the y-axis at $x = 0$ cm.

calorimeter covers $|\eta| < 1.1$ and is split at the center into two separate barrels covering $+\eta$ and $-\eta$. Each barrel consists of 24 azimuthal "wedges" of size 0.26 radians (15°) with ten projective towers of size $\Delta\eta \approx 0.11$. To allow a pathway for the solenoid cryogenic tubes, a two-tower region is removed, corresponding to $0.77 < \eta < 1.0$, $75° < \phi < 90°$, and $z > 193$ cm. The forward calorimeter covers $1.1 < |\eta| < 3.6$, filling the forward gaps with a plug shape (Fig. 6).

The central electromagnetic calorimeter (CEM) [30] has a thickness of 18 radiation lengths, consisting of 31 radial scintillator layers interleaved with 30 layers of lead-aluminum plates. At a radius of 184 cm electromagnetic showers have traversed about six radiation lengths (including the solenoidal coil) and have their maximum energy deposition. At this radius finely segmented strip and wire chambers (CES) measure the energy deposition with a position resolution of ≈ 2 mm.

The local shower position in the azimuthal direction in the tower is denoted as CES x, which ranges from -24.1 cm to 24.1 cm. The wire chambers extend only to $|x| \leq 22.5$ cm, and for $|x| > 23.1$ cm no energy measurements are made. In this region wavelength shifters read out the light from the scintillator, and steel and foam separate the towers. Light follows a waveguide to a phototube positioned at the back end of the hadronic calorimeter.

Parallel to the beam line, the position at shower maximum is denoted CES z. The strip chambers extend from 6-239 cm in $|z|$, and there is no scintillator for $|z| < 4.2$ cm, where the two calorimeter barrels meet.

The central hadronic calorimeter [31] is separated into a central region (CHA, $|\eta| < 0.6$) with 32 longitudinal layers of scintillator sandwiched with steel and a forward "wall" calorimeter (WHA, $0.6 < |\eta| < 1.1$) with 15 such layers. These calorimeters have thicknesses of ≈ 4.5 interaction lengths.

The plug calorimeter [32] has a comparable design to the central calorimeter with scintillator-lead electromagnetic calorimeters and scintillator-steel hadronic calorimeter compartments. The ϕ seg-
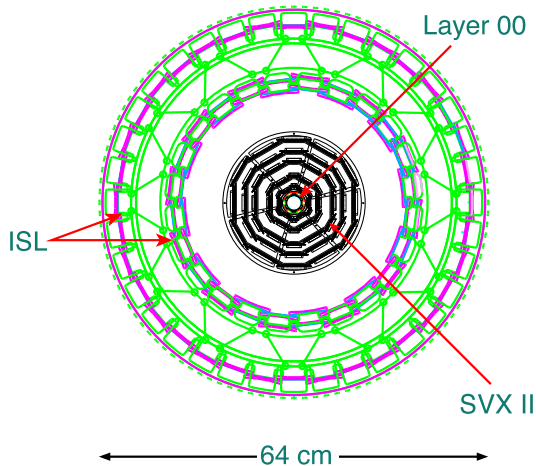
FIG. 7: End view of the silicon detector. The innermost layer (Layer 00) is attached to the beam pipe, and is surrounded by five concentric layers of silicon wafers (SVX II). The outermost layers are the intermediate silicon layers (ISL), which sit just inside the outer tracking chamber.

mentation is 0.13 radians up to $|\eta| = 2.1$, and then broadens to 0.26 radians. The two furthest forward plug towers cover the $|\eta|$ regions $2.6 - 3.0$ and $3.0 - 3.6$, while the remaining towers have a size $\Delta\eta = 0.1$.

3. Muon Detectors

The muon systems relevant for the W mass measurement cover the region $|\eta| \leq 1$. The central muon detector (CMU) and the central muon upgrade (CMP) cover $|\eta| \leq 0.6$, while the central muon extension (CMX) covers $0.6 < |\eta| \leq 1$.

The CMU detector [33] is located at the outer edge of the CHA, 347 cm from the z axis. The CMU is segmented into $15°$ azimuthal wedges containing four layers of proportional drift chambers that cover $12.6°$. The maximum drift time within a chamber is 800 ns, about twice as long as the 396 ns spacing between $p\bar{p}$ crossings. CMU information must therefore be combined with reconstructed COT particle tracks to determine the appropriate $p\bar{p}$ crossing.

Because the total thickness of the central calorimeter is about five interaction lengths, approximately 0.5% of high-momentum pions reach the CMU. To reduce this background, the CMP detector is located behind an additional 60 cm of steel. The CMP has a similar construction to the CMU, with the exception that wider drift chambers are used to cover the same solid angle, resulting in a maximum drift time

of 1.8 μs rather than 800 ns.

The CMX detector [34] consists of eight drift chamber layers beyond both the calorimeter and the steel detector support structure ($6 - 10$ interaction lengths). The CMX ϕ regions used in this analysis are $-45° < \phi < 75°$ and $105° < \phi < 225°$. New detectors for Run II cover much of the remaining ϕ region, but were not fully commissioned for the data-taking period of this analysis. Scintillator detectors (CSX) at the inner and outer surfaces of the CMX provide timing information to the trigger to separate collision particles from other sources such as beam halo or cosmic rays.

4. Trigger System

The trigger consists of three stages with progressively greater sophistication of event reconstruction. The first stage is hardware-based, the second a mix of hardware and software, and the third a farm of processors performing full event reconstruction.

The first trigger stage, level 1, includes tracker, calorimeter, and muon reconstruction. The charged particle track reconstruction is performed with the extremely fast tracker (XFT) [35] based on the four axial COT superlayers. A track segment is reconstructed in a given superlayer if at least 11 of the 12 sense wires [36] in a wide road have charge deposition above a given threshold ("hits"). The list of segments from the full tracker is compared to predefined groups of segments expected from charged particles above a given momentum threshold. When matches are found, track candidates are created and passed to the track extrapolator (XTRP) [37]. The XTRP determines the expected ϕ positions of the tracks in the calorimeter and muon detectors, for the purpose of forming electron and muon candidates.

The calorimeter reconstruction at level 1 defines separate electromagnetic and hadronic "trigger towers" as tower pairs adjacent in η. The tower p_T is calculated assuming a collision vertex $z = 0$ and an electron candidate is formed if the ratio of hadronic to electromagnetic energy (Had/EM) in a trigger tower is less than 1/8. The high-momentum electron trigger used in this analysis requires a level 1 trigger tower with electromagnetic $p_T > 8$ GeV matched to a track with $p_T > 8$ GeV, and drops the Had/EM requirement for electromagnetic $p_T > 14$ GeV.

Level 1 muon reconstruction includes a p_T estimate within the CMU and CMX chambers from the relative timing of the hits in different layers. The CMU track segments are combined with reconstructed CMP track segments to create "CMUP"
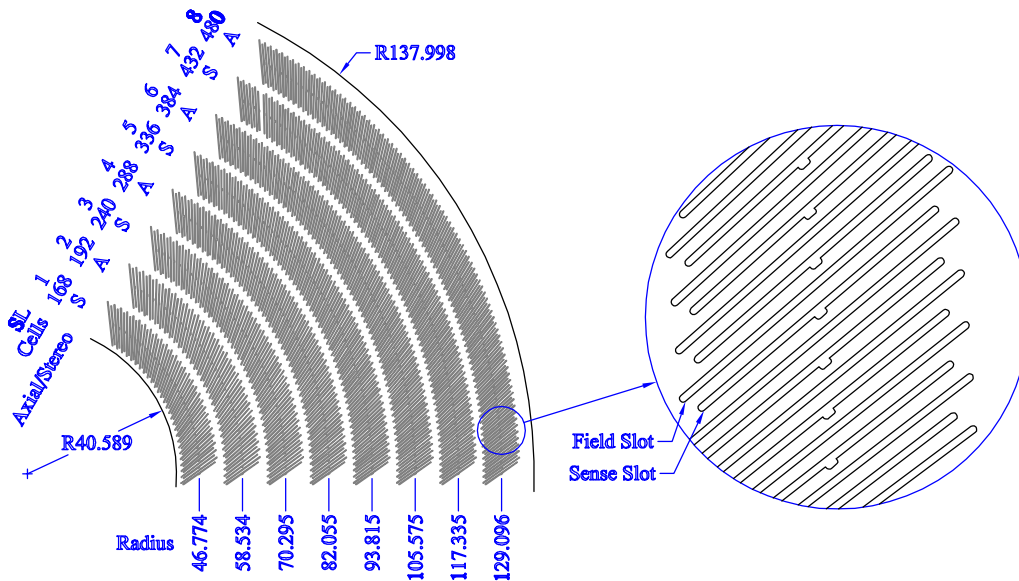
FIG. 8: End view of a section of a central outer tracker (COT) endplate. The COT consists of eight concentric 'superlayers,' separated azimuthally into cells, each containing 12 sense wires and sandwiched by field sheets. The endplates contain precision-machined slots where each cell's sense wires and field sheets are held under tension. The radius at the center of each superlayer is shown in cm.

muon candidates. For the majority of the data CMX candidates also require local CSX hits consistent with particles originating from the collision. For our W and Z boson samples we use a muon trigger that requires CMU or CMX $p_T > 6$ GeV matched to an XFT track with $p_T > 4$ GeV (CMUP) or $p_T > 8$ GeV (CMX).

The level 2 calorimeter reconstruction uses a more sophisticated clustering algorithm for electromagnetic objects. This improves energy measurement resolution and allows a higher threshold ($p_T > 16$ GeV) to be applied. To reduce rates, the XFT track requirement for CMUP candidates was raised to $p_T > 8$ GeV for most of the data-taking period.

At level 3, approximately 300 dual processor computers allow full track pattern recognition, muon reconstruction, and calorimeter clustering. Variables used to select electrons at level 3 are the lateral shower profile, L_{shr} (Section IV B), and the distance between CES z and the z-position of the track extrapolated to the CES (Δz). The L_{shr} variable quantifies the difference between the measured energies of towers neighboring the electron in η and the expected energies determined from electron test beam data. The trigger requirements of $L_{shr} < 0.4$ and $|\Delta z| < 8$ cm are $\approx 100\%$ efficient for electrons from W and Z boson decays. The high-momentum electron trigger

also requires electromagnetic $p_T > 18$ GeV and track $p_T > 9$ GeV. For efficiency studies we use a separate trigger that requires electromagnetic $p_T > 25$ GeV and $\not{p}_T^{L3} > 25$ GeV, but has no quality requirements at level 3 and no trigger track requirements. At level 3, $\vec{\not{p}}_T^{L3}$ is defined as the negative of the vector sum of the transverse momenta in all calorimeter towers. The high-momentum muon trigger requires a COT track with $p_T > 18$ GeV matched to a CMUP or CMX track segment.

5. Luminosity Detector

The small-angle Cherenkov luminosity counters (CLC) [38] are used to measure the instantaneous and integrated luminosity of our data samples. The CLC consists of two modules installed around the beampipe at each end of the detector, providing coverage in the regions $3.6 < |\eta| < 4.6$. Each module contains 48 conical gas Cherenkov counters pointing to the collision region. Signals in both CLC modules coinciding in time with the bunch crossing are used to measure the instantaneous luminosity and to trigger collision events. Events collected with this trigger, known as "minimum bias" events, are used to study the detector response to generic inelastic $p\bar{p}$ collisions

(Section VII).

B. Detector Model

We use a parametrized model of the detector response to electrons, muons, and the hadronic recoil. The model is incorporated into a custom fast simulation that includes lepton and recoil reconstruction, event selection, and fit template generation. The simulation provides both flexibility in determining the effects of various inputs, and computing speed to allow frequent high-statistics studies. A sample of $O(10^7)$ events can be generated using a single-processor machine in one day. This is several orders of magnitude more than the $O(10^3)$ events that can be produced with the standard GEANT-based CDF simulation [40] [41].

We describe in this section the simulation of electrons and muons. Fits to the data that determine the values of some of the model parameters are described in Secs. V and VI. The detector model of hadronic recoil response and resolution is discussed in Sec. VII.

The model components common to muons and electrons are: ionization energy loss and multiple scattering in the beam pipe and tracker volume; parametrized track hit resolutions and efficiencies; and track reconstruction. We describe these components in the muon simulation overview, and then discuss the electron- and photon-specific simulation.

1. Muon Simulation

Muon and electron tracks are reconstructed using only COT hit and beam position information (Section IV). Thus, the simulation of the silicon detector consists entirely of energy loss and multiple scattering. In the COT, hit resolutions and efficiencies are additionally simulated, and track reconstruction is performed. The total measured muon EM calorimeter energy is simulated by combining the minimum-ionizing energy deposition with energy from final-state photon radiation (Section IX D) and the recoil and underlying event [39]. Finally, the detector fiduciality of muons is calculated using a map of the muon detector geometry as a function of η and ϕ. The map is extracted from a full GEANT-based simulation of the CDF II detector [40, 41].

Ionization Energy Loss

The differential ionization energy loss of muons and electrons in the tracking system is simulated according to the Bethe-Bloch equation [11]:

$$-\frac{dE}{dx} = \frac{KZ}{A\beta^2}\left[\frac{1}{2}\ln\frac{2m_e\beta^2 T_{max}}{(1-\beta^2)I^2} - \beta^2 - \frac{\delta}{2}\right], \quad (6)$$

where $K = 4\pi N_A r_e^2 m_e$, N_A is Avogadro's number, r_e is the classical electron radius, $Z(A)$ is the atomic (mass) number, β is the particle velocity, I is the mean excitation energy, T_{max} is the maximum kinematic energy that can be transferred to a free electron in a single collision, and δ is the material-dependent density effect as a function of β [11]. When calculating the effect of δ, we take the material to be silicon throughout.

To calculate muon energy loss in the material upstream of the COT ($r < 40$ cm), we use a three-dimensional lookup table of the material properties of the beam pipe, the silicon detector, and the wall of the alumnium can at the inner radius of the COT. The lookup table determines the appropriate Z/A and I values, along with the radiation length X_0 (Appendix A), for each of 32 radial layers. Except for the inner and outer layers, the map is finely segmented longitudinally and in azimuth to capture the material variation in the silicon detector [42]. Inside the COT fiducial volume we calculate the energy loss between each of the 96 radial sense wires.

The energy loss model is tuned using the data. We apply a global correction factor of 0.94 to the calculated energy loss in the material upstream of the COT in order to obtain a $J/\psi \rightarrow \mu\mu$ mass measurement that is independent of the mean inverse momentum of the decay muons (Section V B 3).

Multiple Coulomb Scattering

Multiple Coulomb scattering in the beampipe, silicon detector, and COT affects the resolution of the reconstructed track parameters for low-momentum tracks. We model the scattering using a Gaussian distribution for 98% of the scatters [43] with an angular resolution σ_ϑ defined by

$$\sigma_\vartheta = \frac{13.6 \text{ MeV}}{\beta p}\sqrt{x/X_0}, \quad (7)$$

where x is the thickness of the layer and X_0 is the layer's radiation length (Section III B 2). Simulation of multiple scattering is implemented for each radial

layer of the three-dimensional lookup table and between each COT layer.

Based on the results of low-energy muon scattering data [44], we model the non-Gaussian wide-angle scatters by increasing σ_θ by a factor of 3.8 for 2% of the scatters.

COT Simulation and Reconstruction

The charged track measurement is modeled with a full hit-level simulation of the charge deposition in the COT and a helical track fit. The parameter resolution of reconstructed tracks is affected by the individual hit resolution, and by the distribution of the number of hits (N_{hit}) used in the fit [45].

We tune the COT hit resolution using the width of the $\Upsilon \rightarrow \mu\mu$ mass distribution reconstructed with non-beam-constrained tracks. The tuned value of $[150 \pm 3(\text{stat})]$ μm is consistent with the 149 μm RMS of the observed hit residual distribution for the muon tracks in $Z \rightarrow \mu\mu$ data. We use a 150 μm hit resolution for the simulation of the Υ, W, and Z bosons.

We use a dual-resolution model to describe the narrower mass peak in the high-statistics $J/\psi \rightarrow \mu\mu$ sample, where the muons generally have lower momenta than the other samples. The J/ψ mass peak width is particularly sensitive to multiple scattering and relative energy loss, and our hit-resolution model compensates for any mismodeling that affects the peak width. We find that a single-hit resolution of 155 μm applied to 70% of the tracks and 175 μm applied to the remaining 30% adequately describes the width and lineshape of the $J/\psi \rightarrow \mu\mu$ mass peak.

To describe the N_{hit} distribution, we use a dual-hit-efficiency model, the larger one applied to the majority of the tracks. The lower efficiency accounts for events with high COT occupancy, where fewer hits are attached to reconstructed tracks. The two parameters are tuned to match the mean and RMS of the data N_{hit} distributions. We independently tune these parameters for the J/ψ sample, the Υ sample, and the W and Z boson samples.

COT hit positions from a charged track are used to reconstruct a helix with a χ^2-minimization procedure. The axial helix parameters [46] are the impact parameter with respect to the nominal beam position, d_0, the azimuthal angle at the closest approach to the beam, ϕ_0, and the curvature of the track, c, defined to be $(2R)^{-1}$, where R is the radius of curvature. The stereo helix parameters are the longitudinal position at the closest approach to the beam, z_0, and the cotangent of the polar angle, $\cot\theta$.

When optimizing resolution of lepton tracks from prompt resonance decays, we constrain the helix to originate from the location of the beam. The transverse size of the beam is ≈ 30 μm at $z = 0$ cm and increases to $50 - 60$ μm at $|z| = 40$ cm [47]. For simplicity we assume an average beam size of $[39 \pm 3(\text{stat})]$ μm, which is determined from a fit to the width of the $Z \rightarrow \mu\mu$ mass peak. The beam constraint improves the intrinsic fractional momentum resolution by about a factor of three, to $\delta p_T/p_T \approx 0.0005$ p_T/GeV.

We perform a track fit on our simulated hits in the same manner as the data. The hits are first fit to a helix without a beam constraint; hits with large residuals (> 600 μm) are dropped from the track (in order to remove spurious hits added in data pattern recognition); and the track is fit again with an optional beam constraint. This option is applied to prompt lepton tracks from W and Z boson decays, but not to tracks from J/ψ decays, approximately 20% of which are not prompt. The prompt muons from Υ decays are fit twice, both with and without the beam constraint, as a consistency check.

Calorimeter Response

Muons deposit ionization energy in the calorimeter. We simulate a muon's EM energy deposition using a distribution taken from cosmic ray muons passing through the center of the detector, in events with no other track activity. An additional contribution comes from energy flow into the calorimeter from the underlying event [39]. We model this energy using a distribution taken from $W \rightarrow \mu\nu$ data events, using towers separated in azimuth from the muon.

Muons with a CES z position within 1.58 cm of a tower boundary typically deposit energy in two calorimeter towers. We use this criterion in the simulation to apply the underlying event and final-state photon radiation (Section IX D) contributions for one or two towers. The simulated underlying event energy includes its dependence on $u_{||}$ and $u_\perp$ (Fig. 5), and on the tower η position of the muon when it crosses the CES (Section VII B).

Detector Fiduciality

The CMUP and CMX muon systems do not have complete azimuthal or polar angle coverage. We create an $\eta - \phi$ map of each muon detector's coverage using muons simulated [41] with a detector geometry based on GEANT [40]. We use the map in the fast simulation to determine the fiduciality of a muon at

a given $\eta - \phi$ position.

We incorporate the relative efficiency of the CMUP to CMX triggers in the fast simulation by matching the ratio of CMUP to CMX events in the $W \to \mu\nu$ data (Section IV A).

2. Electron and Photon Simulation

The dominant calibration of the calorimeter energy measurement E of electrons uses their track momenta p and a fit to the peak of the E/p distribution. An additional calibration results from a mass fit to the Z boson resonance and reduces the calibration uncertainty by 20% relative to the E/p calibration alone.

The E/p method relies on an accurate modeling of radiative effects that reduce the track momentum measured in the COT. A given electron loses $\approx 20\%$ of its energy through bremsstrahlung radiation in the silicon detector, and this process has the most significant impact on the E/p calibration. The total amount of silicon detector material is tuned with data using highly radiative electrons (Section VI A). We additionally model processes that affect the shape of the E/p distribution: photon conversion in the tracker; energy loss in the solenoid and the time-of-flight system; electromagnetic calorimeter response and resolution; and energy loss into the hadronic calorimeter. The models of ionization energy loss and multiple scattering in the tracker, as well as the COT track simulation and reconstruction, are the same as for muons (Section III B 1).

Bremsstrahlung

The differential cross section for an electron of energy E_e to radiate a photon of energy E_γ is given by the screened Bethe-Heitler equation [48] over most of the $y \equiv E_\gamma/E_e$ spectrum. In terms of the material's radiation length X_0, the differential cross section for bremsstrahlung radiation is:

$$\frac{d\sigma}{dy} = \frac{A}{N_A X_0 \rho} \left[\left(\frac{4}{3} + C \right) \left(\frac{1}{y} - 1 \right) + y \right], \quad (8)$$

where C is a small material-dependent correction (Appendix A). Figure 9 shows the integrated thickness of material upstream of the COT, in terms of radiation lengths, traversed by the reconstructed electron tracks in $W \to e\nu$ data. The number of photons emitted per layer is given by:

$$N_\gamma = \frac{x}{X_0} \left[\left(\frac{4}{3} + C \right) (y_0 - \ln y_0 - 1) + \frac{1}{2} (1 - y_0)^2 \right], \quad (9)$$
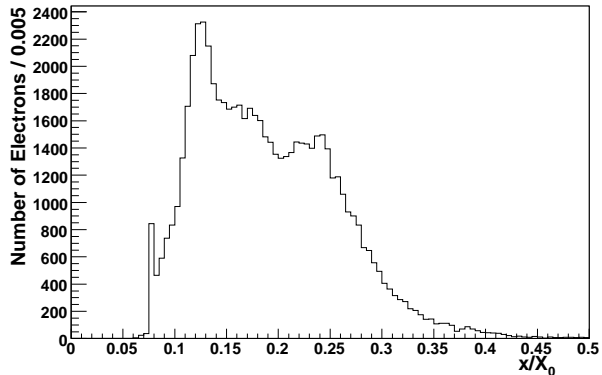
FIG. 9: The distribution of material upstream of the COT traversed by reconstructed electron trajectories in $W \to e\nu$ data events, in units of radiation lengths. The peaks at ≈ 0.08, ≈ 0.13, and ≈ 0.24 correspond respectively to trajectories outside the silicon detector ($|z| > 45$ cm), within the silicon detector, and crossing silicon barrels ($|z| \approx 15, 45$ cm). The mean of the distribution is 19%.

where x is the thickness of the layer and y_0 is a lower threshold introduced to avoid infrared divergences. We use $y_0 = 10^{-4}$ [49] and determine $C = 0.0253$ using the silicon atomic number $Z = 14$.

For each layer of the silicon or COT material, we use a Poisson distribution with mean N_γ to determine the number of photons radiated in that layer. For each radiated photon, we calculate y from the spectrum in Eq. (8). To correct for inaccuracies of the screened Bethe-Heitler equation at the ends of the y spectrum, we apply a suppression factor if $y \leq 0.005$ or $y \geq 0.8$.

For radiation of high-momentum photons ($y \gtrsim 0.8$), the approximation of complete screening of the nuclear electromagnetic field by the atomic electrons breaks down. In this region, the full Bethe-Heitler equation for incomplete screening [48] must be used. We implement this correction by removing generated photons in the high-y region such that we match the reduced cross section from incomplete screening.

Two effects reduce the cross section for low-momentum photon radiation [50]: multiple scattering and Compton scattering. Multiple Coulomb scattering suppresses long-distance interactions, and the resulting LPM suppression [51] in low-momentum radiation can be expressed in terms of the Bethe-Heitler cross section [52]:

$$S_{LPM} \equiv \frac{d\sigma_{LPM}/dy}{d\sigma_{BH}/dy} = \sqrt{\frac{E_{LPM}}{E_e} \frac{y}{(1-y)}}, \quad (10)$$

where E_{LPM} depends on the material. We use $E_{LPM} = 72$ TeV, appropriate for silicon, and apply the suppression when $S_{LPM} < 1$.

Radiated photons scatter off the atomic electrons, and destructive interference of low-momentum photons suppresses this radiation [53]. The suppression factor is:

$$S_{Compton} = \frac{y^2}{y^2 + E_p^2/E_e^2},\qquad (11)$$

where $E_p = \gamma\omega_p$ is 2.4 MeV for a 40 GeV electron in silicon, using the silicon plasma frequency ω_p, and γ is the Lorentz factor.

In any given simulated event, the product of S_{LPM} and $S_{Compton}$ provides the probability that a photon generated from the screened Bethe-Heitler equation with $y \leq 0.005$ survives the low-momentum suppression. For a 40 GeV electron radiating a 20 MeV (8 MeV) photon, the suppression factors are $S_{LPM} = 0.95$ (0.60) and $S_{Compton} = 0.99$ (0.92). Our simulated y spectrum from W boson decay electrons reproduces the spectrum obtained by a GEANT [40] simulation.

Photon Conversion

Photons can convert to an electron-positron pair by interacting with the tracker material. The differential cross section for a photon of energy $E_\gamma \gtrsim 1$ GeV to convert into an electron with energy E_e is given by the screened Bethe-Heitler equation [48]:

$$\frac{d\sigma}{dy} = \frac{A}{N_A X_0 \rho}\left[1 - (4/3 + C)y(1-y)\right],\qquad (12)$$

where $y = E_e/E_\gamma$. Integrating over y and multiplying by $\rho x N_A/A$ gives the total cross section, from which we obtain the following conversion probability at high photon energy:

$$P_{\gamma \to e^+e^-}(E_\gamma \to \infty) = 1 - e^{-(7/9 - C/6)x/X_0}.\qquad (13)$$

We parametrize the cross section as a function of photon energy using the tables for photon cross sections in silicon given in [54]. We apply the ratio shown in Fig. 10 to the high-energy cross section when calculating the conversion probability.

For each radiated photon upstream of the COT, we integrate the material between the radiation point and the COT inner can. If the photon converts, we take the conversion point to be halfway between the radiation point and the inner can. If the photon does not convert before the COT, we integrate the material in the COT and take a converting photon to convert halfway through the COT.
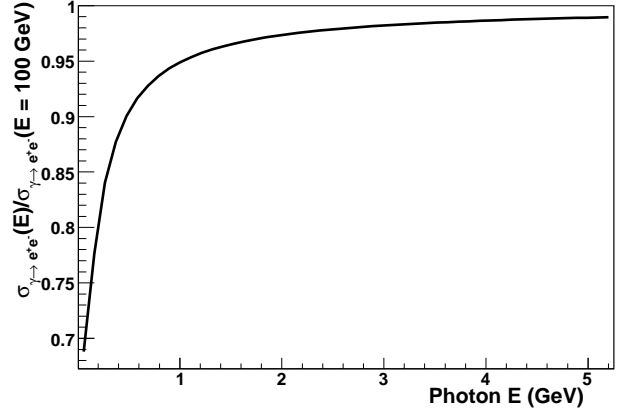
FIG. 10: The ratio of the photon conversion cross section at a given photon energy to the cross section at $E_\gamma = 100$ GeV [54]. We use this function to scale down the cross section obtained from the Bethe-Heitler equation [Eq. (13)] [48].

We use the conversion electron momentum spectrum from Eq. (12), ignoring the small effect of the C term on the shape. If a radiated photon has high momentum, a conversion electron's measured momentum can be larger than that of the electron from the W boson decay. To mimic the offline reconstruction, we assign the track from the highest momentum electron to the electron cluster.

Compton Scattering

The cross section for a low-momentum photon to scatter off an electron is similar to that of conversion into an e^+e^- pair. The differential cross section with respect to the photon fractional energy loss y can be approximated as (Appendix A):

$$\frac{d\sigma}{dy} \propto 1/y + y.\qquad (14)$$

Using a lower bound of $y = 0.001$, this spectrum approximates the Compton energy loss distribution for photons radiated from electrons from W boson decays.

We calculate the total cross section in terms of the pair production cross section using the tables for photon interactions in silicon in [54]. The ratio of cross sections as a function of energy is parametrized as (Fig. 11):

$$R_{Com} \equiv \frac{\sigma_{\gamma \to \gamma'}}{\sigma_{\gamma \to e^+e^-}(E_\gamma \to \infty)} = e^{F(E_\gamma)},\qquad (15)$$
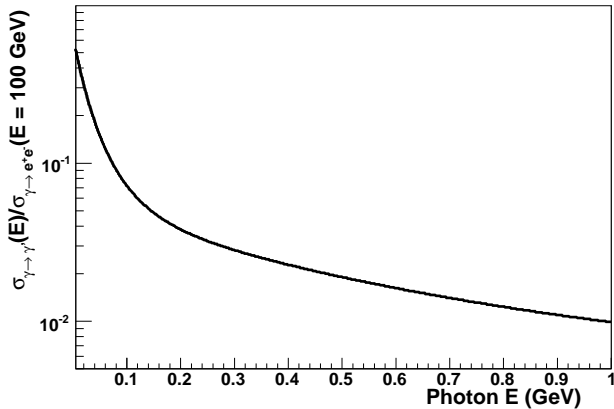
FIG. 11: The ratio of the Compton scattering cross section at a given photon energy to the pair-production cross section at $E_\gamma = 100$ GeV [54]. This ratio is applicable for photons traversing silicon.
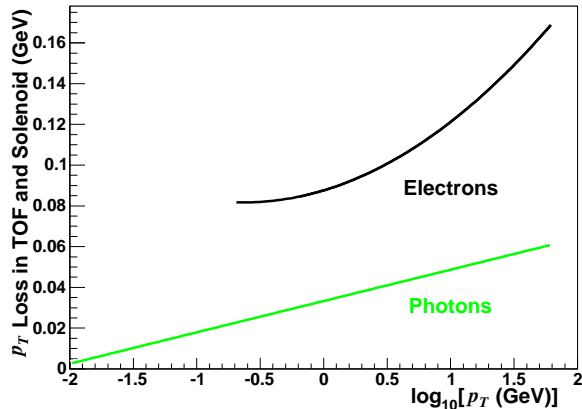

FIG. 12: The mean p_T loss as a function of $\log_{10}(p_T/\text{GeV})$ for electrons with $p_T > 400$ MeV and photons traversing the time-of-flight system and solenoid.

where $F(E_\gamma) = 2.35e^{-1.16E_\gamma} + 2.42e^{-15.8E_\gamma} - 5.21 - 0.151E_\gamma$, with E_γ in GeV, and γ and γ' are the initial- and final-state photons, respectively. We thus use the following Compton scattering probability per layer:

$$P_{\gamma\to\gamma'} = R_{Com}(7/9 - C/6)x/X_0. \qquad (16)$$

Energy Loss in Solenoid

After exiting the tracker electrons and photons travel through the time-of-flight (TOF) system and the solenoid. These systems have thicknesses of $\approx 10\%$ and $\approx 85\%$ of a radiation length, respectively. With this much material it becomes prohibitive to model individual radiative processes, and we instead use a parametrized energy-loss model determined from a GEANT simulation [40]. The energy loss is defined as the difference in energy of a single particle entering the TOF and the total energy of particles exiting the solenoid.

Figure 12 shows the mean energy loss as a function of $\log_{10}(p_T/\text{GeV})$ of the incoming particle for both photons and electrons. Electrons lose more energy than photons due to their ionization of the material. Since electrons with $p_T \lesssim 400$ MeV curve back to the center of the detector before exiting the solenoid, we do not parametrize energy loss in this energy region.

The energy loss distribution at a given particle p_T is reasonably described by an exponential. We use this distribution, with a mean determined by Fig. 12,

to model the energy loss of a given particle passing through the TOF and solenoid.

Calorimeter Response and Fiduciality

The calorimeter simulation models the response of the electromagnetic calorimeter as a function of each particle's energy and position, and the fraction of shower energy leaking into the hadronic calorimeter.

The electromagnetic calorimeter response, or the average measured energy divided by the true particle energy entering the calorimeter, can depend on each particle's energy. Possible sources of this dependence are variations in light yield as a function of calorimeter depth, attenuation in the light guide from the scintillator to the phototube, or leakage of showering particles into the hadronic calorimeter. The mean fractional energy leakage into the hadronic calorimeter for particles exiting the tracker, determined using the GEANT calorimeter simulation, is shown as a function of $\log_{10}(p_T/\text{GeV})$ in Fig. 13.

For a low-p_T particle exiting the tracker, the distribution of energy loss into the hadronic calorimeter is adequately described by an exponential. For high-p_T particles ($\gtrsim 10$ GeV), the distribution has a peak at non-zero values of energy loss. In this energy region we model the hadronic energy loss fluctuations with the distributions shown in Fig. 13. Because a non-negligible fraction of electrons lose a significant amount of energy ($5-10\%$) in the hadronic calorimeter, it is important to model the energy loss spectrum in addition to the mean hadronic energy loss.
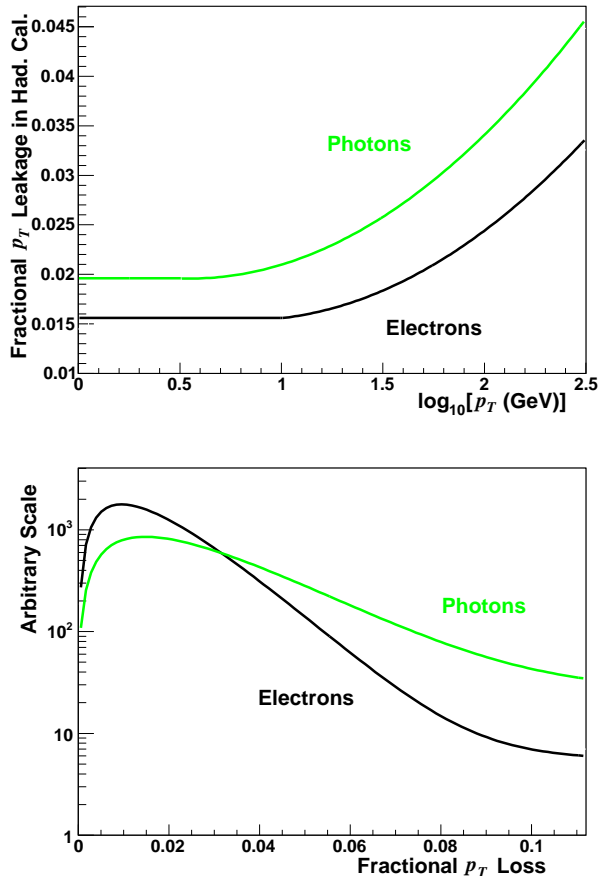
FIG. 13: The photon and electron p_T leakage into the hadronic calorimeter. Top: The mean p_T leakage as a function of $\log_{10}(p_T/\text{GeV})$. Bottom: The distributions of p_T leakage for high-p_T (> 10 GeV) photons and electrons.

To correct for any unaccounted dependence of the response on incoming particle energy, we use an empirical model of response that increases linearly with particle p_T:

$$R_{EM}(p_T) = S_E[1 + \xi(p_T/\text{GeV} - 39)]. \qquad (17)$$

We determine the slope parameter $\xi = [6 \pm 7(\text{stat})] \times 10^{-5}$ using fits to the electron E/p distribution as a function of p_T in $W \to e\nu$ and $Z \to ee$ events (Section VI). The inclusive E/p distribution from $W \to e\nu$ events is used to calibrate the absolute response S_E. Since electrons in this sample have a mean p_T of 39 GeV, the fitted values for S_E and ξ are uncorrelated. The parameter ξ describes the "non-linearity" of the calorimeter response.

Light attenuation in the scintillator results in non-uniform response as a function of distance from the

wavelength-shifting light guides. The attenuation function was measured using test beam data at construction, and aging effects are measured *insitu* using electrons from W boson decays. The function is parametrized as a quadratic function of the CES x position within a tower and corresponds to a reduction in response of $\approx 10\%$ at the edge of the tower. We simulate the light attenuation by reducing the energy deposited by each particle according to this function, evaluated at the particle's CES x position.

To improve measurement resolution in data, we correct for attenuation effects by applying the inverse of the quadratic attenuation function to the measured EM energy. We match this procedure in the simulation.

The EM calorimeter response drops rapidly as a particle crosses the edge of the scintillator and into the dead region between towers [30]. We take the calorimeter to have zero response for any particle with $|\text{CES } x| > 23.1$ cm or $|\text{CES } z| < 4.2$ cm. For the m_W measurement we only use high-energy electrons far from the dead regions (Section IV B).

We apply the following smearing to the calorimeter cluster energy:

$$\sigma_E/E = \sqrt{0.135^2/p_T + \kappa^2}, \qquad (18)$$

where the constant term κ is determined to be $[0.89 \pm 0.06(\text{stat}) \pm 0.13(\text{sys})]\%$ from a fit to the width of the electron E/p peak in W boson decays [55]. We find further energy smearing is necessary to model the multi-particle energy clusters populating the high E/p region. When a simulated W or Z decay electron radiates in the tracker, we apply an additional fractional resolution of $\kappa_\gamma = [8.3 \pm 2.2(\text{stat})]\%$ to each radiated particle. This smearing contributes $\approx 1.3\%$ to the effective constant term, and is determined from a fit to the width of the Z boson mass peak reconstructed from radiative electrons ($E/p > 1.06$).

The final contribution to the electron cluster energy comes from the underlying event [39] and additional $p\bar{p}$ interactions. As with muons, we measure this energy distribution in W boson data as a function of $u_{||}$, $u_\perp$, and the electron tower η (Section VII B). These measurements are incorporated in the simulation.

IV. W BOSON SELECTION

The W boson samples are collected with triggers requiring at least one central ($|\eta| \lesssim 1$) lepton candidate in the event. A narrow kinematic region is defined for W boson selection: 30 GeV < lepton p_T < 55 GeV; 30 GeV < $\not{p}_T$ < 55 GeV; 60 GeV

$< m_T(l,\not{p}_T) < 100$ GeV; and $u_T < 15$ GeV. This selection results in low background while retaining events with precise m_W information. Additional background rejection is achieved through event selection targeting the removal of Z boson decays to leptons. To minimize bias, lepton selection criteria are required to have high efficiency or to be explicitly modeled by our fast simulation.

A. $W \to \mu\nu$ Selection

Muons are identified based on their reconstructed COT track quality and production vertex, minimum ionizing energy deposited in the calorimeter, and the consistency of the track segments reconstructed in the muon chambers with the COT tracks.

All charged lepton candidates from W and Z boson decay are required to have fully-fiducial central ($|z_0| < 60$ cm) COT tracks with at least 5 hits on each of ≥ 3 axial superlayers and ≥ 3 small-angle stereo superlayers. For muon candidates we remove background from decays of long-lived hadrons to muons ("decays in flight") by requiring the track impact parameter to be small ($|d_0| < 1$ mm) and the track fit quality to be good ($\chi^2/\text{dof} < 3$). After this initial selection, the COT track parameters are updated with an additional constraint to the transverse position of the beam, which has a size of ≈ 30 μm in the luminous region. The beam constraint results in a factor of ≈ 3 improvement in momentum resolution for muons from W boson decays.

Each muon candidate's COT track is extrapolated to the calorimeter and its energy deposition in the electromagnetic and hadronic calorimeters is separately measured. Muons near a tower edge in the z direction cross two calorimeter towers, and those tower energies are combined to determine the muon's total energy deposition. We require the muon's electromagnetic energy deposition E_{EM} to be less than 2 GeV and its hadronic energy deposition E_{Had} to be less than 6 GeV [26].

All W muon candidates must have a track segment in either the CMU and CMP detectors, or the CMX detector. COT tracks extrapolated to these detectors must have $r - \phi$ positions that match to within 3, 5, or 6 cm of the CMU, CMP, or CMX track segment positions, respectively.

The $Z/\gamma^* \to \mu\mu$ process presents a significant background to the $W \to \mu\nu$ sample. We reduce this background by removing events with a second opposite-charge muon candidate passing the above selection, or passing the following looser set of criteria: an opposite-charge track with $p_T > 10$ GeV,

$|d_0| < 1$ mm, ≥ 2 axial superlayers with ≥ 5 hits, and ≥ 2 (1) small-angle stereo superlayers with ≥ 5 hits for tracks fully (partially) fiducial to the COT; $E_{EM} < 2$ GeV and $E_{Had} < 6$ GeV; and calorimeter isolation < 0.1. Calorimeter isolation is defined as the calorimeter p_T in an $\eta - \phi$ cone of radius 0.4 surrounding the muon calorimeter towers, divided by the muon track p_T. For events with one identified W decay muon and a second muon candidate passing the looser criteria, the identified W decay muon must also have isolation < 0.1 for the event to be rejected from the W boson sample. The full W boson sample, after kinematic selection and Z boson rejection, contains 51,128 events in (190.8 ± 11.1) pb^{-1} of data.

The identification efficiency of muons has a small dependence on the recoil in $W \to \mu\nu$ and $Z \to \mu\mu$ events, due primarily to the track χ^2 and d_0 requirements. We measure this dependence using $Z \to \mu\mu$ events, selected with one muon passing the W muon candidate criteria and a second "probe" muon identified as a track with $p_T > 30$ GeV. The two muons must have opposite charge and reconstruct to an invariant mass in the $81 - 101$ GeV range. The fraction of probe muons passing the additional W muon candidate selection criteria is shown in Fig. 14 as a function of net recoil energy along the muon direction ($u_{||}$). The observed dependence is parametrized as:

$$\epsilon = a[1 + b(u_{||} + |u_{||}|)], \qquad (19)$$

where a is a normalization factor that does not affect the m_W measurement and $b = [-1.32 \pm 0.40(\text{stat})] \times 10^{-3}$. We vary b by $\pm 3\sigma$ in simulated data and fit for m_W. Assuming a linear variation of m_W with b, we derive uncertainties of $\delta m_W = 1, 6$, and 13 MeV for the m_T, p_T, and $\not{p}_T$ fits, respectively.

B. $W \to e\nu$ Selection

Electron identification uses information from the COT track quality and production vertex, the matching of the track to calorimeter energy and position, and the longitudinal and lateral calorimeter energy profiles.

An electron candidate's COT track has the same fiduciality and hit usage requirements as a muon candidate track, and utilizes the same beam-constrained track fit. The track is required to have $p_T > 18$ GeV, a kinematic region where the trigger track-finding efficiency has no p_T dependence.

The clustering of showers in the CES produces an energy-weighted position at the electron shower maximum. We require the CES cluster to be well sepa-
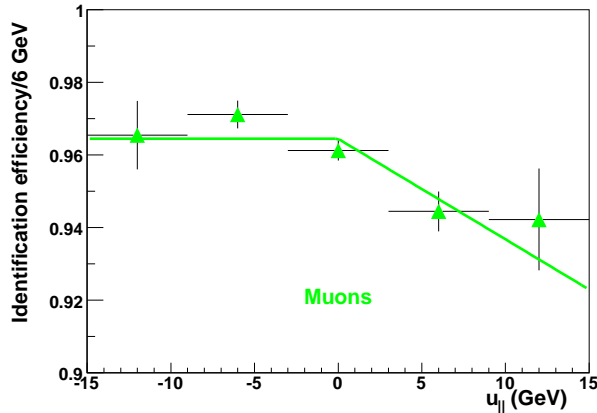
FIG. 14: The muon identification efficiency as a function of the recoil component in the direction of the muon ($u_{||}$).
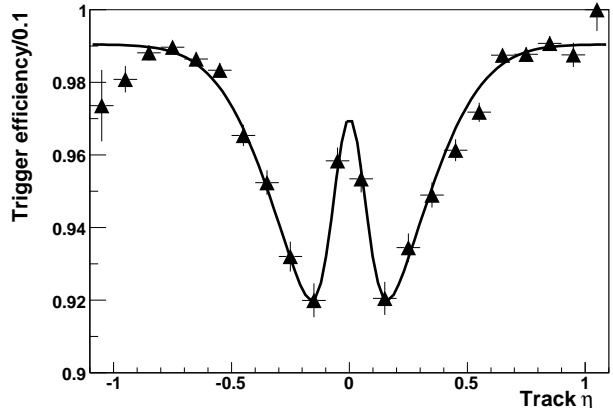

FIG. 15: The electron track trigger efficiency as a function of track η, for electrons identified in the calorimeter. The solid line shows the double-Gaussian parametrization of the data.

rated from the edges of the towers, $|\text{CES } x| < 18$ cm and $|\text{CES } z| > 9$ cm. The cluster z position is compared to the extrapolated track z position, and the difference is required to be less than 5 cm, consistent with the trigger requirement. The ratio of the measured calorimeter energy to the track momentum, E/p, must be less than 2.

Electrons are differentiated from hadrons by their high fraction of energy deposited in the electromagnetic calorimeter. The electron's EM energy is measured in two neighboring towers in η, while the energy collected in the hadronic calorimeter is measured in three towers. The ratio, E_{Had}/E_{EM}, is required to be less than 0.1. Only the EM calorimeter measurement is used to determine the electron's p_T.

An electron shower will typically be confined to a single tower, with a small amount of energy flowing into the nearest tower in η. We define an error-weighted difference between the observed and expected energies in the two towers neighboring the electron in the η direction [56]:

$$ L_{shr} = 0.14 \sum_i \frac{E_i^{adj} - E_i^{exp}}{\sqrt{0.14^2 E_i^{adj} + (\Delta E_i^{exp})^2}}, \quad (20) $$

where E_i^{adj} is the energy in a neighboring tower, E_i^{exp} is the expected energy contribution to that tower, ΔE_i^{exp} is the RMS of the expected energy, energies are measured in GeV, and the sum is over the two neighboring towers. We require $L_{shr} < 0.3$, consistent with the trigger criterion (Section III A 4).

The $Z \to ee$ background is highly suppressed by the $u_T < 15$ GeV requirement for the W boson sam-

ple. Residual background results from electrons passing through dead calorimeter regions, which reduces u_T and increases $\not{p}_T$. We remove events from the W sample if a track with $p_T > 20$ GeV and $|d_0| < 0.3$ cm extrapolates to a calorimeter region with reduced response ($|\text{CES } x| > 22$ cm or $|\text{CES } z| < 6$ cm), and the track's calorimeter isolation is < 0.1 (Section IV A). The full $W \to e\nu$ selection results in a sample of 63,964 candidate events in (218.1 ± 12.6) pb^{-1} of integrated luminosity.

The track selection in the single-electron trigger (Section III A 4) results in an η-dependent trigger efficiency for reconstructed electrons (Fig. 15). We study this efficiency using W events selected with a trigger where the track requirements are replaced by a $\not{p}_T$ threshold. The efficiency decreases as $|\eta|$ decreases because the reduced path length reduces the ionization charge collected by each wire, thus reducing the single hit efficiency. There is an additional decrease in efficiency due to the dead region at $|z| \lesssim 2$ mm. Electrons crossing this region at track $|\eta| = 0$ are not included in the efficiency plot, since we only measure electrons with $|\text{CES } z| > 9$ cm. Thus, at $|\eta| = 0$ there is no inefficiency due to the dead COT region, and the measured efficiency increases.

We measure the $u_{||}$ dependence of the electron identification efficiency (Fig. 16) using $Z \to ee$ events, selected with one electron passing the W electron candidate criteria and a second "probe" electron identified as an EM energy cluster with $p_T > 30$ GeV, an associated track with $p_T > 18$ GeV, and $E/p < 2$. Since the probe electron definition includes
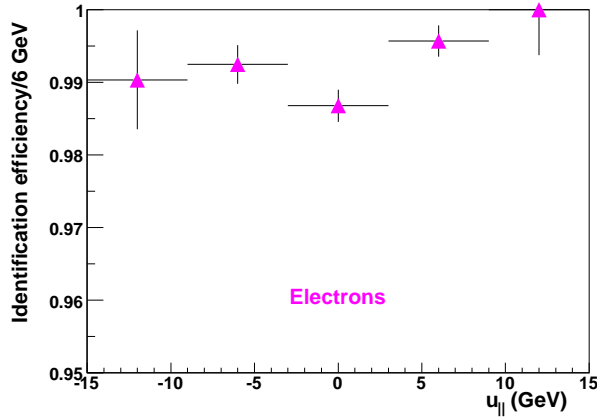
FIG. 16: The electron identification efficiency measured in $Z \rightarrow ee$ data as a function of the recoil component in the direction of the electron ($u_{||}$). Background is subtracted using the number of like-charge lepton events observed at a given $u_{||}$. The $E/p < 2$ requirement is not included in this efficiency measurement.

an E/p requirement, this cut is not included in the efficiency measurement. We instead study the unbiased $E/p < 2$ efficiency by recalculating E and $u_{||}$ for towers separated in ϕ from the identified electron in $W \rightarrow e\nu$ events, and find no significant $u_{||}$ dependence in this efficiency. In the simulation we use $b = 0 \pm 0.54 \times 10^{-3}$, obtained by fitting the measured efficiencies to the function in Eqn. 19.

We vary b by $\pm 3\sigma$ in pseudoexperiments and assume linear variation of m_W with b to derive uncertainties of $\delta m_W = 3, 5$, and 16 MeV for the m_T, p_T, and $\not{p}_T$ fits, respectively. Since b is measured with different data samples for the electron and muon channels, there is no correlation between the corresponding systematic uncertainties.

V.   TRACK MOMENTUM MEASUREMENT

Muon momenta are determined from helical fits to tracks reconstructed using COT information. The momentum resolution of prompt muons is improved by constraining the helix to originate from the transverse beam position. A given muon's transverse momentum is determined by the Lorentz equation,

$$
\begin{aligned}
mv^2/R &= evB, \\
p_T &= eB/(2|c|),
\end{aligned}
\tag{21}
$$

where B is the magnetic field, R is the radius of curvature, $c \equiv q/(2R)$ is the curvature of the he-

lix, and q is the muon charge. The *a priori* momentum scale is determined by the measurements of the magnetic field and the radius of the tracker. At CDF, $eB/2 = 2.11593 \times 10^{-3}$ GeV/cm, where B is measured using an NMR probe at a COT endplate. Measurements of the local field nonuniformities and tracker geometry were performed during construction and installation and are used to determine the positions of individual track hits. We find these measurements provide an *a priori* momentum scale accuracy of $\approx 0.15\%$.

We refine the momentum scale calibration with data. Using reconstructed cosmic ray muon tracks, we align the relative positions of the tracker wires. Track-level corrections derived from $W \rightarrow e\nu$ data reduce relative curvature bias between positive and negative particles. Finally, we perform an absolute calibration of the momentum scale using high-statistics data samples of J/ψ, Υ, and Z boson decays to muons. The final calibration is applied as a relative momentum correction $\Delta p/p$ to the W boson data and has an accuracy of $\approx 0.02\%$.

A.   COT Alignment

The COT contains 30,240 sense wires for measuring the positions of charged particles passing through the detector. The position measurements rely on an accurate knowledge of the wire positions throughout the chamber. We determine these positions using a combination of alignment survey, computer modeling, and cosmic-ray muon data. Any remaining biases in track parameter measurements are studied with $J/\psi \rightarrow \mu\mu$ and $W \rightarrow e\nu$ data, from which final track-level corrections are derived.

After construction of the COT endplates, the position of each 12-wire cell was measured with an accuracy of ± 13 μm using a coordinate measuring machine. The effect of the load of the wire plane and field sheets was modeled with a finite element analysis (FEA) and found to cause an endplate bend towards $z = 0$ cm, with the maximum bend of ≈ 6 mm in the fifth superlayer [29]. An equivalent load was applied to the detector and further measurements found the FEA to be accurate to within $\approx 20\%$. The FEA results were scaled to match the measurements, and the positions determined from the FEA were set as the directly-determined cell positions.

While each cell position determines the average positions of its 12 sense wires within the chamber, several effects create a non-linear wire shape as a function of z. Gravity has the most significant effect, causing each wire to sag ≈ 260 μm in y at $z = 0$
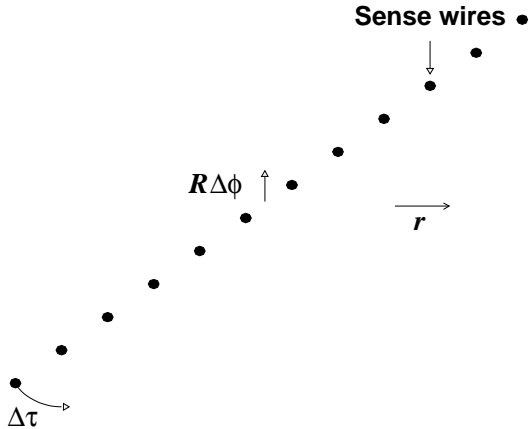
FIG. 17: The definitions of the local tilt ($\Delta\tau$) and azimuthal shift ($R\Delta\phi$) alignment corrections applied to each COT cell.

cm. Electrostatic deflection towards the nearest field sheet occurs for cells where the sense wire is not centered between the field sheets. By construction, the wires are slightly offset within a cell; in addition, the gravitational sag of the field sheets is larger than that of the sense wires, resulting in an electrostatic deflection that partially counteracts the sag of the sense wires. Combined, the electrostatic effects cause a ϕ-dependent wire shift that has a maximum of 74 μm at $\phi = 145^o$ and $z = 0$ cm. The gravitational and electrostatic effects were combined to determine the best *a priori* estimate of the wire shapes.

Starting from the predicted cell and wire positions, we develop *in situ* corrections based on cosmic-ray muon data taken during $p\bar{p}$ crossings with the single muon trigger. The data are selected by requiring exactly two reconstructed tracks in the event, eliminating effects from overlapping hits from collision-induced particles. Since the two tracks on opposite sides of the COT result from a single cosmic-ray muon, we refit both tracks to a single helix and determine hit residuals with respect to this helix [57]. For each cell, we use the residuals to determine a tilt correction about its center, and a shift correction along the global azimuth (Fig. 17). We show the tilt and shift corrections for the inner superlayer of the west endplate in Fig. 18, after removing global corrections. We apply these corrections to each cell of each superlayer in each endplate. In addition, we measure a relative east-west shift and include it in each cell's correction.

We combine the cell-based corrections with wire-
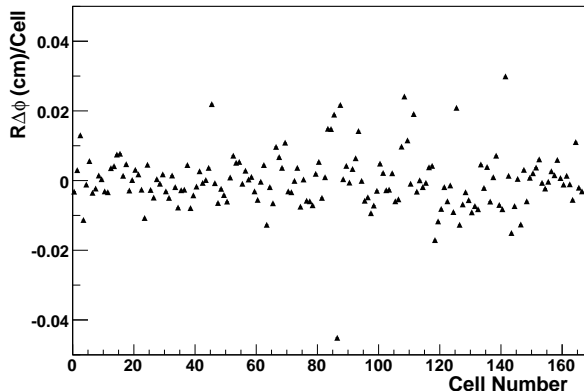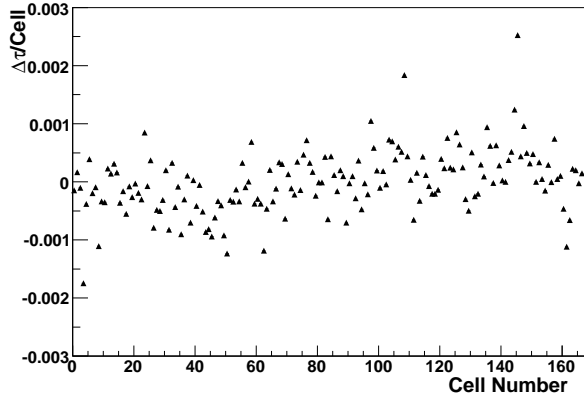
FIG. 18: The local tilt (top) and azimuthal shift (bottom) alignment corrections applied to each cell of the inner superlayer of the west endplate. Not shown are a global 0.0021 tilt correction and a small global rotation and shift of the COT that does not affect track measurements.

based corrections for the shapes of the wires between the endplates. We measure these corrections as functions of z and radius R using the differences in the measured d_0 and curvature parameters for the helix fits on opposite sides of the COT for a cosmic ray muon. The corrections are applied as additional offsets $\Delta\xi$ of the wires at $z = 0$ cm, with a parabolic wire shape as a function of z. The corrections include a radial dependence,

$$\Delta\xi = -160 + 380(R/140) - 380(R/140)^2, \quad (22)$$

where R is measured in cm and $\Delta\xi$ in μm. Figure 19 shows the gravitational and electrostatic shifts of a wire as a function of z at $\phi = \pi$, as well as the data-based correction at $R = 130$ cm (the outer superlayer).

The cell- and wire-based corrections are implemented for the track-finding and fitting stage, and re-
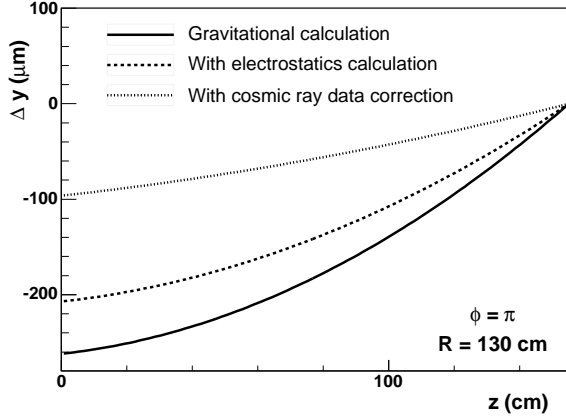
FIG. 19: The net wire shift in y as a function of z from gravitational sag only (solid), including electrostatic effects (dashed), and including data-based corrections from Eq. (22) (dotted). The shift is shown at $\phi = \pi$ and $R = 130$ cm.

duce the measured hit resolution for high-momentum muons from ≈ 180 μm to ≈ 140 μm. Final track-based corrections are applied to the measured track curvature, which is inversely related to the transverse momentum [Eq. (21)]. Expanding the measured curvature c as a function of the true curvature c_t in a Taylor series around zero,

$$c = \epsilon_1 + (1 + \epsilon_2)c_t + \epsilon_3 c_t^2 + \epsilon_4 c_t^3 + ..., \qquad (23)$$

the terms even in c_t cause biases in positive tracks relative to negative tracks, which tend to cancel when the two are averaged. The term linear in c_t scales the true curvature and is determined by the momentum calibration. The $\epsilon_4 c_t^3$ term is the first to directly affect mass measurements and is suppressed by the c_t^3 factor at low curvature (high momentum).

Corrections for high-momentum tracks from W and Z decay particles are determined using the difference in E/p for e^+ and e^- from W decays, which should be zero in the absence of misalignments. This difference can be used to constrain ϵ_1, the first term in the Taylor expansion. Figure 20 shows the differences in E/p as functions of $\cot\theta$ and ϕ, before and after corrections of the following form:

$$\begin{aligned} \delta c = \; & a_0 + a_1 \cot\theta + a_2 \cot^2\theta + \\ & b_1 \sin(\phi + 0.1) + b_3 \sin(3\phi + 0.5). \end{aligned} \qquad (24)$$

The terms can be interpreted as arising from the following physical effects: a relative rotation of the outer edge to the inner edge of each endplate (a_0);
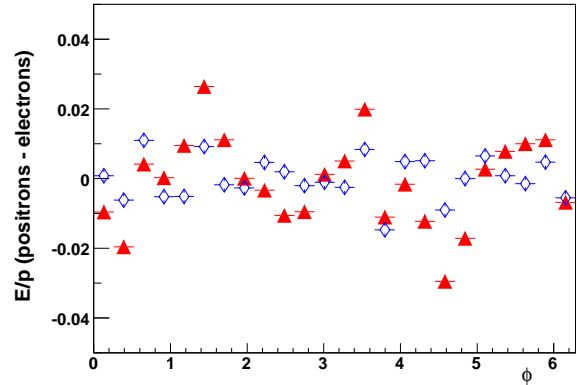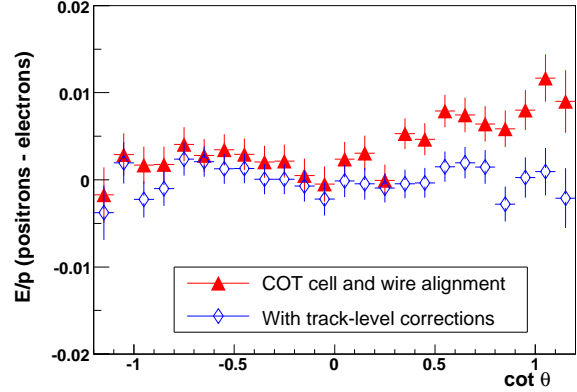

FIG. 20: The difference between e^+ and e^- E/p as a function of $\cot\theta$ (top) and ϕ (bottom) before (triangles) and after (diamonds) track-level corrections.

a relative rotation of the east and west endplates ($a_1 \cot\theta$); and a mismeasurement of the beam position ($b_1 \sin(\phi + 0.1)$). The measured values of the parameters a_0, a_1, a_2, b_1, and b_3, are shown in Table III.

Varying a_1 by $\pm 3\sigma$ in pseudoexperiments and assuming linear variation of the momentum scale with a_1, we find the a_1 uncertainty results in a relative momentum scale uncertainty of $\pm 0.07 \times 10^{-3}$ for W and Z boson mass measurements. The other parameter uncertainties, as well as residual higher-order terms, have a negligible impact on the momentum scale for the m_W measurement.

B. $J/\psi \to \mu\mu$ Calibration

With a measured $\sigma \times BR$ of $16.3^{+1.4}_{-1.3}$ nb [28], J/ψ mesons are the Tevatron's most prolific source of resonant decays to muon pairs. In addition to

23

Parameter	Value ($\times 10^{-7}$ cm^{-1})
a_0	-0.66 ± 0.17
a_1	-1.6 ± 0.3
a_2	-2.1 ± 0.5
b_1	-2.1 ± 0.2
b_3	5.7 ± 1.7

TABLE III: The parameters used to correct the track curvature of electrons and muons from W and Z boson decays. The values and statistical uncertainties are determined from fits to the E/p difference between positrons and electrons.

its high statistics, the J/ψ's precisely known mass ($m_{J/\psi} = 3096.88 \pm 0.04$ MeV [58]) and narrow width ($\Gamma_{J/\psi} = 0.0934 \pm 0.0021$ MeV [11]) make it a key component of the track momentum calibration. We perform measurements of the J/ψ mass as a function of mean inverse muon p_T to determine a momentum scale correction and extrapolate to the high-p_T region relevant for W and Z boson decays.

1. Data Sample

The J/ψ data sample is collected with a Level 1 trigger requiring one $p_T > 1.5$ GeV XFT track with a matching CMU track segment, and a second $p_T > 1.5$ (2) GeV XFT track with a matching CMU (CMX) segment. At Level 3, the two corresponding COT tracks must have opposite charge and consistent z vertex positions ($|\Delta z_0| < 5$ cm), and must form an invariant mass between 2.7 and 4 GeV. The resolution on the invariant mass measurement degrades at high track momentum, so to avoid trigger bias the mass range is extended to 2 GeV $< m_{\mu\mu} < 5$ GeV when the p_T of the muon pair $p_T^{\mu\mu}$ is greater than 9 GeV.

Candidate events are selected offline by requiring two COT tracks, each with $p_T > 2$ GeV, $|d_0| < 0.3$ cm, and ≥ 7 hits on each of the eight superlayers. The tracks must originate from a common vertex ($|\Delta z_0| < 3$ cm) and form an invariant mass in the range $(2.95, 3.21)$ GeV.

A significant fraction ($\approx 20\%$) of the J/ψ mesons in our data sample result from decays of B hadrons, which have an average proper decay length of ≈ 0.5 mm. The muons from the J/ψ decay can thus originate outside the beam radius. Therefore, no beam constraint is applied in the COT track fit of muon candidates from J/ψ decays.

The total sample consists of 606,701 J/ψ candidates in (194.1 ± 11.3) pb^{-1} of integrated luminosity.

2. Monte Carlo Generation

We use PYTHIA [59] to generate $J/\psi \to \mu\mu$ events, from which templates are constructed to fit the data for the momentum scale. The shape of the $m_{\mu\mu}$ distribution from J/ψ decays is dominated by the p_T-dependent detector resolution. We therefore model the $p_T^{J/\psi}$ distribution as well as the p_T and relative p_T of the muons in a J/ψ decay. To obtain an adequate model, we empirically tune the generated J/ψ kinematics to describe the relevant data distributions for the J/ψ mass fits.

To tune the $p_T^{J/\psi}$ distribution, we boost the J/ψ momentum by changing its rapidity ($y_{J/\psi}$) along its direction of motion $\hat{p}_{J/\psi}$. In 50% of the generated events we multiply $y_{J/\psi}$ by 1.215, and in the other 50% we multiply it by 1.535. The decay angle θ^* in the J/ψ rest frame relative to $\hat{p}_{J/\psi}$ is tuned by multiplying $\cot \theta^*$ by 1.3. After tuning, the simulation matches the relevant background-corrected data distributions, as shown in Fig. 21.

The PYTHIA event generator does not include energy loss due to final-state photon radiation from the muons in J/ψ decays. To simulate this effect, we scale each muon's momentum by a factor x determined from the following leading-log probability distribution for soft photon radiation [59, 60]:

$$f(x) = \beta(1-x)^{\beta-1}, \qquad (25)$$

with

$$\beta = \frac{\alpha_{EM}}{\pi}[\ln(Q^2/m_\mu^2) - 1] \qquad (26)$$

and $Q^2 = m_{J/\psi}^2$.

3. Momentum Scale Measurement

The momentum scale is calibrated using J/ψ decays by fitting the dimuon mass as a function of mean inverse p_T of the two muons, and then extrapolating to high p_T ($\langle p_T^{-1} \rangle \approx 0$ GeV^{-1}). This procedure results in a track momentum calibration accuracy of 0.025%.

The momentum scale calibration requires an accurate modeling of the muon ionization energy loss in the tracker. Each muon passing through the silicon and COT detectors loses on average 9 MeV at normal incidence. The combined effect on the reconstructed $m_{\mu\mu}$ is about 0.6% of $m_{J/\psi}$, a factor of ≈ 20 larger than our total uncertainty. Since the ionization energy loss E_I varies only logarithmically with p_T (Section III B 1), the relative effect on the reconstructed
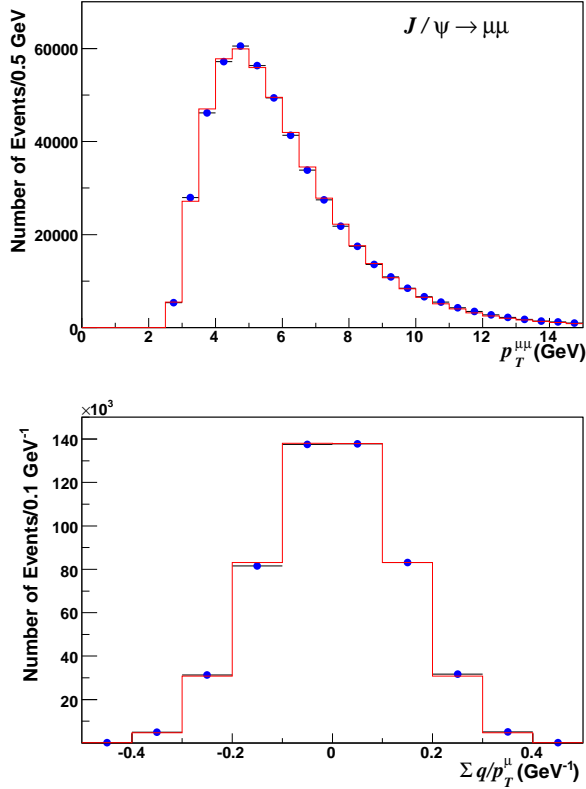
FIG. 21: The $J/\psi \to \mu\mu$ data (points) and tuned simulation (histogram) distributions of $p_T^{\mu\mu}$ (top) and $\sum q/p_T^\mu$ (bottom). The $\sum q/p_T^\mu$ is equal to the sum of the track curvatures of muons from a J/ψ decay, divided by 2.11593×10^{-3}.

mass is:

$$\frac{\Delta m}{m} = \frac{E_I^{\mu^+}}{2p_T^{\mu^+}} + \frac{E_I^{\mu^-}}{2p_T^{\mu^-}} \approx E_I \left\langle p_T^{-1} \right\rangle. \qquad (27)$$

Thus, in a linear fit of $\Delta m/m$ as a function of mean inverse p_T, a non-zero slope approximately corresponds to E_I. Since we model the ionization energy loss based on the known detector material, this slope should be zero. We however find that we need to scale down the ionization energy loss from the detector parametrization (Section III B 1) by 6% to achieve a zero slope. We show the result of this tuning in Fig. 22, replacing $\Delta m/m$ on the $y-$axis with the relative momentum correction $\Delta p/p$ to be applied to the data in order to measure $m_{J/\psi} = 3096.88$ MeV. The tuning is based on a $\left\langle p_T^{-1} \right\rangle$ region of $(0.1, 0.5)$ GeV^{-1}, divided into eight bins. We find a scale correction of $\Delta p/p = [-1.64 \pm 0.06(\text{stat})] \times 10^{-3}$ from a linear fit
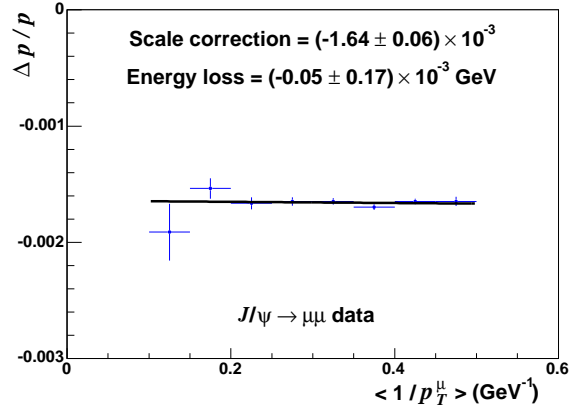
FIG. 22: The fractional momentum correction for data as a function of the mean inverse momentum of the muons from J/ψ decays. In a linear fit, the intercept corresponds to the scale correction relevant for W and Z boson decays, and the slope corresponds to the remaining unmodeled ionization energy loss after material tuning. The uncertainties are statistical only.

to $\Delta p/p$ as a function of $\left\langle p_T^{-1} \right\rangle$.

Each $\Delta p/p$ value in Fig. 22 is extracted via a binned likelihood fit to the $m_{\mu\mu}$ distribution for each $\left\langle p_T^{-1} \right\rangle$ bin. Since the mass resolution varies significantly with $\left\langle p_T^{-1} \right\rangle$, the fit ranges are adjusted from 3.08 ± 0.13 GeV for $\left\langle p_T^{-1} \right\rangle = (0.1, 0.15)$ GeV^{-1} to 3.08 ± 0.08 GeV for $\left\langle p_T^{-1} \right\rangle = (0.45, 0.5)$ GeV^{-1}. The background is modeled as a linear function of $m_{\mu\mu}$, with normalization and slope determined from upper and lower sideband regions whose combined width is equal to that of the mass fit window. The results of the fits in the $\left\langle p_T^{-1} \right\rangle = (0.15, 0.2)$ GeV^{-1} and $\left\langle p_T^{-1} \right\rangle = (0.25, 0.3)$ GeV^{-1} ranges are shown in Fig. 23.

The J/ψ momentum calibration includes corrections to the curvature c derived from the measured dimuon mass as a function of $\Delta \cot\theta$ between the positive and negative muons from the J/ψ decay. Biases linear in $\Delta \cot\theta$ are removed with a curvature correction linear in $\cot\theta$:

$$\delta c = [(-7 \pm 1) \times 10^{-7} \text{ cm}^{-1}] \cot\theta, \qquad (28)$$

where the uncertainty is statistical only. Biases quadratic in $\Delta \cot\theta$ are removed with the following correction to the absolute length scale of the COT along the z axis (statistical uncertainty only):

$$\delta \cot\theta = [(-3.75 \pm 1.00) \times 10^{-4}] \cot\theta. \qquad (29)$$

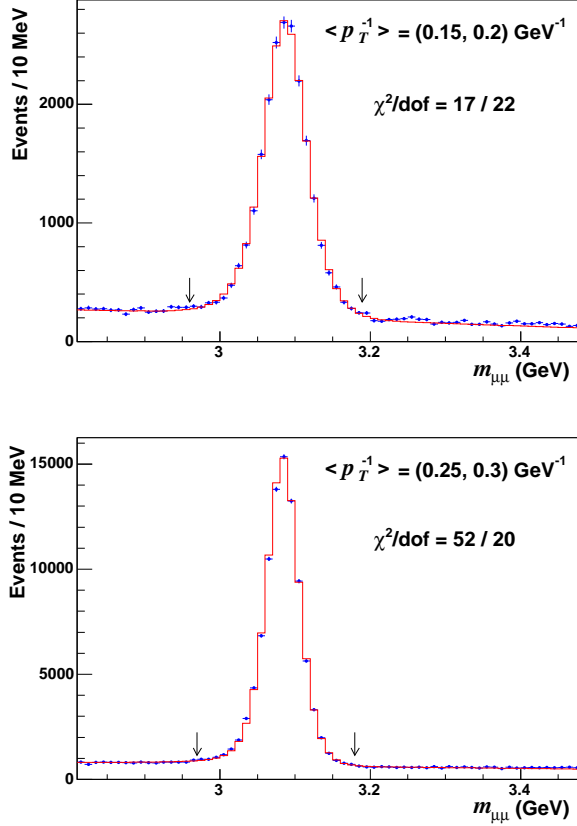FIG. 23: The $m_{\mu\mu}$ fits to data (points) with $\langle p_T^{-1} \rangle =$ $(0.15, 0.2)$ GeV^{-1} (top) and $\langle p_T^{-1} \rangle = (0.25, 0.3)$ GeV^{-1} (bottom). The best fit to the $m_{\mu\mu} = (3.08 \pm 0.12)$ GeV (top) and $m_{\mu\mu} = (3.08 \pm 0.11)$ GeV (bottom) regions correspond to momentum scale corrections of $(-1.54 \pm 0.09) \times 10^{-3}$ (top) and $(-1.65 \pm 0.04) \times 10^{-3}$ (bottom). The arrows indicate the fit regions and the uncertainties are statistical only. The fit χ^2 can be improved by adjusting the final-state radiation model, and this effect is incorporated into the systematic uncertainty (Section V B 4).

The $\cot\theta$-dependent correction to the curvature [Eq. (28)] is larger than the correction derived from E/p in $W \to e\nu$ data (a_1 in Table III). Muons from J/ψ decay have a broader curvature range and thus a greater dependence on misalignments affecting higher order terms in curvature. Since we derive a curvature correction averaged over all of the terms in Eq. (23), the J/ψ correction can be larger than the correction for electrons and muons from W and Z boson decays.

4. Momentum Scale Uncertainties

Systematic uncertainties on the momentum scale correction extracted from $J/\psi \to \mu\mu$ decays (Table IV) are dominated by the incompleteness of the QED and energy loss models. At low muon p_T (high $\langle p_T^{-1} \rangle$), the mass fits become increasingly sensitive to QED and energy loss modeling because of the better mass resolution and higher statistics. Since we only model the mean ionization energy loss, our modeling of the mass region below the peak is imperfect. Additionally, our neglect of higher-order QED corrections affects the modeling of this region. We study possible bias from our incomplete model by changing the Q^2 value in the photon radiation probability function [Eq. (25)] such that the χ^2 of the inclusive $m_{\mu\mu}$ fit is minimized. We find that this change affects $\Delta p/p$ by 0.2×10^{-3}.

If there is a relative tilt between the solenoid and the tracker axes, the extracted momentum scale correction will have a linear dependence on $\Delta \cot\theta$. In addition, incomplete corrections of the magnetic field nonuniformities near the ends of the solenoid can cause a quadratic $\cot\theta$ variation. We study the $\cot\theta$ dependence of $\Delta p/p$ using J/ψ decays where both muons are measured in the same $\cot\theta$ region ($|\Delta \cot\theta(\mu\mu)| < 0.1$). We find that if we correct for the observed quadratic dependence, the extracted $\Delta p/p$ changes by 0.1×10^{-3}.

The uncertainty on the material correction propagates to a momentum scale uncertainty of 0.06×10^{-3} when extrapolated to high momentum, as shown in Fig. 22. An additional statistical uncertainty of 0.01×10^{-3} on the scale is determined by fixing the material correction and fitting for the scale.

The statistical uncertainties on the J/ψ alignment corrections [Eq. (28) and (29)] have a 0.05×10^{-3} effect on $\Delta p/p$. We test our model of the $m_{\mu\mu}$ lineshape by changing the fit range by $\pm 20\%$, and find a $\pm 0.05 \times 10^{-3}$ change in $\Delta p/p$.

We apply the same p_T thresholds offline as in the trigger for muons with CMU segments. Since we do not model a p_T-dependent trigger efficiency, any inefficiency could cause a bias in the reconstructed $m_{\mu\mu}$. We investigate this possibility by varying the offline p_T thresholds by $\pm 5\%$, and find a $\Delta p/p$ variation of $\pm 0.04 \times 10^{-3}$.

The quality of the fit is highly sensitive to the hit resolution model, but the momentum scale correction is not. Changing the simulated COT hit resolution by ± 10 μm, which corresponds to a $> 10\sigma$ statistical variation, results in a $\pm 0.03 \times 10^{-3}$ change in $\Delta p/p$. We include this in our systematic uncertainty estimate.

A $\pm 0.03 \times 10^{-3}$ uncertainty on $\Delta p/p$ from the background model is determined by changing its linear dependence on $m_{\mu\mu}$ to a constant. Finally, the world-average J/ψ mass value used in this measurement contributes $\pm 0.01 \times 10^{-3}$ to the uncertainty on $\Delta p/p$.

The final momentum scale correction derived from J/ψ data is:

$$\Delta p/p = (-1.64 \pm 0.25) \times 10^{-3}. \qquad (30)$$

C. $\Upsilon \rightarrow \mu\mu$ Calibration

The $b\bar{b}$ resonance Υ provides a complementary momentum scale calibration tool to the J/ψ. Its precisely measured mass $m_\Upsilon = (9460.30 \pm 0.26)$ MeV [11] is three times larger than that of the J/ψ, so an Υ momentum scale calibration is less sensitive to the material and energy loss model than that of the J/ψ. Because the $b\bar{b}$ resonances are the highest mass mesons, long-lived hadrons do not decay to the Υ and the muons from Υ decay effectively originate from the collision point. We improve the accuracy of the muon measurements by constraining their tracks to the beam position, which is the same procedure applied to the W and Z decay lepton tracks.

The Υ data sample is based on the same Level 1 trigger as the J/ψ sample (Section V B 1). The Level 3 requirements are: one reconstructed track with $p_T > 4$ GeV and matching CMU and CMP track segments (CMUP); a second track with opposite charge to the first, $p_T > 3$ GeV, and a matching CMU or CMX track segment; and a reconstructed mass of the two tracks between 8 and 12 GeV. Offline, the p_T thresholds are increased to 4.2 (3.2) GeV for the track with a CMUP (CMU or CMX) track segment, and each track must have $|d_0| < 0.3$ cm and at least 5 hits in at least 3 axial and 3 stereo superlayers. The two tracks are required to have a common vertex ($|\Delta z_0| < 3$ cm).

We model Υ production and decay using PYTHIA [59], to which we apply the same tuning procedure as for J/ψ generation. The data p_T^Υ distribution is matched in simulation by boosting the rapidity of each decay muon by $0.07 y_\Upsilon$ along $\hat{p}_\Upsilon$, where y_Υ is the Υ rapidity. Radiation of photons from the final state muons is simulated using the probability distribution of Eqns. 25 and 26. The $p_T^{\mu\mu}$ distribution is shown in Fig. 24, after subtracting background from the data.

We test any possible beam-constraint bias by separately reconstructing charged muon tracks from Υ decays with and without incorporating the beam constraint. For the sample with beam-constrained tracks we fit for m_Υ in the region 9.28 GeV $<$
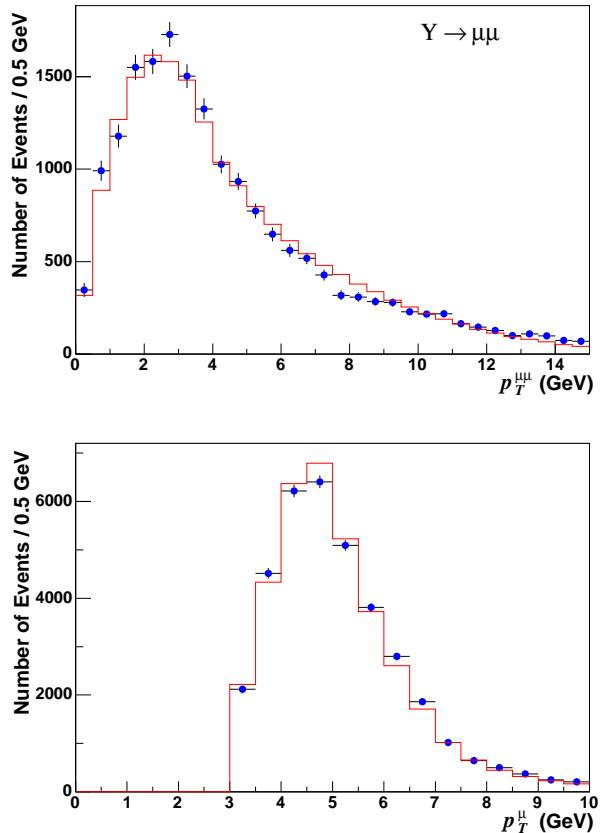

FIG. 24: The $p_T^{\mu\mu}$ (top) and p_T^μ (bottom) distributions from $\Upsilon \rightarrow \mu\mu$ decays for the data (points) and simulation (histogram).

$m_{\mu\mu} < 9.58$ GeV, while for the sample with non-beam-constrained tracks we fit the region 9.25 GeV $< m_{\mu\mu} < 9.61$ GeV. In (190.8 ± 11.1) pb^{-1} of integrated luminosity, we have 34,618 Υ candidates with beam-constrained tracks and 35,622 candidates with non-beam-constrained tracks. The two momentum scale measurements are shown in Fig. 25 and are consistent at the 2σ level when correlations are taken into account. We define the Υ result to be the mean of the two values, and take half their difference ($\Delta p/p = 0.06 \times 10^{-3}$) as a systematic uncertainty on the measurement.

The remaining systematic uncertainties on the momentum scale measurement with Υ decays are common to those of the measurement with J/ψ decays. We use the same procedures as with the J/ψ calibration to estimate the sizes of the uncertainties, with one exception. Since the Υ sample has $< 10\%$ of the statistics of the J/ψ sample, the QED and energy loss

Source	J/ψ ($\times 10^{-3}$)	Υ ($\times 10^{-3}$)	Common ($\times 10^{-3}$)
QED and energy loss model	0.20	0.13	0.13
Magnetic field nonuniformities	0.10	0.12	0.10
Beam constraint bias	N/A	0.06	0
Ionizing material scale	0.06	0.03	0.03
COT alignment corrections	0.05	0.03	0.03
Fit range	0.05	0.02	0.02
Trigger efficiency	0.04	0.02	0.02
Resolution model	0.03	0.03	0.03
Background model	0.03	0.02	0.02
World-average mass value	0.01	0.03	0
Statistical	0.01	0.06	0
Total	0.25	0.21	0.17

TABLE IV: Uncertainties on the momentum scale correction derived from the J/ψ and Υ mass measurements.

model cannot be tested with the χ^2 of the $\Upsilon \to \mu\mu$ mass fit. Instead, we change Q in the photon radiation probability by the amount estimated for the J/ψ systematic uncertainty (Section V B 4). We find that this variation affects $\Delta p/p$ by $\pm 0.13 \times 10^{-3}$ in the Υ calibration.

The final result of the Υ calibration is:

$$\Delta p/p = (-1.44 \pm 0.21) \times 10^{-3}. \qquad (31)$$

We have verified that this result has no time dependence, at the level of the statistical precision of $\pm 0.13 \times 10^{-3}$. When combined with the momentum scale correction from the J/ψ calibration, we obtain:

$$\Delta p/p = (-1.50 \pm 0.19) \times 10^{-3}. \qquad (32)$$

D. $Z \to \mu\mu$ Calibration

Given the precise momentum scale calibration from the J/ψ and Υ decays, we measure the Z boson mass and compare it to the world-average value $m_Z = (91187.6 \pm 2.1)$ MeV [11]. We then use the world-average m_Z to derive an additional $\Delta p/p$ calibration and combine it with that of the J/ψ and Υ decays.

The systematic uncertainties of the m_Z measurement are correlated with those of the m_W measurement, so a momentum scale calibration with Z bosons can reduce systematic uncertainties on the m_W measurement. However, the statistical uncertainty from the $Z \to \mu\mu$ sample is significantly larger than the calibration uncertainty from J/ψ and Υ decays. Thus, the main purpose of the m_Z measurement is to confirm the momentum scale calibration and test our systematic uncertainty estimates.

The Z boson data sample is selected using the same single-muon trigger and offline muon selection as for the W boson sample (Sections III A 4 and IV A), with the exception that we remove the requirement of a track segment in a muon detector for one of the muons from the Z boson decay. Removing this requirement significantly increases detector acceptance while negligibly affecting background. Z boson candidates are defined by 66 GeV $< m_{\mu\mu} <$ 116 GeV, $p_T^{\mu\mu} <$ 30 GeV, $|\Delta t_0(\mu,\mu)| <$ 3 ns, and oppositely charged muons. A muon track's t_0 is defined as the time between the $p\bar{p}$ bunch crossing and the muon's production, and should be (0 ± 1) ns for $Z \to \mu\mu$ production and decay. The track t_0 is measured using the time information from the track hits in the COT by incorporating t_0 into the helical fit. The $|\Delta t_0| <$ 3 ns requirement effectively removes cosmic ray muons passing through the detector. An additional cosmic ray identification algorithm [57] reduces this background to a negligible size. After applying all selection criteria, the $Z \to \mu\mu$ sample contains 4,960 events in (190.8 ± 11.1) pb^{-1} of integrated luminosity.

We model Z boson production and decay using the RESBOS [61] event generator and a next-to-leading order QED calculation of photon radiation from the final-state muons [62] (Section IX). For $m_{\mu\mu}$ near the Z boson resonance, the photon propagator and Z/γ^* interference make small contributions to the shape of the $m_{\mu\mu}$ distribution. We separately simulate these components and include them as fixed "background" to the Z lineshape. We measure m_Z using a binned likelihood template fit to the data in the range 83 GeV $< m_{\mu\mu} <$ 99 GeV (Fig. 26). Our measurement of $m_Z = [91.184 \pm 0.043(\text{stat})]$ GeV is

FIG. 26: The m_Z fit to data (points) in the 83 GeV $< m_{\mu\mu} < 99$ GeV region (denoted by arrows). The uncertainty is statistical only.
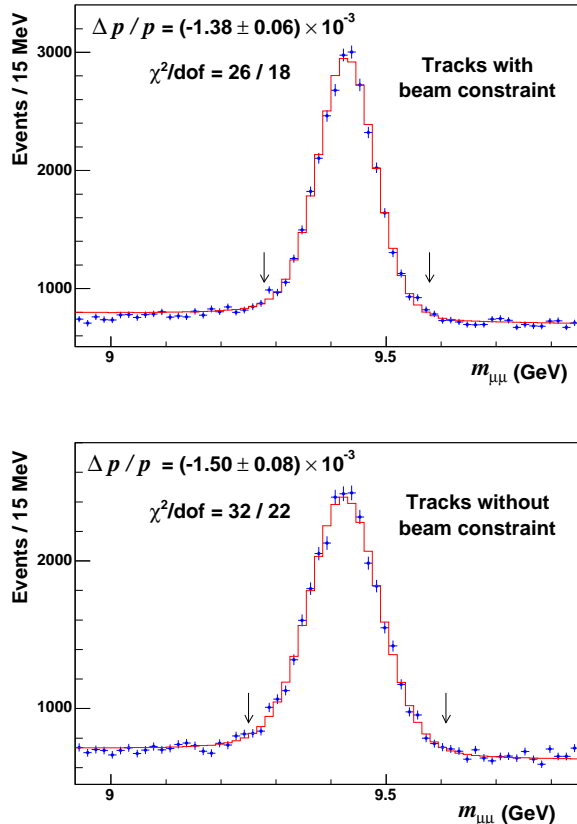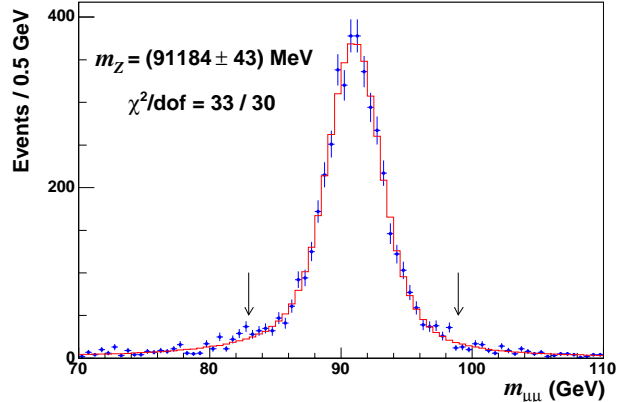

FIG. 25: The momentum scale correction $\Delta p/p$ derived from binned likelihood fits to the $m_{\mu\mu}$ data distribution (points) in the region dominated by $\Upsilon \to \mu\mu$ decays. The small difference between fits using tracks with (top) and without (bottom) a beam constraint is incorporated into the systematic uncertainty. The arrows indicate the fit region and the uncertainties are statistical only.

in good agreement with the world-average value of $m_Z = (91.188 \pm 0.002)$ GeV [11].

Systematic uncertainties on m_Z are due to the momentum scale calibration (17 MeV), alignment correction uncertainties (7 MeV), and incomplete modeling of higher-order QED corrections (14 MeV). The combined statistical and systematic uncertainty is 49 MeV.

Given the precise world-average measurement of m_Z, we use the Z boson resonance as an additional calibration input to $\Delta p/p$. We find that adding the m_Z information reduces $\Delta p/p$ and its uncertainty by less than 0.01×10^{-3} each.

Incorporating the alignment uncertainty (Section V A) into $\Delta p/p$ from Eqn. 32 gives the mo-

mentum scale correction applicable to the W boson sample:

$$\Delta p/p = (-1.50 \pm 0.21) \times 10^{-3}. \qquad (33)$$

The corresponding uncertainty on the m_W fits in the muon channel is 17 MeV.

VI. ELECTRON ENERGY MEASUREMENT

An electron's energy is measured from its shower in the electromagnetic calorimeter. We perform an initial data calibration by scaling the measured energy such that a Gaussian fit to the reconstructed dielectron mass in a region dominated by Z decays (86-98 GeV) gives a mean of 91 GeV. This is slightly below the world-average m_Z because the Gaussian fit is biased by the energy lost to final-state photon radiation (Section IX D). This initial data calibration is accurate to $\approx 0.15\%$.

To model the data, the simulated calorimeter energy is scaled to match the measured E/p distribution of electrons in $W \to e\nu$ events. A calibrated data measurement would result in an E/p of unity for electrons that do not radiate before entering the calorimeter, and deposit all of their energy in the EM calorimeter. We verify that the E/p calibration is unbiased by using it to measure m_Z in dielectron events. Given consistency of the measured m_Z with the world-average value, we incorporate the m_Z fit into the calibration. The final calibration has an accuracy of 0.037%.

A. E/p **Calibration**

We transfer the precise tracker calibration to the calorimeter using the ratio of electron calorimeter energy to track momentum, E/p. The material from the beam pipe to the inner COT wall causes bremsstrahlung that affects the measured position of the E/p peak, and this material is scaled such that the simulation matches the data in the high E/p region. The non-linearity of the energy scale is removed by applying a correction to the simulation scale as a function of the calorimeter shower p_T [Eq. (17)]. Finally, corrections are applied to the data to improve uniformity in response as a function of detector tower and time. After the complete set of corrections and simulation calibrations, the simulation energy scale S_E is determined from a maximum likelihood template fit to the E/p peak region.

The shape of the E/p distribution has a strong dependence on the material upstream of the COT. Bremsstrahlung in this material reduces the measured electron momentum in the tracker while leaving the measured calorimeter energy unchanged, since photons are radiated collinearly with the electron and deposit their energy in the same calorimeter tower as the electron. Thus, the effect of bremsstrahlung is to shift the measured E/p to values > 1. If the material were not well modeled, the energy scale calibration would be biased to compensate for the mismodeling.

A detailed accounting of the silicon and COT tracker material was performed at installation. In the early data-taking period, the radial distribution of photon conversions was compared between data and a full GEANT simulation. The amount of copper cable was increased by a few percent of X_0 in the GEANT simulation to correct observed discrepancies, and the three-dimensional lookup table of material properties (Section III B 1) was produced from this corrected GEANT simulation.

For a final material tuning, we compare our parametrized simulation to the data in the high E/p region ($1.19 \leq E/p < 1.85$) of electrons from W boson decays. Using the region $0.85 \leq E/p < 1.19$ for normalization, we perform a maximum likelihood fit to the $1.19 \leq E/p < 1.85$ region in two bins (Fig. 27) and measure a radiation length multiplicative correction factor of $S_{mat} = 1.004 \pm 0.009(\text{stat})$ [63]. As a further consistency check of the material lookup table, we determine S_{mat} as a function of tower $|\eta|$, and find no statistically significant dependence on $|\eta|$.

Our simulation of electron interactions in the tracker and calorimeter accounts for most of the energy dependence of the energy scale. Any residual non-linearity is incorporated as a per-particle cor-
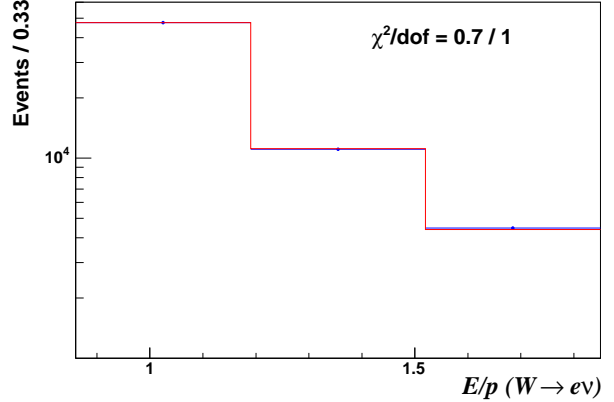

FIG. 27: The maximum likelihood fit to the tracker radiation length correction factor using the high E/p region ($1.19 \leq E/p < 1.85$) in $W \to e\nu$ data (points).

rection in the simulation (Section III B 2). To measure this non-linearity, we fit the E/p peak region ($0.93 \leq E/p < 1.11$) for the energy scale in bins of measured electron calorimeter p_T (Fig. 28). The resulting energy scale measurements are fit as a linear function of p_T, fixing the scale to 1 at the W boson sample's $\langle p_T^e \rangle = 39$ GeV. The error-weighted average, $\xi = [6 \pm 7(\text{stat})] \times 10^{-5}$, of the measurements of the non-linearity parameter from the W and Z boson samples is used in Eq. (17). The linear fits in Fig. 28, where the simulation includes this correction, show a constant energy scale [64].

To improve the energy resolution of the data, we apply time-dependent and tower-dependent calibrations derived from low-energy EM clusters. At level 3 the relevant trigger requires calorimeter and track p_T greater than 8 GeV each, as well as electron identification based on track-calorimeter matching and calorimeter shower shape properties. Offline, candidates are required to have Had/EM< 0.05 and $E + p > 22$ GeV to remove any trigger bias. Using the mean of the E/p range $0.8 - 1.25$, we apply relative corrections of $\mathcal{O}(3\%)$ to remove variations as functions of tower and time.

Because of bremsstrahlung radiation in the tracker, the mean E/p correction has a small bias that depends on the electron path length. Since the path length increases as $|\eta|$ increases, we perform a final $|\eta|$-dependent calibration of the data. Using template fits to the E/p peak region of the $W \to e\nu$ sample in bins of $|\eta|$, we derive a relative correction for each bin. This calibration removes $\approx 2\%$ residual variation in the calorimeter energy response.
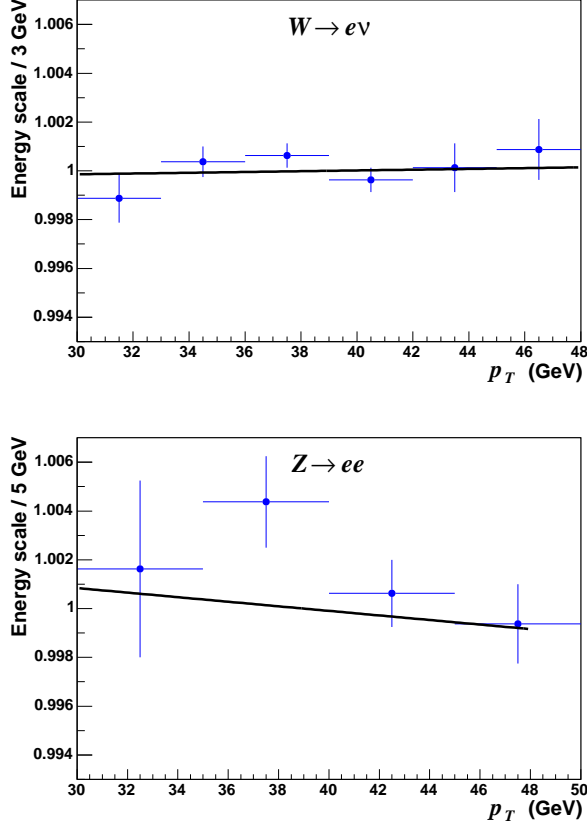
FIG. 29: The energy scale calibration using the peak E/p region ($0.93 \leq E/p < 1.11$, denoted by arrows) in $W \to e\nu$ data (points).
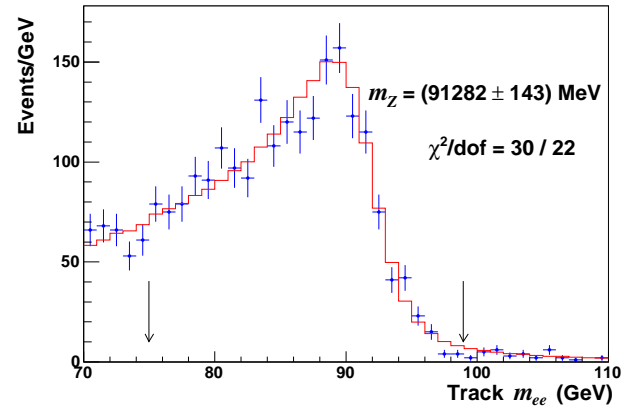

FIG. 28: The energy scale as a function of measured electron calorimeter p_T for W (top) and Z (bottom) boson decays. The fast simulation incorporates a per-particle non-linear response correction [Eq. (17)] . The combination of the linear fits to ξ results in no energy dependence of the energy scale.

FIG. 30: The m_Z fit to data (points) in the 75 GeV $< m_{ee} <$ 99 GeV region (denoted by arrows), using reconstructed track information only. The uncertainty is statistical only.

With the complete set of corrections applied to the data and simulation, we calibrate the simulation energy scale using $W \to e\nu$ events. The fit for S_E [Eq. (17)] to the E/p peak region (Fig. 29) has a statistical uncertainty of 0.025%. Including systematic uncertainties due to S_{mat} (± 0.011%) and the tracker momentum scale (± 0.021%), we obtain a total uncertainty of 0.034% on the E/p calibration of the electron energy scale.

The E/p calibration requires an accurate simulation of electron radiation in the tracker. We test the track simulation by measuring m_Z (Section VI B) using electron track information only. The measurement is a binned likelihood fit to the region 75 GeV $< m_{ee} <$ 99 GeV (Fig. 30), with m_Z as the fit parameter. Because of the significant radiated energy loss,

the test is less precise than the measurement using the calorimeter (Fig. 31). Nevertheless, we obtain good consistency with the world-average m_Z, verifying that we do not have any significant mismodeling of electron radiation in the tracker.

B. $Z \to ee$ Calibration

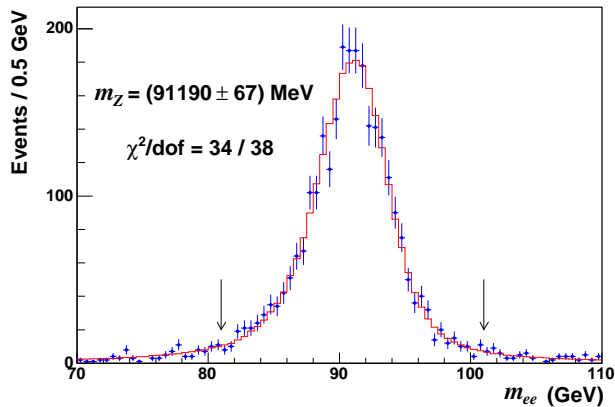Using the E/p-based calorimeter energy calibration, we measure the Z boson mass from its decay

FIG. 31: The m_Z fit to data (points) in the 81 GeV $< m_{ee} < 101$ GeV region (denoted by arrows). The uncertainty is statistical only.

to two electrons. After confirming consistency of the result with the world-average mass, we fix m_Z to this value and produce a combined calibration from the electron E/p-based method and $Z \rightarrow ee$ mass measurement.

We select Z bosons using the same single-electron trigger and offline electron selection as for the W boson sample (Sections III A 4 and IV B), and define candidates as oppositely-charged electrons with 66 GeV $< m_{ee} < 116$ GeV and $p_T^{ee} < 30$ GeV. The Z boson sample contains 2,919 events in (218.1 ± 12.4) pb^{-1} of data.

The sample includes a small component of multijet and $W+$ jet background. From a comparison of the data with like-sign electrons to a prediction of the full GEANT simulation, we estimate the background fraction to be $\lesssim 0.5\%$. Since $\langle m_{ee} \rangle$ of the background is ≈ 2 GeV less than that of the Z boson sample in the fit region, we estimate any corresponding bias on the measured m_Z to be $\lesssim 10$ MeV.

The model for Z boson production and decay to electrons is the same as for the muon decay channel (Section V D). We use the RESBOS [61] event generator and a next-to-leading order QED calculation of photon radiation from the final-state electrons [62] (Section IX). We include the virtual photon exchange and Z/γ^* interference contributions as fixed "backgrounds" to the Z boson lineshape, and determine m_Z from a binned likelihood fit to the data in the range 81 GeV $< m_{ee} < 101$ GeV (Fig. 31).

Systematic uncertainties on the m_Z measurement result from the E/p calibration (29 MeV), calorimeter non-linearity measurement (23 MeV), and higher-

order QED radiation (14 MeV). The measured $m_Z = [91.190 \pm 0.067(\text{stat})]$ GeV is consistent with the world-average value $m_Z = (91.188 \pm 0.002)$ GeV [11], given the total uncertainty of 78 MeV on the measurement.

The uncorrelated uncertainties in the combination of the m_Z and E/p calibrations are the uncertainty on the non-linearity parameter ξ, the statistical uncertainty on the m_Z measurement (0.073%), and the uncertainty on the E/p calibration (0.034%). Since the m_W fit relies predominantly on the shape of the Jacobian edge of the m_T distribution, the relevant electron transverse energies are in the $\approx 40 - 45$ GeV range. The uncertainty on the energy dependence of the scale from the Z boson mass is negligible, as the $\langle p_T^e \rangle$ is about 42 GeV in this sample. The E/p-based calibration involves an extrapolation from $\langle p_T^e \rangle = 39$ GeV, so it receives an additional uncertainty contribution of 23 MeV to the m_W measurement from the non-linearity parameter ξ. Combining the two calibrations, we obtain a total electron energy measurement uncertainty of 30 MeV on the m_W measurement in the electron channel. Of this uncertainty, we take 17 MeV to be 100% correlated with the muon channel through the momentum scale uncertainty.

VII. RECOIL MEASUREMENT

The recoil $\vec{u}_T$ (Fig. 5) in a W boson event results from quark or gluon radiation in the initial state, and from photon radiation in the initial and final states. A quark or gluon typically fragments into multiple hadrons, which are detected in the calorimeter. Additional energy from the underlying event is also measured in the calorimeter and obscures the recoil measurement. Rather than rely on detailed modeling of the underlying event, we develop an empirical model of the recoil $\vec{u}_T$ using Z boson events, where the four-momentum of the Z boson is measured precisely using its leptonic decays. The model of the recoil energy measurement is tuned with these decays and applied to W boson events.

We measure the recoil energy using all calorimeter towers except those with ionization or shower energy from the charged leptons. To reduce potential bias and facilitate our model parametrization, we correct the measured energy in each tower for acceptance differences resulting from an uncentered beam. In addition, we improve the measurement resolution by correcting for response differences between the central and plug calorimeters.
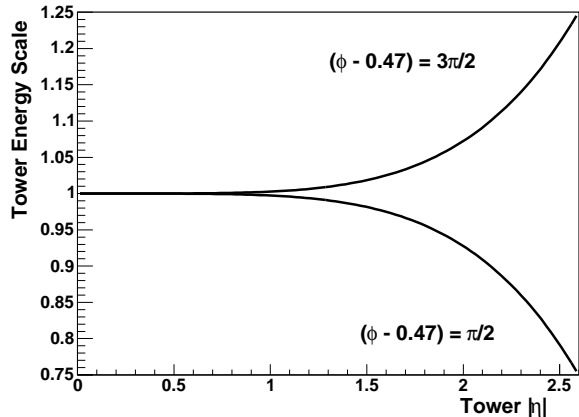
FIG. 32: The maximal energy correction factors applied to each tower as a function of $|\eta|$. The decreasing curve corresponds to towers closest to the beam line, and the increasing curve corresponds to towers on the opposite side. The correction factors reduce the ϕ variation in acceptance due to the beam line displacement from the detector axis.

A. Data Corrections

The data used in this analysis have a relative offset of about 4 mm between the beam line and the center of the CDF II detector. This results in a variation in calorimeter acceptance as a function of ϕ such that the calorimeter towers closest to the beam line have a larger acceptance, and thus a larger average measured energy per tower. The variation is largest in the forward region, where the towers are in closest proximity to the beam line. We suppress this azimuthal energy variation by applying a threshold on the combined EM and hadronic tower p_T of 5 GeV for towers with detector $|\eta| > 2.6$. The threshold strongly suppresses the forward tower energy variation in W boson events, while retaining the energy from high-p_T hadronic jets in multijet events. All other towers have EM and hadronic energy thresholds of 20 MeV each.

We reduce the residual azimuthal energy variation by applying a multiplicative correction factor to each measured tower energy according to the following empirical function (Fig. 32):

$$S_{tower} = 1 - 0.6(0.32|\eta|)^{4.74}\sin(\phi - 0.47). \quad (34)$$

This correction is determined using events collected by a minimum bias trigger, which requires evidence of an inelastic $p\bar{p}$ collision (Section III A 5).

The relative energy scale between the central and forward calorimeters is initially determined from the calibration of high-p_T hadronic jets. The relative response has a significant energy dependence, however, and the initial calibration is not optimized for the low p_T particles relevant to the W boson recoil measurement. Using the E/p distribution of charged pions from minimum bias events, we find that a relative energy scale of $\approx 12\%$ between central and forward calorimeters is appropriate for particles with $p_T \lesssim 2$ GeV, the momentum region of a typical recoil particle. To maintain the mean recoil energy scale, we scale the central (forward) calorimeter tower energies up (down) by 5% (7%). This calibration improves the recoil resolution, and thus the statistical precision of the m_W fits. It also minimizes the sensitivity of the recoil model to differences in phase space sampled by the selected W and Z boson decays.

B. Lepton Tower Removal

The recoil $\vec{u}_T$ is measured as the sum of corrected $\vec{p}_T$ in all calorimeter towers (Sec. VII A), excluding the towers in which the lepton(s) deposit energy. The exclusion of these towers also removes some recoil energy from the measurement, thus causing a bias in $u_{||}$. We measure this bias from the data and incorporate it in the simulation.

An electron shower typically distributes energy to two calorimeter towers, but can also contribute to a third tower if the electron is near a tower edge. We remove each tower neighboring the electron's tower, as well as the corner towers closest to the electron's CES position (Fig. 33). A muon near a tower edge can cross two towers, so we remove the two towers in η neighboring the muon's tower (Fig. 34). The tower window definitions are motivated by the presence of excess energy in a given tower above the background energy from the underlying event.

We estimate the recoil energy flow into the excluded towers, denoted by $\Delta u_{||}$, using equivalent windows separated in ϕ from the lepton in $W \to l\nu$ events. When simulating a W or Z boson event, we correct the simulated $\vec{u}_T$ by a $\Delta u_{||}$ taken from the measured distribution. The simulated $\Delta u_{||}$ incorporates its measured dependence on $u_{||}$ and $u_\perp$, and lepton $|\eta|$. These dependencies are shown for $W \to \mu\nu$ events in Fig. 35 and similar functions are defined for electrons. The incorporation of these functions preserves $\langle\Delta u_{||}\rangle$, which is 269 MeV for electrons and 112 MeV for muons (with negligible statistical uncertainty).

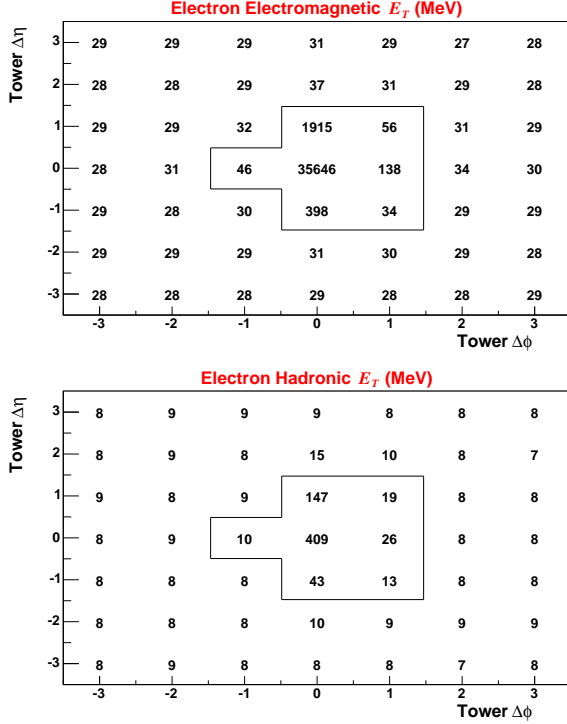To estimate the systematic uncertainty associated with modeling the tower removal, we study the varia-

Electron Electromagnetic E_T (MeV)

Tower $\Delta\eta$ \ Tower $\Delta\phi$	-3	-2	-1	0	1	2	3
3	29	29	29	31	29	27	28
2	28	28	29	37	31	29	28
1	29	29	32	1915	56	31	29
0	28	31	46	35646	138	34	30
-1	29	28	30	398	34	29	29
-2	29	29	29	31	30	29	28
-3	28	28	28	29	28	28	29

Muon Electromagnetic E_T (MeV)

Tower $\Delta\eta$ \ Tower $\Delta\phi$	-3	-2	-1	0	1	2	3
3	28	27	28	29	28	27	27
2	28	27	29	32	29	28	28
1	28	29	30	49	33	29	28
0	29	28	30	332	37	29	29
-1	28	28	30	35	31	28	29
-2	28	27	29	30	29	29	27
-3	28	28	30	29	28	27	28

Electron Hadronic E_T (MeV)

Tower $\Delta\eta$ \ Tower $\Delta\phi$	-3	-2	-1	0	1	2	3
3	8	9	9	9	8	8	8
2	8	9	8	15	10	8	7
1	9	8	9	147	19	8	8
0	8	9	10	409	26	8	8
-1	8	8	8	43	13	8	8
-2	8	8	8	10	9	9	9
-3	8	9	8	8	8	7	8

Muon Hadronic E_T (MeV)

Tower $\Delta\eta$ \ Tower $\Delta\phi$	-3	-2	-1	0	1	2	3
3	8	7	8	8	8	8	8
2	7	7	8	9	8	8	8
1	8	8	8	432	9	8	8
0	9	8	9	1255	11	8	8
-1	8	9	9	83	9	8	8
-2	8	8	8	8	8	7	8
-3	8	8	8	7	8	9	8

FIG. 33: The average energy collected in the electromagnetic (top) and hadronic (bottom) calorimeters in the vicinity of the electron shower in W boson decays. The differences $\Delta\phi$ and $\Delta\eta$ are signed such that positive differences correspond to towers closest to the electron position at shower maximum. The central seven towers inside the box are removed from the recoil measurement. Statistical uncertainties on the values outside the box are $\mathcal{O}(1$ MeV$)$.
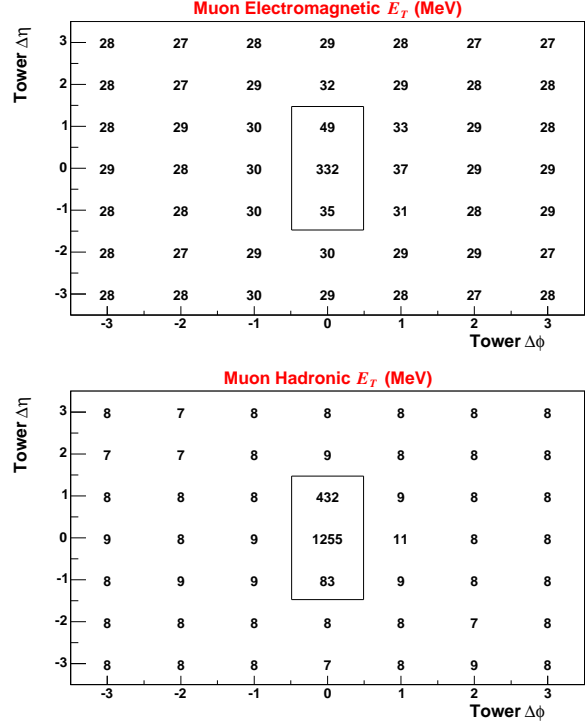
FIG. 34: The average energy collected in the electromagnetic (top) and hadronic (bottom) calorimeters in the vicinity of the muon in W boson decays. The differences $\Delta\phi$ and $\Delta\eta$ are signed such that positive differences correspond to towers closest to the muon position at the shower maximum detector. The central three towers inside the box are removed from the recoil measurement. Statistical uncertainties on the values outside the box are $\mathcal{O}(1$ MeV$)$.

tion of $\Delta u_{||}$ in the data as a function of the ϕ separation from the lepton of the equivalent tower window. We take half the variation as a systematic uncertainty: 8 (5) MeV for removed electron (muon) towers. To confirm our estimate of this uncertainty, we remove an additional window azimuthally opposite to the lepton ($\Delta\phi = \pi$), incorporate its model into the simulation, and compare the resulting simulation and data $u_{||}$ distributions. We find the differences to be consistent within our quoted uncertainties.

C. Recoil Model Parametrization

The recoil consists of three separate components: radiation in the W or Z boson production; radiation from the spectator partons; and energy from additional $p\bar{p}$ collisions in a given bunch crossing. We use the RESBOS [61] generator to predict the net p_T distri-

bution of radiation in the W or Z boson production, and minimum bias data for the p_T distribution from spectator partons and additional interactions. The parameters for the detector response to the recoil are measured in Z boson events.

To facilitate tuning of the recoil model, we define axes such that quark and gluon radiation lies predominantly along one axis, denoted as the "η" axis (Fig. 36). This axis is chosen to be the angular bisector of the two leptons, whose angles are precisely measured. The orthogonal axis is denoted as the "ξ" axis.

1. Recoil Energy Scale

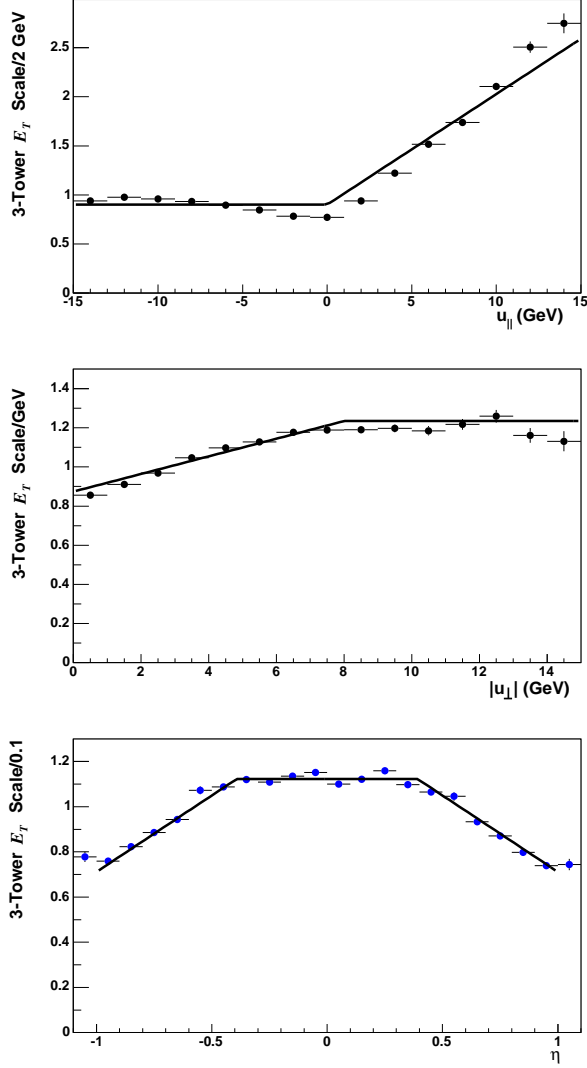We tune the simulation to match the observed detector response to the recoil radiation. The recoil re-

FIG. 35: The scales applied to the energy in the three
removed muon towers in the simulation (solid lines), as
functions of $u_{||}$ (top), $u_{\perp}$ (middle), and η (bottom). The
points show the scales measured using towers separated in
ϕ from the muon in $W \to \mu\nu$ data. The scaling functions
for removed electron towers have similar shapes.

FIG. 36: The definitions of the η and ξ axes in Z boson
events. The quark and gluon radiation from the boson
production points predominantly in the $-\eta$ direction.

stants determined from the data. Figure 37 shows
$-\vec{u}_T^{\,meas} \cdot \vec{p}_T^{\,\mu\mu}/p_T^{\mu\mu}$, which approximates R, for Z bo-
son decays to muons. The response R is less than 1
due to calorimeter energy loss from particles curling
in the tracker, particles passing through calorimeter
cracks, and non-linearity of the hadronic calorimeter
response.

Projecting the lepton momenta and the recoil along
the η axis to obtain p_η^{ll} and u_η, the sum $p_\eta^{ll}+u_\eta$ is sen-
sitive to R. This sum is zero for $R = 1$, and positive
for $R < 1$. We measure $A = 0.635 \pm 0.007(\text{stat})$ and
$B = 6.68 \pm 1.04(\text{stat})$ by minimizing the combined
χ^2 of the electron and muon $(p_\eta^{ll} + u_\eta)$ distributions
as a function of p_T^{ll} (Fig. 38). We determine A and B
with the $(p_\eta^{ll} + u_\eta)$ distribution rather than the distri-
bution of Fig. 37 because $(p_\eta^{ll} + u_\eta)$ is well-defined as
$p_T^Z \to 0$ GeV, while R is not. The parameters A and
B are statistically uncorrelated by construction. We
apply $R(A, B)$ to the generated recoil $\vec{u}_T$ in simulated
W and Z boson events.

2. Spectator and Additional $p\bar{p}$ Interactions

The net $\vec{p}_T$ flow from spectator quarks and ad-
ditional interactions is negligible due to momentum
conservation. However, detector resolution causes
its measurement to generally be non-zero. The res-
olution is predominantly determined by the energy
sampling in the calorimeter, and we expect it to in-
crease as the square root of the scalar sum $\sum p_T$ of
the calorimeter tower p_T. We plot the width of the
$\not{p}_T$ distribution, projected along the x and y axes, as
a function of the $\sum p_T$ in minimum bias data. We
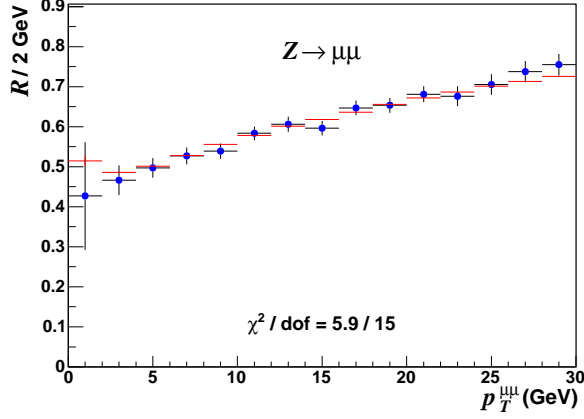parametrize the dependence as a power law, with the

sponse is defined as $R \equiv \vec{u}_T^{\,meas} \cdot \vec{u}_T^{\,true}/u_T^{true}$, where
$\vec{u}_T^{\,true} = -\vec{p}_T^Z$ is the generated net $\vec{p}_T$ of the initial-
state-radiation, and $\vec{u}_T^{\,meas}$ is the reconstructed vec-
tor of this transverse momentum.

To simulate the measured recoil, we parametrize
the response as

$$R(A, B) = A \ln(u_T^{true} + B)/\ln(15 + B), \quad (35)$$

where u_T^{true} is in units of GeV, and A and B are con-

FIG. 37: The mean $-\vec{u}_T^{\,meas}\cdot\vec{p}_T^{\,\mu\mu}/p_T^{\mu\mu}$, which approximates the recoil response R, as a function of dimuon p_T for $m_{\mu\mu}$ in the Z boson mass region. The simulation (solid) uses parameters fit from the electron and muon $p_\eta^{ll}+u_\eta$ distributions, and models the data (circles) well.

fitted result:

$$\sigma_{x,y}=0.3842\left(\sum p_T\right)^{0.5333}\ \text{GeV}, \qquad (36)$$

where $\sum p_T$ is defined in units of GeV. The distribution of $\sum p_T$ from additional interactions, denoted P_{MB}, is parametrized as (Fig. 39):

$$P_{MB}\left(\sum p_T\right)\propto\left(\sum p_T\right)^{0.325}e^{-\sum p_T/19.98}, \quad (37)$$

with constants obtained from a fit to the minimum bias data. In our simulation, we draw a value of $\sum p_T$ from this distribution, for the fraction of events containing at least one $p\bar{p}$ collision beyond that producing the W or Z boson. This fraction is calculated from the average instantaneous luminosity of 2.137 $(2.014)\times10^{31}$ cm^{-2} s^{-1} for W and Z boson data in the muon (electron) channel, and the assumed instantaneous luminosity per additional collision $(3.3\times10^{31}$ cm^{-2} s$^{-1})$.

The observed $\sum p_T$ from spectator partons in the $p\bar{p}\to W$ or Z boson interaction is modeled from the minimum bias data, which correspond to one or more $p\bar{p}$ collisions. We deconvolute the $\sum p_T$ spectrum of Eqn. 37 with the distribution of the number of collisions in minimum bias data to derive the following single-collision $\sum p_T$ distribution $P_{1-col.}$ applicable to W or Z production (Fig. 39):

$$P_{1-col.}\left(\sum p_T\right)\propto\left(\sum p_T\right)^{0.345}e^{-\sum p_T/14.27}. \quad (38)$$
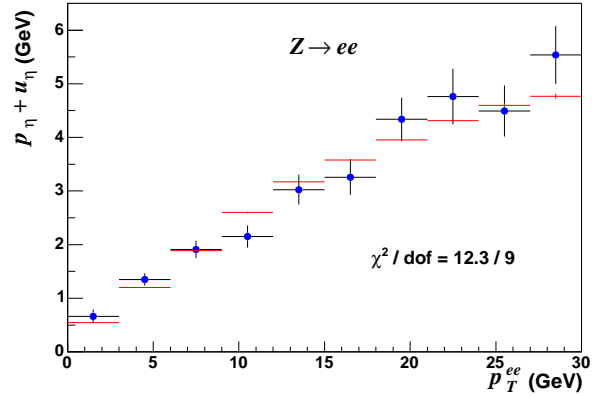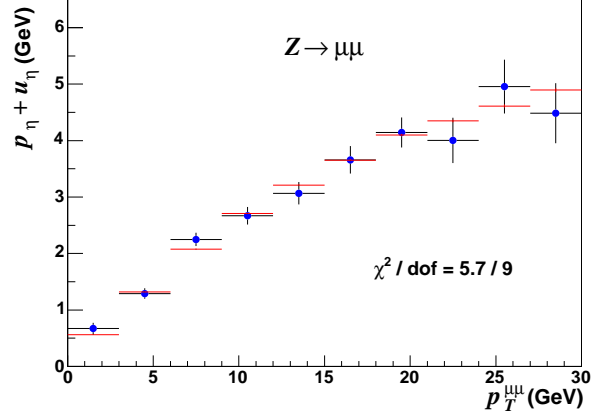
FIG. 38: The simulation (solid) and data (circles) distributions of $(p_\eta^{ll}+u_\eta)$ for Z boson decays to muons (top) and electrons (bottom). The combined χ^2 is minimized in the fit for the recoil detector response parameters.

The $\sum p_T$ produced in a single minimum bias collision can be different from that produced by the spectator partons in W or Z boson production. In order to allow for a difference, we scale the $\sum p_T$ drawn from the single-collision spectrum by a parameter $N_{W,Z}$, which we tune on the Z boson data.

With this model, the $\sum p_T$ in a simulated event is obtained by adding the contributions from the spectator partons and the additional interactions. The corresponding recoil resolution is generated according to Eqn. 36, with a single tunable parameter $N_{W,Z}$.

3. Recoil Energy Resolution

The measurement of the quark and gluon radiation is affected by detector energy resolution, which in
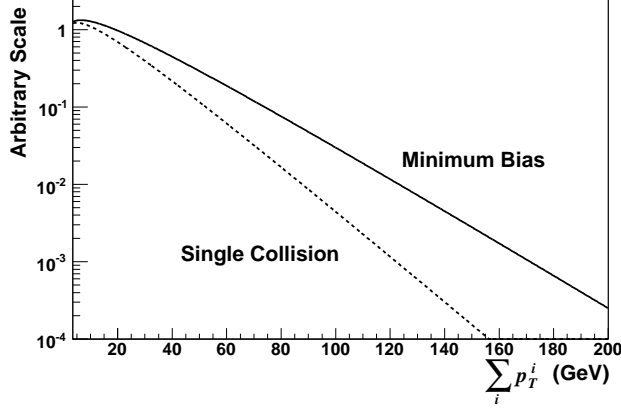
FIG. 39: The $\sum_i p_T^i$ distribution for minimum bias data (solid) and a single $p\bar{p}$ collision (dashed), as derived from the minimum bias distribution.

turn affects the measured recoil direction. We model the recoil angular resolution as a Gaussian distribution with $\sigma_\phi = 0.14 \pm 0.01$(stat), determined from fits to the $\Delta\phi(\vec{u}_T, -\vec{p}_T^{\,ll})$ distribution in Z boson events (Fig. 40). Since the lepton directions are precisely measured, the width of the peak at $\Delta\phi = 0$ is dominated by the recoil angular resolution.

The energy resolution of the quark and gluon radiation is predominantly determined by stochastic fluctuations in the hadronic calorimeter, which motivate the functional form $\sigma_{u_T} \propto \sqrt{u_T^{true}}$. We measure the proportionality constant s_{hard} using Z boson data.

To tune s_{hard} and $N_{W,Z}$, we project the momentum imbalance $\vec{p}_T^{\,ll} + \vec{u}_T$ along the η and ξ axes in Z boson decays (Fig. 41). The width of these projections as a function of p_T^{ll} provides information on $N_{W,Z}$ and s_{hard}. At low p_T^Z the resolution is dominantly affected by $N_{W,Z}$, with the s_{hard} contribution increasing as the boson p_T increases. We compare the widths of the data and simulation projections as a function of p_T^{ll} and compute the χ^2. Minimizing this χ^2, we obtain $N_{W,Z} = 1.167 \pm 0.026$(stat) and $s_{hard} = [0.828 \pm 0.028(\text{stat})]$ GeV$^{1/2}$. The tuning is performed such that the statistical uncertainties on these parameters are uncorrelated.

D. Recoil Model Cross-Checks

The full recoil model, with parameters tuned from Z boson events, is applied to the simulated W boson sample. We compare the data to the predictions of distributions that can affect the final mass measure-
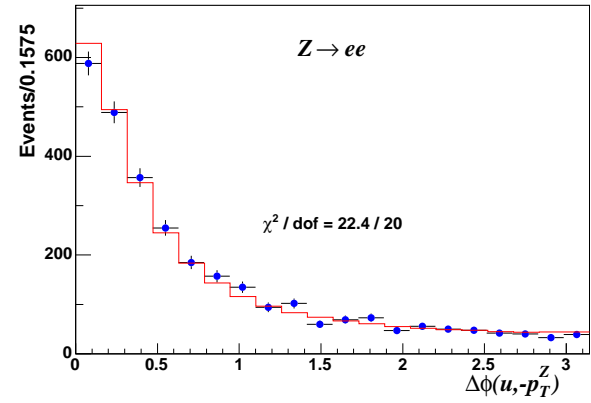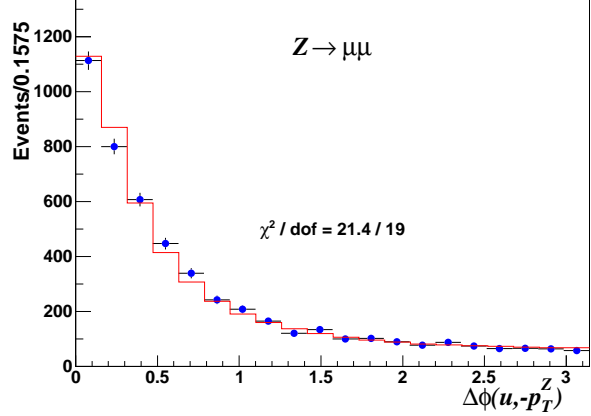
FIG. 40: The angle between the measured recoil and the direction opposite p_T^Z, for simulation (histogram) and data (circles) events where the Z boson decays to muons (top) or electrons (bottom). The χ^2 from the $Z \to \mu\mu$ sample is minimized in the fit to the recoil angular resolution. The corresponding uncertainty on m_W is negligible.

ment: the projections of the recoil along $(u_{||})$ and perpendicular to $(u_\perp)$ the charged lepton; and the total recoil u_T.

The $u_{||}$ distribution is directly affected by the measurements of lepton efficiency as a function of $u_{||}$ (Figs. 14 and 16) and the modeling of lepton tower removal (Figs. 33 and 34). The $u_{||}$ is also sensitive to the boson p_T (Sec. IX B) and decay angular distributions, and to the recoil response and resolutions.

Since u_T is much less than the charged lepton p_T for our event selection, $\not{p}_T \approx |p_T + u_{||}|$. Thus, m_T can be written as:

$$m_T \approx 2p_T\sqrt{1 + u_{||}/p_T} \approx 2p_T + u_{||}. \qquad (39)$$
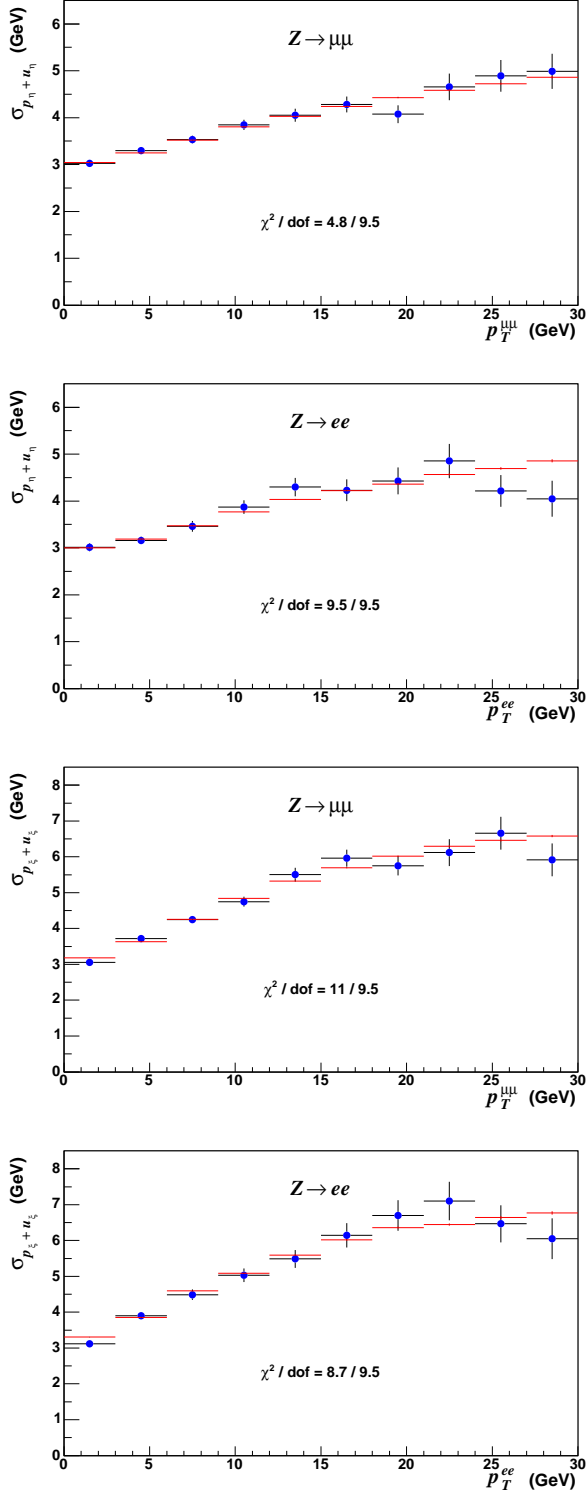
To a good approximation, any bias in $u_{||}$ directly en-

FIG. 41: The simulation (solid) and data (circles) $p^{ll}_\eta + u_\eta$ (top) and $p^{ll}_\xi + u_\xi$ (bottom) resolutions for Z boson decays to muons and electrons. The sum of the four χ^2 values is minimized in the fit for the recoil resolution parameters $N_{W,Z}$ and s_{hard}. Since there are four distributions and two fit parameters, each distribution contributes half a degree of freedom to the fit.
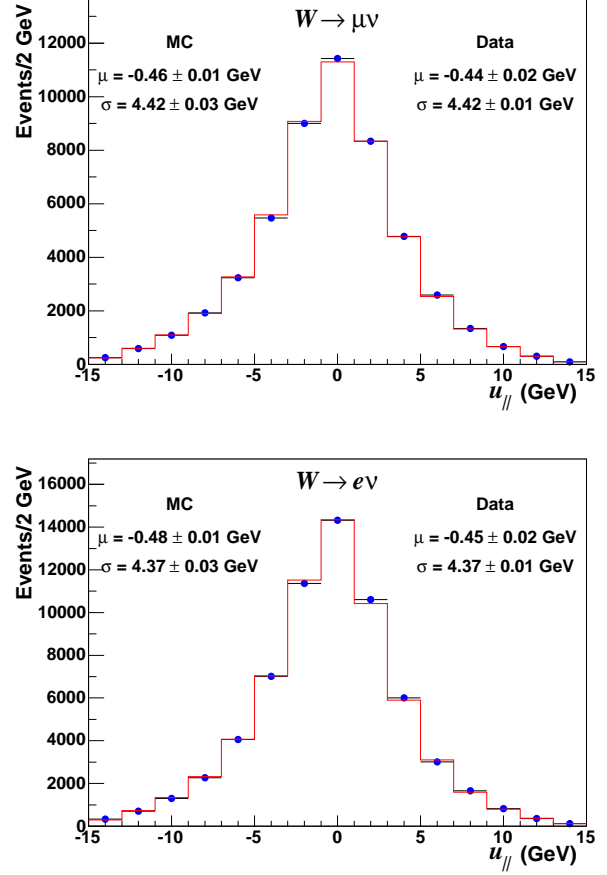

FIG. 42: The simulation (solid) and data (circles) $u_{||}$ distributions for W boson decays to $\mu\nu$ (top) and $e\nu$ (bottom). The simulation uses parameters fit from Z boson data, and the uncertainty on the simulation is due to the statistical uncertainty on these parameters. The data mean (μ) and RMS (σ) are well-modeled by the simulation.

ters as a bias in the m_T fit. We compare the $u_{||}$ distributions in data and simulation $u_{||}$ in Fig. 42, and observe no evidence of a bias at the level of the data statistics and simulation systematics derived from the recoil model parameters. All backgrounds (Section VIII) are included in the comparison, except $W \to \tau\nu$, which has similar distributions to the other W leptonic decays.

The $u_\perp$ distribution is dominantly affected by the recoil resolution, with a smaller contribution from the recoil response. The simulation models this distribution well for both $W \to e\nu$ and $W \to \mu\nu$ samples (Fig. 43).

The mean of the u_T distribution is sensitive to the
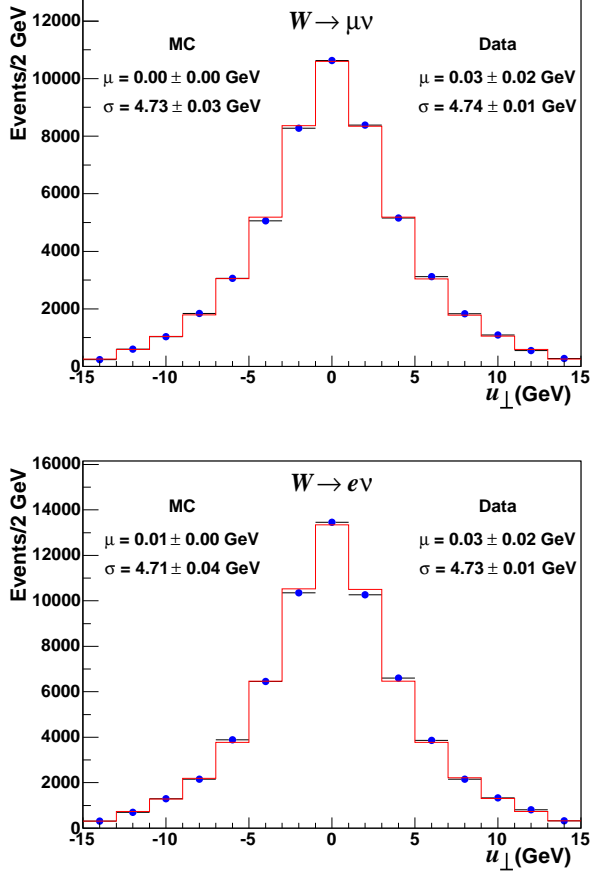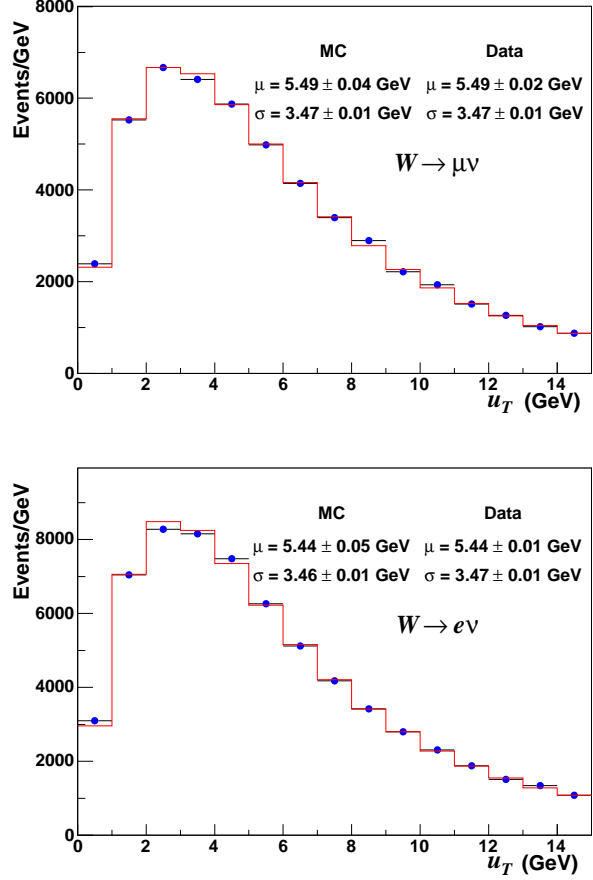
FIG. 43: The simulation (solid) and data (circles) $u_\perp$ distributions for W boson decays to $\mu\nu$ (top) and $e\nu$ (bottom). The simulation uses parameters fit from Z boson data, and the uncertainty on the simulation is due to the statistical uncertainty on these parameters. The data mean (μ) and RMS (σ) are well-modeled by the simulation.

FIG. 44: The simulation (solid) and data (circles) u_T distributions for W boson decays to $\mu\nu$ (top) and $e\nu$ (bottom). The simulation uses parameters fit from Z boson data, and the uncertainty on the simulation is due to the statistical uncertainty on these parameters. The data mean (μ) and RMS (σ) are well-modeled by the simulation.

recoil response and the boson p_T, and is affected to a lesser extent by the resolution. The reverse is the case for the RMS of the u_T distribution. Both are modeled well by the simulation for both $W \rightarrow e\nu$ and $W \rightarrow \mu\nu$ samples (Fig. 44).

The uncertainties on the m_W fits from the recoil parameters (Table V) are determined by varying each parameter by $\pm 3\sigma$ and assuming linear variation of the fit m_W with the parameter. Since all uncertainties are uncorrelated, we add them in quadrature to obtain total recoil model uncertainties of 12, 17, and 34 MeV on m_W from the m_T, p_T, and $\not{p}_T$ fits, respectively. The uncertainties are the same and 100% correlated for the electron and muon channels, since

the recoil parameters are obtained from combined fits to $Z \rightarrow ee$ and $Z \rightarrow \mu\mu$ data. The uncertainty on the p_T fit arises predominantly from the modeling of the $u_T < 15$ GeV threshold used to select W boson events (Section IV).

VIII. BACKGROUNDS

The event selection criteria (Section IV) result in W boson samples with high purity. However, the small residual backgrounds affect the distributions used for the m_W fits. Both the $W \rightarrow e\nu$ and $W \rightarrow \mu\nu$ samples receive contributions from: $Z/\gamma^* \rightarrow ll$,

Input	Shift (MeV)		
parameter	m_T	p_T	$\not{p}_T$
A	-9	-8	2
B	-2	15	15
$N_{W,Z}$	5	0	22
s_{hard}	5	-3	21

TABLE V: Signed shifts in the m_W fits due to 1σ increases in the recoil model parameters.

where one lepton is not detected; $W \to \tau\nu$, where the τ decay products are reconstructed as a charged lepton; and multijet production, where at least one jet is misreconstructed. The $W \to \mu\nu$ sample also contains backgrounds from cosmic rays, where a muon passing through the COT is reconstructed on only one side of the COT, and long-lived hadrons decaying to $\mu\nu X$, where the muon momentum is misreconstructed.

A. $W \to e\nu$ Backgrounds

We model the $W \to \tau\nu$ and $Z/\gamma^* \to ee$ backgrounds using events generated with PYTHIA [59] and simulated with a full GEANT-based detector simulation [40, 41]. The full simulation models global detector inefficiencies and is thus more appropriate for predicting background normalizations than the custom fast simulation. The multijet background is estimated using a data-based approach.

In the standard model the branching ratio for $W \to e\nu$ is the same as for $W \to \tau\nu$, neglecting lepton masses. Measurements from LEP [19] test this prediction with a precision of 2.9%, and a slight discrepancy from the standard model is observed with a significance of 2.6σ. In estimating the $W \to \tau\nu$ background, we assume the standard model prediction and determine the ratio of $W \to \tau\nu$ to $W \to e\nu$ events from the ratio of acceptances of these two processes, as determined by the full GEANT-based detector simulation. We include an uncertainty of 2.9%, corresponding to the statistical precision of the tests of this assumption. We estimate the $W \to \tau\nu$ background to be $(0.93 \pm 0.03)\%$ of the $W \to e\nu$ sample.

The Z/γ^* background is determined from the ratio of $Z/\gamma^* \to ee$ to $W \to e\nu$ acceptances determined from the GEANT-based detector simulation, multiplied by the corresponding ratio of cross sections times branching ratios. The ratio $\sigma \cdot BR(Z \to ee)/\sigma \cdot BR(W \to e\nu)$ has been calculated in the standard model to be 10.69 ± 0.08 [25] [26], and measurements are consistent with this value [26] [56]
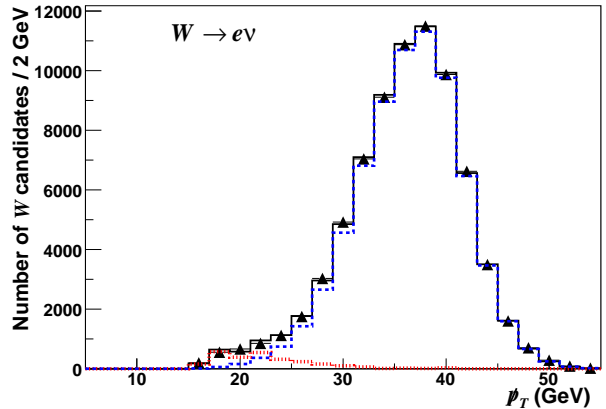

FIG. 45: The $\not{p}_T$ distribution of the $W \to e\nu$ candidate sample (triangles) and prediction (solid), with the $\not{p}_T$ and m_T selection cuts removed. We fit for the normalization of the hadronic jet background (dotted) after fixing the normalization of the $W \to e\nu$ distribution (dashed) in the peak. Not shown are the $Z/\gamma^* \to ee$ and $W \to \tau\nu$ backgrounds, whose relative normalizations are fixed from the simulation.

[65]. We take an uncertainty of ± 0.43 on this value from the CDF Run I measurement, and estimate the $Z/\gamma^* \to ee$ background in the $W \to e\nu$ candidate sample to be $(0.24 \pm 0.01)\%$.

Multijet background enters the signal data sample when a hadronic jet is misreconstructed as an electron and a second jet results in large $\not{p}_T$ through energy misreconstruction or the semi-leptonic decay of a hadron. To estimate this background, we remove the $\not{p}_T$ threshold in our signal event selection to include the background-dominated kinematic region of low $\not{p}_T$. We then fit the observed $\not{p}_T$ spectrum to the combination of the hadronic jet, $W \to e\nu$, $Z/\gamma^* \to ee$, and $W \to \tau\nu$ components, floating only the hadronic jet shape normalization (Fig. 45).

In this fit, the shapes and normalizations for the $W \to e\nu$, $Z/\gamma^* \to ee$, and $W \to \tau\nu$ components are determined from the GEANT-based simulation. The shape of the $\not{p}_T$ spectrum of the hadronic jet background is determined from the single-electron events that pass an anti-electron identification requirement based on a neural network discriminant NN. The discriminant is determined by combining the electron quality variables (Section IV B) into a neural network [66] trained with single-electron data events, using $\not{p}_T$ to separate signal from background.

Electron candidates in the $W \to e\nu$ sample with low NN values have a high probability to be jets

misreconstructed as electrons. Events with such candidates provide a $\not{p}_T$ distribution characteristic of hadronic jet production. We apply a small correction to this distribution to account for the expected contribution from $W \to e\nu$ decay electrons with low NN values.

This method relies on the assumption that the hadronic jet background has a $\not{p}_T$ distribution that is independent of the electron identification variables. As a test of this assumption, we perform the same fit for the jet background normalization, using only the isolation variable (Section IV A) instead of the NN to select a hadronic jet subsample. We take a weighted average of the two fitted background normalizations, and assign an uncertainty that covers the range of the two results. The resulting background estimate is $(0.25 \pm 0.15)\%$ of the $W \to e\nu$ sample.

The m_T, p_T, and $\not{p}_T$ distributions are obtained from the GEANT-based simulation for W and Z boson backgrounds, and from events in the $W \to e\nu$ sample with low-NN electron candidates for the hadronic jet background. We fit these distributions (Fig. 46) and include their shapes and relative normalizations in the m_W template fits. The uncertainties on the background estimates result in uncertainties of 8, 9, and 7 MeV on m_W from the m_T, p_T, and $\not{p}_T$ fits, respectively (Table VI).

	% of	δm_W (MeV)		
Background	$W \to e\nu$ data	m_T fit	p_T fit	$\not{p}_T$ fit
$W \to \tau\nu$	0.93 ± 0.03	2	2	2
Hadronic jets	0.25 ± 0.15	8	9	7
$Z/\gamma^* \to ee$	0.24 ± 0.01	1	1	0
Total	1.42 ± 0.15	8	9	7

TABLE VI: The percentages of the various backgrounds in the $W \to e\nu$ data set, and the corresponding uncertainties on the m_T, p_T and $\not{p}_T$ fits for m_W.

B. $W \to \mu\nu$ Backgrounds

The $W \to \tau\nu$ and $Z/\gamma^* \to \mu\mu$ backgrounds are modeled using events generated with PYTHIA [59] and simulated with the GEANT [40]-based detector simulation. We use the data to estimate backgrounds from cosmic rays, multijets, and hadrons decaying in flight to $\mu\nu X$.

Backgrounds from $W \to \tau\nu$ and $Z/\gamma^* \to \mu\mu$ to the $W \to \mu\nu$ sample are modeled in the same manner as for the $W \to e\nu$ sample (Section VIII A). We determine the ratio of the acceptance for $W \to \tau\nu$
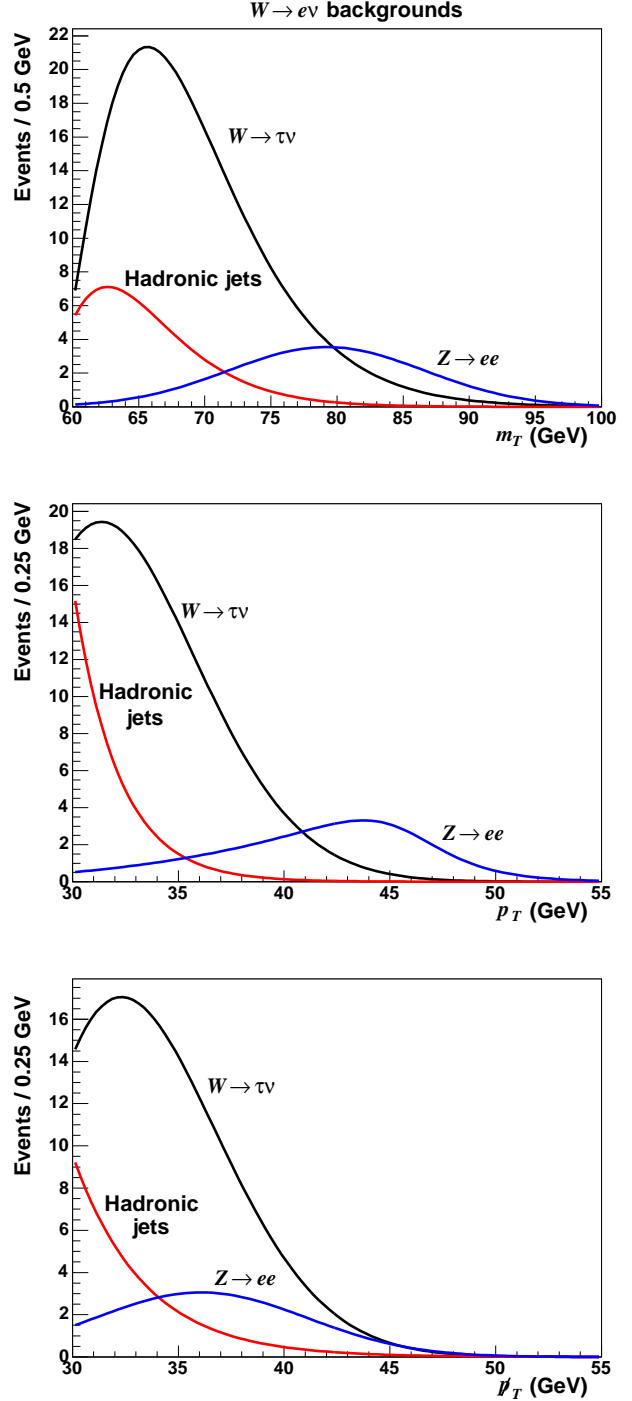

FIG. 46: The parametrizations of the backgrounds to the $W \to e\nu$ data sample. The backgrounds to the m_T (top), p_T (middle), and $\not{p}_T$ (bottom) distributions are included in the m_W fits.

or $Z/\gamma^* \to \mu\mu$ events to the acceptance for $W \to \mu\nu$ events using the GEANT-based detector simulation. We assume equal branching ratios for the two W boson decay modes, and use the ratio $\sigma \cdot BR(Z \to \mu\mu)/\sigma \cdot BR(W \to \mu\nu) = 10.69 \pm 0.43$ (Section VIII A). We estimate the fraction of $W \to \tau\nu$ $(Z/\gamma^* \to \mu\mu)$ events in the $W \to \mu\nu$ candidate sample to be $(0.89 \pm 0.02)\%$ $[(6.6 \pm 0.3)\%]$. The $Z/\gamma^* \to \mu\mu$ background is large because our event selection does not identify muons with $|\eta| \gtrsim 1.2$. The tracker and muon detectors have incomplete or no coverage in the forward rapidity region, and the muons deposit only a few GeV of energy in the calorimeter. Thus, a $Z/\gamma^* \to \mu\mu$ event with one central and one forward muon is measured as a single-muon event with large $\not{p}_T$.

Cosmic-ray muons passing close to the beam line are a source of background to the $W \to \mu\nu$ sample when the muon track is reconstructed on only one side of the COT. The cosmic-ray identification algorithm [57] searches for unreconstructed tracks and removes cosmic rays with high efficiency. The residual cosmic-ray background is estimated using the reconstructed interaction time t_0 and impact parameter d_0 from the COT track fit. Figure 47 compares the t_0 distributions of the $W \to \mu\nu$ candidate sample, $Z/\gamma^* \to \mu\mu$ candidates, and identified cosmic rays. The cosmic ray fraction is fit by minimizing the χ^2 of the sum of the $Z/\gamma^* \to \mu\mu$ and cosmic ray distributions with respect to the $W \to \mu\nu$ distribution. We obtain an alternative background estimate by comparing the d_0 distribution of identified cosmic rays to the d_0 distribution of $W \to \mu\nu$ candidates with the d_0 selection cut removed. The high impact parameter region of the W boson sample is enriched with cosmic rays, and is used to estimate the cosmic ray background within the selection region $|d_0| < 1$ mm. We take the cosmic-ray background to be $(0.05 \pm 0.05)\%$, where the uncertainty covers the range of results from the two estimates.

Decay of a long-lived meson to a muon can result in a reconstructed track with high momentum and large event $\not{p}_T$. A low-momentum pion or kaon $(\lesssim 10$ GeV$)$ that decays in the tracking chamber can be reconstructed as a high-momentum muon if the decay is in an azimuthal direction opposite the meson's curvature (i.e., a kink in the trajectory). Such misreconstruction typically results in a poor COT track χ^2 and a large impact parameter. For each of these quantities we obtain a prompt muon distribution from Z boson decays and a meson decay-in-flight distribution from the W boson sample by requiring either high COT track χ^2 or high impact parameter. We fit for the background fraction by summing the
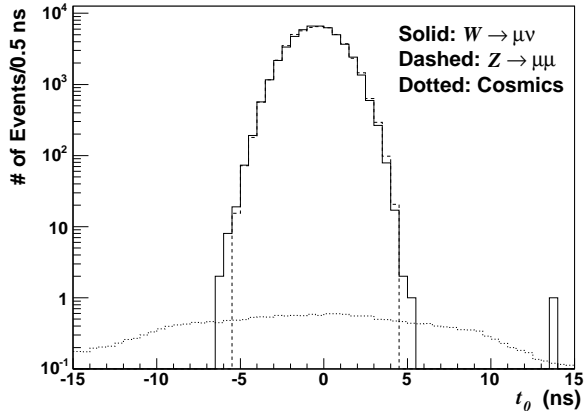

FIG. 47: The t_0 distributions for $W \to \mu\nu$ candidates (solid), $Z \to \mu\mu$ candidates (dashed), and identified cosmic rays (dotted). For comparison, the distribution from Z candidates has been normalized to that of the W candidates, while the cosmic distribution has been normalized to 0.05% of the W boson sample.

prompt muon distribution with the decay-in-flight distribution, and minimizing the χ^2 with respect to the muon distribution from the W boson sample. We obtain a background fraction of $(0.3 \pm 0.2)\%$, where the uncertainty covers the range of the estimates obtained using the COT track χ^2 and impact parameter distributions.

A separate class of hadronic background results from high-momentum muons from short-lived hadronic decays, or energetic hadrons penetrating the calorimeter to the muon detectors. These background muon candidates are typically accompanied by significant hadronic energy due to an associated hadronic jet, and can be separated using a muon isolation variable. Two such variables are determined by using either calorimeter energy or track momenta in an $\eta - \phi$ cone of size 0.4 surrounding the muon candidate. Using the low $\not{p}_T$ region to select a jet-dominated sample, we fit the track and calorimeter isolation distributions of the W boson candidate sample to the sum of the expected distributions from $Z \to \mu\mu$ events and jet-dominated events. As a third method, we fit the $\not{p}_T$ distribution, using muon candidates with high-isolation values to provide the $\not{p}_T$ distribution of the hadronic-jet background. From the range of results of the three methods, we obtain a jet background estimate of $(0.1 \pm 0.1)\%$.

The distributions for the m_W fit variables are obtained from the GEANT-based simulation for W and Z boson backgrounds, from identified cosmic ray events

for the cosmic ray background, and from events in the $W \to \mu\nu$ sample with high-χ^2 (isolation) muons for the decay-in-flight (hadronic jet) background. Including uncertainties on the shapes of the distributions, the total uncertainties on the background estimates result in uncertainties of 9, 19, and 11 MeV on m_W from the m_T, p_T, and $\not{p}_T$ fits, respectively (Table VII).

	% of	δm_W (MeV)		
Background	$W \to \mu\nu$ data	m_T fit	p_T fit	$\not{p}_T$ fit
$Z/\gamma^* \to \mu\mu$	6.6 ± 0.3	6	11	5
$W \to \tau\nu$	0.89 ± 0.02	1	7	8
Decays in flight	0.3 ± 0.2	5	13	3
Hadronic jets	0.1 ± 0.1	2	3	4
Cosmic rays	0.05 ± 0.05	2	2	1
Total	7.9 ± 0.4	9	19	11

TABLE VII: The percentages of the various backgrounds in the $W \to \mu\nu$ data set, and the corresponding uncertainties on the m_T, p_T and $\not{p}_T$ fits for m_W.

IX. PRODUCTION AND DECAY MODELS

The measurement of the W boson mass relies on a complete model of W and Z boson production and decay. The production process is described by perturbative QCD and a parametrization of non-perturbative QCD effects, with parameters determined from global fits to hadron-hadron and lepton-hadron collision data. W and Z boson decay are modeled using a next-to-leading-order electroweak calculation and includes QCD corrections for the lepton angular distributions, as a function of boson p_T. The most important process in the decay is photon radiation off the final-state charged lepton, which has been calculated at next-to-leading order [62].

A. Parton Distribution Functions

The longitudinal momentum of the produced W or Z boson depends on the momenta of the interacting partons. These momenta, generally expressed in terms of the fractions x_i of the colliding (anti-)proton energies, are not known on an event-by-event basis. The x_i parton distribution functions (PDFs) are however well constrained by hadron-hadron and lepton-hadron collision data. The distributions have been parametrized as simple functional forms for the quarks, antiquarks, and gluons inside a proton. Two
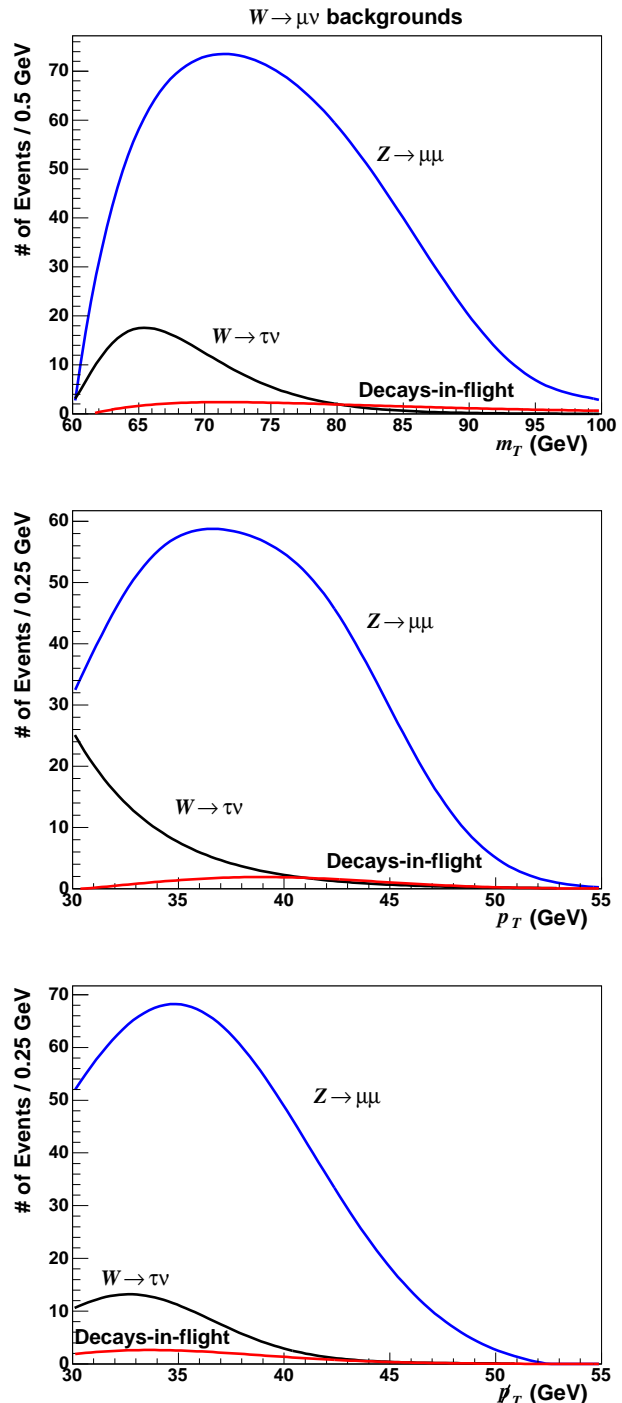

FIG. 48: The parametrizations of the backgrounds to the $W \to \mu\nu$ data sample. The backgrounds to the m_T (top), p_T (middle), and $\not{p}_T$ (bottom) distributions are included in the m_W fits. Not shown are the small hadronic-jet and cosmic-ray background distributions.

independent fits to the global data, performed by the MRST [23] and CTEQ [24] collaborations, constrain the parameters in these PDFs.

We model the quark momentum fractions using the next-to-leading-order CTEQ6M parton distribution functions. The CTEQ parametrization [24] for most of the distribution functions inside the proton is:

$$x_p f_a(x_p, Q_0) = A_0 x_p^{A_1}(1 - x_p)^{A_2} e^{A_3 x_p}(1 + A_4 x_p)^{A_5}, \quad (40)$$

where f_a are the distributions of a particular quark or gluon combination a, A_i are the fit parameters, and Q_0 is the energy scale at which the parameters are defined. The functions at a particular energy scale Q are determined by a perturbative evolution calculation known as the DGLAP equation [67].

The uncertainty on the m_W measurement arising from uncertainties on the PDF parameters is determined using a set of 40 PDFs provided by the CTEQ collaboration. The set covers the $\pm 1.6\sigma$ (90% C.L.) uncertainties [68] for the eigenvectors of the parametrization. The mass shift of a particular $+1.6\sigma$ PDF, relative to the corresponding -1.6σ PDF, determines the uncertainty due to that eigenvector. We calculate the total PDF uncertainty using the quadrature sum of all eigenvector contributions [24]:

$$\delta m_W^{PDF} = \frac{1}{1.6}\left[\frac{1}{2}\sqrt{\sum_i (m_W^{i+} - m_W^{i-})^2}\right], \quad (41)$$

where $m_W^{i\pm}$ represents the mass fits for the $\pm 1.6\sigma$ shifts in eigenvector i. These fits are performed using templates and simulated pseudoexperiments both generated with PYTHIA [59]. The resulting δm_W^{PDF} are 11, 9, and 13 MeV, for the m_T, p_T, and $\not{p}_T$ fits, respectively. A fit to pseudodata using the MRST PDF set results in m_W shifts smaller than these uncertainties.

B. W and Z Boson p_T

Because mass is a Lorentz invariant, the W boson transverse mass is only weakly sensitive to the W boson transverse momentum p_T^W. However, the decay lepton p_T spectra are more significantly affected by the p_T^W distribution.

At the Tevatron, the p_T spectra of W and Z bosons peak at a few GeV (Fig. 49), where the shapes are predominantly determined by non-perturbative QCD interactions. We model the distribution with the RESBOS generator [61], which uses the Collins-Soper-Sterman (CSS) [69] resummation formalism and a

parametrized non-perturbative form factor. In this formalism, the cross section for W boson production is written as:

$$\frac{d\sigma(p\bar{p} \to W + X)}{d\hat{s}\, d^2\vec{p}_T^W\, dy} = \frac{1}{2\pi^2}\delta(\hat{s} - m_W^2)\int d^2 b\, e^{i\vec{p}_T^W \cdot \vec{b}}$$
$$\times \tilde{W}_{j\bar{k}}(\vec{b}, \hat{s}, x_i) + Y(p_T^W, \hat{s}, x_i), \quad (42)$$

where x_i are the parton energy fractions of the (anti-)proton, $y = 0.5\ln(x_p/x_{\bar{p}})$ is the boson rapidity, $\vec{b}$ is the relative impact parameter of the partons in the collision, Y is a function calculable at fixed order, and $\tilde{W}$ can be separated into its perturbative and non-perturbative components. We use the Brock-Landry-Nadolsky-Yuan (BLNY) form for the non-perturbative component:

$$\tilde{W}_{j\bar{k}}^{NP} = e^{[g_1 - g_2\ln(\frac{Q}{2Q_0}) - g_1 g_3 \ln(100 x_p x_{\bar{p}})]b^2}, \quad (43)$$

where $Q_0 = 1.6$ GeV and g_i are parameters suggested by the CSS formalism to be universal to processes with initial state quarks and colorless objects in the final state [61].

The g_2 parameter affects the position of the most probable p_T^W and is the most relevant for the m_W measurement. We use $g_1 = 0.21$ GeV^2, $g_2 = 0.68$ GeV^2, and $g_3 = -0.60$, which are determined from fits to global Drell-Yan data [61]. We verify the applicability of these values to our data by fitting the dilepton p_T distribution (Fig. 49) for g_2. We find $g_2 = [0.685 \pm 0.048(\text{stat})]$ GeV^2, consistent with the global fits. Varying g_2 by $\pm 3\sigma$ in pseudoexperiments and taking the fit m_W to be linearly dependent on g_2, we find that the uncertainty of $\delta g_2 = 0.048$ GeV^2 results in uncertainties of 3, 9, and 5 MeV, on m_W for the m_T, p_T, and $\not{p}_T$ fits, respectively. These uncertainties are the same and 100% correlated between the electron and muon channels, since g_2 is fit using $Z \to ee$ and $Z \to \mu\mu$. Neglecting correlations between PDFs and the g_i parameters, we find that uncertainties on the other g_i do not significantly affect the m_W measurement.

C. W Boson Decay

The m_W measurement is sensitive to the charged lepton decay angle relative to the boson p_T. The mismodeling of this angle can bias the projection of the recoil along the lepton ($u_{||}$), which in turn affects m_W measured from the m_T fit (Section VII D).

The lepton decay angle is predicted by the matrix element calculation in the RESBOS generator, which
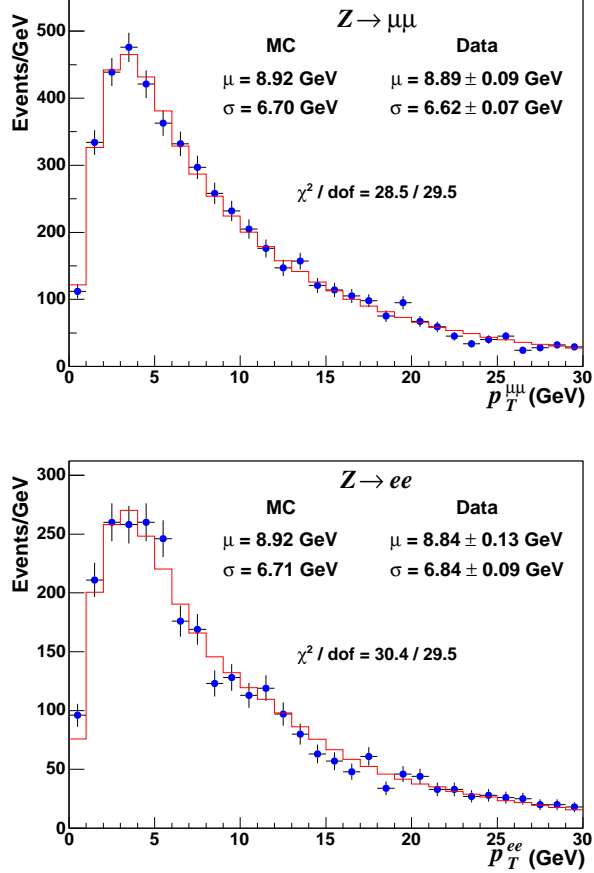
FIG. 49: The simulation (solid) and data (circles) p_T^Z distributions for Z boson decays to $\mu\mu$ (top) and ee (bottom). The distributions are used to fit for the non-perturbative parameter g_2, which determines the most probable value of p_T^Z. Since there are two distributions for one fit parameter, each distribution contributes half of a degree of freedom. The mean (μ) and RMS (σ) are consistent between data and simulation.

computes the differential cross section $\frac{d^4\sigma}{dp_T^W \, dy_W \, dQ^2 d\Omega}$. The angular distributions are defined in the Collins-Soper rest frame of the W boson [70]. In this frame, the z-axis is defined to bisect the angle between the proton momentum and the opposite of the antiproton momentum.

The angular component of the differential cross sec-

tion can be written as [71],

$$\frac{d\sigma}{d\Omega} \propto (1 + \cos^2\theta) + \frac{1}{2}A_0(1 - 3\cos^2\theta)$$
$$+ A_1 \sin 2\theta \cos\phi + \frac{1}{2}A_2 \sin^2\theta \cos 2\phi$$
$$+ A_3 \sin\theta \cos\phi + A_4 \cos\theta + A_5 \sin^2\theta \sin 2\phi$$
$$+ A_6 \sin 2\theta \sin\phi + A_7 \sin\theta \sin\phi, \qquad (44)$$

where the $A_i(p_T^W, y_W)$ have been calculated to NLO in α_s. Because of the $V - A$ structure of the electroweak interaction, for leading-order valence quark interactions all A_i are zero except $A_4 = 2$. The A_i can be determined experimentally through a moments analysis [72] of the lepton angle in the Collins-Soper frame.

We have performed a moments analysis to extract the A_i from the RESBOS generator, and compared the results to those obtained [72] from the DYRAD event generator [73], which produces $W+$ jet events to order α_s^2. The two generators give consistent results in the overlapping region 15 GeV $< p_T^W <$ 100 GeV.

D. Photon Radiation

The quarks, the W boson, and charged lepton have non-zero electromagnetic charge and can radiate photons in the W boson production process. Radiation off the initial-state quarks and the W boson propagator have a negligible effect on the invariant mass distribution of the W boson. Radiation off the final-state charged lepton reduces the measured transverse mass (relative to the W boson mass) and must be accurately modelled.

We study photon radiation using the WGRAD event generator [62], which models the full next-to-leading-order (NLO) electroweak physics. The generator allows an independent study of photon radiation from the initial-state quarks (ISR), the W boson propagator, and the final-state charged lepton (FSR). Interference between the contributing diagrams can also be studied independently. We verify that the initial-state, propagator, and interference effects do not affect the measured W boson mass, within the 5 MeV statistical uncertainty of the simulation.

We simulate final-state photon radiation in our RESBOS-generated W and Z boson events by generating a photon for each charged lepton. The energy and angular spectra are taken from the WGRAD generator using the appropriate boson mass. To avoid the infrared divergence that arises when the photon momentum goes to zero, we require $E_\gamma > \delta_s \sqrt{\hat{s}}/2$, where $\delta_s = 10^{-4}$. We find that increasing δ_s to 10^{-3}
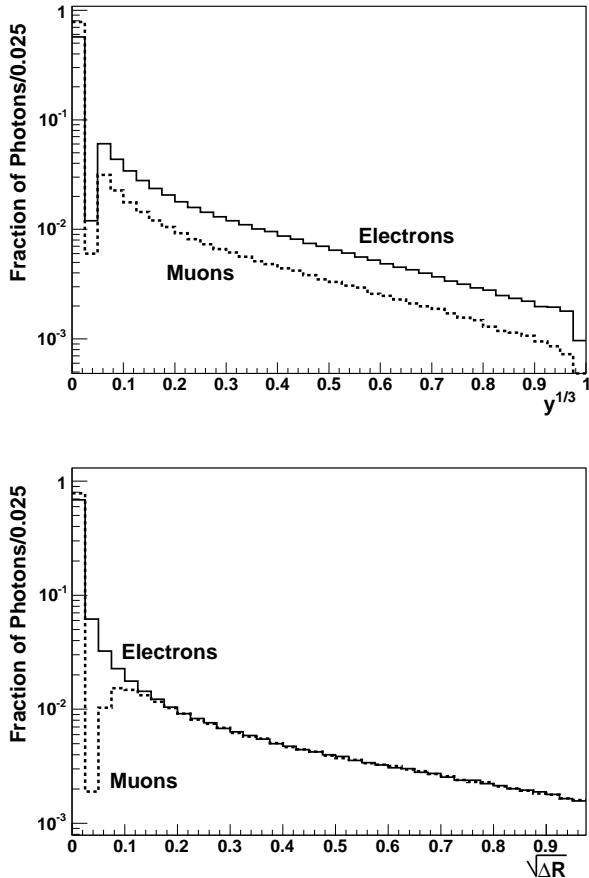
Fit	$\delta m_{W,Z}(\mu)$ (MeV)	$\delta m_{W,Z}(e)$ (MeV)
m_T	-158	-138
p_T	-206	-186
$\not{p}_T$	-77	-59
m_{ll}	-196	-215

TABLE VIII: The mass shifts obtained by fitting events generated with our simulation of single-photon radiation to templates generated without final-state photon radiation. The shifts are for the W boson m_T, p_T, and $\not{p}_T$ fits, and for the Z boson m_{ll} fit. The shifts have statistical uncertainties of 7 MeV each.

FIG. 50: The cube root of the fraction of electron (solid) or muon (dashed) momentum contained in the radiated photon (top), and the square root of the angle ΔR (bottom) between the radiated photon and the electron (solid) or muon (dashed).

does not affect the m_W measurement, at the level of the 5 MeV statistical precision of the tests.

The energy of a photon in a given event is calculated from the fraction $y = E_\gamma/E_l$. The photon angle $\Delta R = \sqrt{(\Delta\eta)^2 + (\Delta\phi)^2}$ is taken with respect to the charged lepton. To improve the phase space sampling, we sample from a two-dimensional distribution of the variables $\sqrt{\Delta R}$ and $y^{1/3}$ when selecting a photon. The individual distributions of these variables are shown in Fig. 50.

We validate our photon simulation by fitting a sample of events generated with FSR using WGRAD to templates generated with leading-order WGRAD and photons simulated according to our model. We find our FSR model to be consistent with that of WGRAD at the level of the 5 MeV statistical precision of the

test. The total effect of including FSR is shown in Table VIII. Since FSR reduces the charged lepton momentum, the shift is largest for the p_T fit and smallest for the $\not{p}_T$ fit. The effects are smaller for electrons than for muons because the electron calorimeter energy measurement recovers much of the energy of FSR photons.

We approximate the effect of next-to-next-to-leading-order FSR by increasing the photon's momentum fraction (y) by 10%, consistent with the results of a study of higher-order photon radiation [74]. We take half the correction as a systematic uncertainty to account for higher-order QED effects.

The total uncertainty due to photon radiation is the quadrature sum of: uncertainties on ISR, interference between ISR and FSR, and radiation off the propagator (5 MeV); uncertainty due to the infrared cutoff of the FSR photon (5 MeV); the FSR model (5 MeV); and uncertainties on higher-order FSR corrections (7 MeV for the electron and 8 MeV for the muon m_T fits). The total uncertainties are 12 (11), 13 (13), and 10 (9) MeV, for the muon (electron) m_T, p_T, and $\not{p}_T$ fits, respectively.

X. W BOSON MASS FITS

We fit the W boson data distributions to a sum of background and simulated signal templates of the m_T, p_T, and $\not{p}_T$ distributions, fixing the normalization of the sum to the number of data events. The fit minimizes the negative log likelihood (Section II D) as a function of the template parameter m_W, which is defined by the relativistic Breit-Wigner mass distribution [11]:

$$\frac{d\sigma}{dm} \propto \frac{m^2}{(m^2 - m_W^2)^2 + m^4\Gamma_W^2/m_W^2}, \qquad (45)$$

where m is the invariant mass of the propagator. The

likelihood is calculated in m_W steps of 1 MeV. We use the standard model W boson width $\Gamma_W = 2.094$ GeV, which has an accuracy of 2 MeV and is calculated for $m_W = 80.393$ GeV. Using pseudoexperiments, we find the input Γ_W affects the fit m_W according to the relation $dm_W/d\Gamma_W = 0.14 \pm 0.04$.

A. Fit Results

The results of the m_T fits are shown in Fig. 51, and Table IX gives a summary of the 68% confidence level uncertainties associated with the fits. We fit for m_W in the range 65 GeV $< m_T <$ 90 GeV, where the fit range has been chosen to minimize the total uncertainty on m_W. The p_T and $\not{p}_T$ distributions are fit in the range 32 GeV $< p_T <$ 48 GeV (Figs. 52 and 53, respectively) and have uncertainties shown in Tables X and XI, respectively. We show the individual fit results in Table XII, and the negative log-likelihoods of all fits in Fig. 54.

m_T Fit Uncertainties			
Source	$W \to \mu\nu$	$W \to e\nu$	Correlation
Tracker Momentum Scale	17	17	100%
Calorimeter Energy Scale	0	25	0%
Lepton Resolution	3	9	0%
Lepton Efficiency	1	3	0%
Lepton Tower Removal	5	8	100%
Recoil Scale	9	9	100%
Recoil Resolution	7	7	100%
Backgrounds	9	8	0%
PDFs	11	11	100%
W Boson p_T	3	3	100%
Photon Radiation	12	11	100%
Statistical	54	48	0%
Total	60	62	-

TABLE IX: Uncertainties in units of MeV on the transverse mass fit for m_W in the $W \to \mu\nu$ and $W \to e\nu$ samples.

We combine results from the $W \to \mu\nu$ and $W \to e\nu$ fits using the Best Linear Unbiased Estimator (BLUE) [75]. The BLUE algorithm defines a procedure for constructing a complete covariance matrix using the derivative of m_W with respect to each model parameter [18]. We construct this matrix assuming each source of systematic uncertainty is independent of any other source of uncertainty. The resulting covariance matrix (Table XIII) is then used
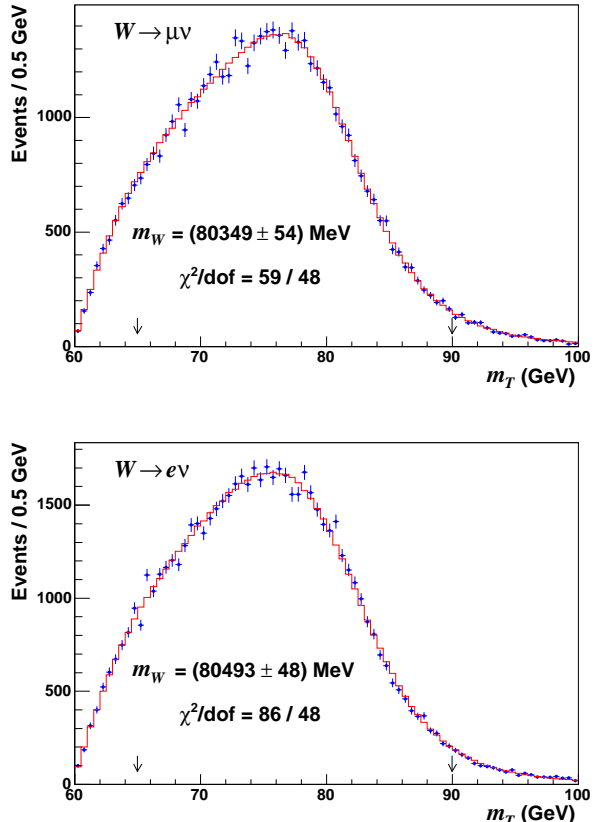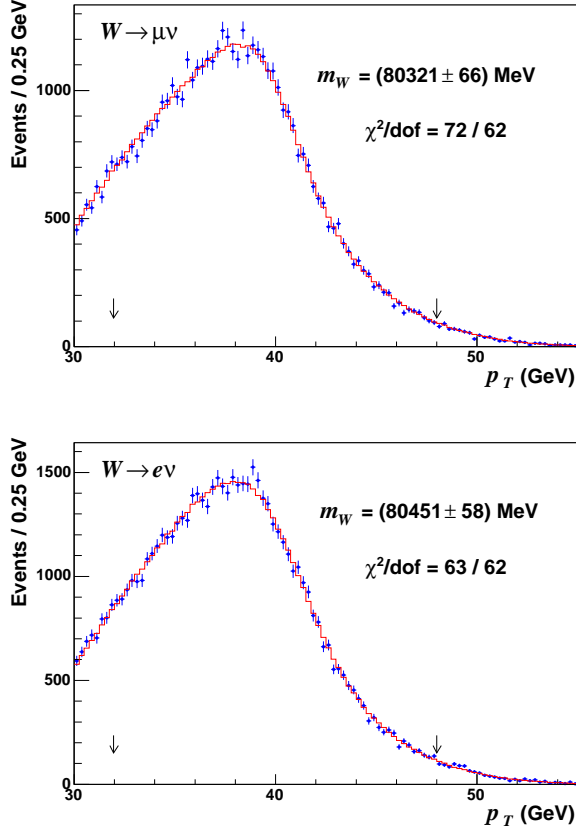

FIG. 51: The simulation (solid) and data (points) m_T distributions for W boson decays to $\mu\nu$ (top) and $e\nu$ (bottom). The simulation corresponds to the best-fit m_W, determined using events between the two arrows. The uncertainty is statistical only. The large χ^2 for the electron fit is due to individual bin fluctuations (Fig. 55) and does not bias the fit result, as evidenced by the small change in the fit m_W when the fit window is varied (Fig. 58).

to combine all six m_W fits. When combining any subset of fits, the appropriate smaller covariance matrix is used.

The result of combining the m_W fits to the m_T distribution in the $W \to \mu\nu$ and $W \to e\nu$ channels is

$$m_W = 80.417 \pm 0.048 \text{ GeV.} \qquad (46)$$

The χ^2/dof of the combination is 3.2/1 and the probability that two measurements of the same quantity would have a χ^2/dof at least as large as this is 7%.

The combination of the fits to the p_T distribution yields

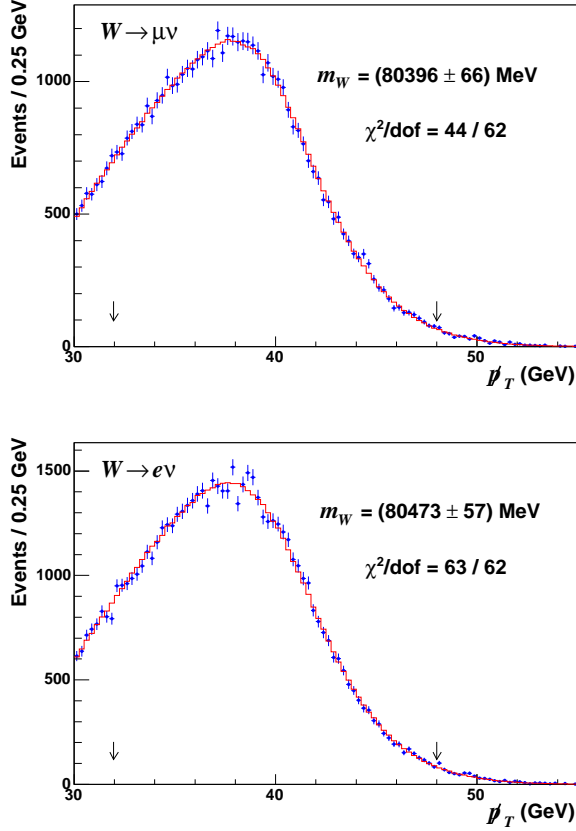$$m_W = 80.388 \pm 0.059 \text{ GeV,} \qquad (47)$$

FIG. 52: The simulation (solid) and data (points) p_T distributions for W boson decays to $\mu\nu$ (top) and $e\nu$ (bottom). The simulation corresponds to the best-fit m_W, determined using events between the two arrows. The uncertainty is statistical only.

with a $\chi^2/$dof of 1.8/1 and an 18% probability for the two measurements to obtain a $\chi^2/$dof ≥ 1.8.

The results of the fits to the $\not p_T$ distribution gives

$$m_W = 80.434 \pm 0.065 \text{ GeV}, \qquad (48)$$

with a 43% probability of obtaining a $\chi^2/$dof at least as large as observed (0.6/1).

Combining the m_T, p_T, and $\not p_T$ fits within the individual decay channels gives $m_W = (80.352 \pm 0.060)$ GeV with a $\chi^2/$dof of 1.4/2 for the $W \rightarrow \mu\nu$ channel and $m_W = (80.477 \pm 0.062)$ GeV with a $\chi^2/$dof of 0.8/2 for the $W \rightarrow e\nu$ channel.

We combine the six fits with the BLUE procedure to obtain our final result of

$$m_W = 80.413 \pm 0.048 \text{ GeV}, \qquad (49)$$

which has statistical and systematic uncertainties of 34 MeV each. The statistical correlations between

p_T Fit Uncertainties			
Source	$W \rightarrow \mu\nu$	$W \rightarrow e\nu$	Correlation
Tracker Momentum Scale	17	17	100%
Calorimeter Energy Scale	0	25	0%
Lepton Resolution	3	9	0%
Lepton Efficiency	6	5	0%
Lepton Tower Removal	0	0	0%
Recoil Scale	17	17	100%
Recoil Resolution	3	3	100%
Backgrounds	19	9	0%
PDFs	20	20	100%
W Boson p_T	9	9	100%
Photon Radiation	13	13	100%
Statistical	66	58	0%
Total	77	73	-

TABLE X: Uncertainties in units of MeV on the charged lepton transverse momentum fit for m_W in the $W \rightarrow \mu\nu$ and $W \rightarrow e\nu$ samples.

$\not p_T$ Fit Uncertainties			
Source	$W \rightarrow \mu\nu$	$W \rightarrow e\nu$	Correlation
Tracker Momentum Scale	17	17	100%
Calorimeter Energy Scale	0	25	0%
Lepton Resolution	5	9	0%
Lepton Efficiency	13	16	0%
Lepton Tower Removal	10	16	100%
Recoil Scale	15	15	100%
Recoil Resolution	30	30	100%
Backgrounds	11	7	0%
PDFs	13	13	100%
W Boson p_T	5	5	100%
Photon Radiation	10	9	100%
Statistical	66	57	0%
Total	80	79	-

TABLE XI: Uncertainties in units of MeV on the missing transverse momentum fit for m_W in the $W \rightarrow \mu\nu$ and $W \rightarrow e\nu$ samples.

the fits, determined from simulation pseudoexperiments, are shown in Table XIV. The relative weights of the fits are 47.7% (32.3%), 3.4% (8.9%), 0.9% (6.8%) for the m_T, p_T and $\not p_T$ fit distributions, respectively, in the muon (electron) channel. The combination establishes an *a priori* procedure to incorporate all the information from individual fits, and yields a $\chi^2/$dof of 4.8/5. The probability to obtain a
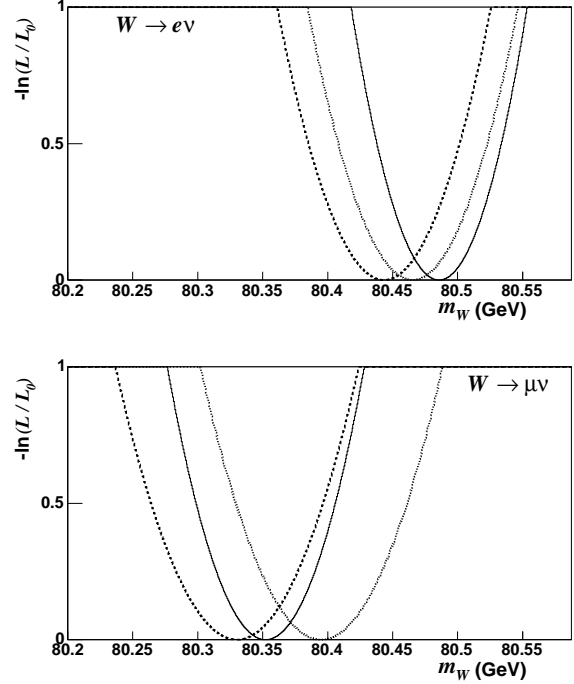
FIG. 54: The negative log of the likelihood ratio $\mathcal{L}/\mathcal{L}_0$, where $\mathcal{L}_0$ is the maximum likelihood, as a function of m_W for the m_T (solid), p_T (dashed), and $\not{p}_T$ (dotted) fits in the electron (top) and muon (bottom) channels.

FIG. 53: The simulation (solid) and data (points) $\not{p}_T$ distributions for W boson decays to $\mu\nu$ (top) and $e\nu$ (bottom). The simulation corresponds to the best-fit m_W, determined using events between the two arrows. The uncertainty is statistical only.

	$m_T(e,\nu)$	$m_T(\mu,\nu)$	$p_T(e)$	$p_T(\mu)$	$\not{p}_T\,(e)$	$\not{p}_T\,(\mu)$
$m_T(e,\nu)$	64^2	27^2	61^2	27^2	61^2	28^2
$m_T(\mu,\nu)$		61^2	27^2	59^2	28^2	59^2
$p_T(e)$			75^2	35^2	51^2	32^2
$p_T(\mu)$				77^2	32^2	53^2
$\not{p}_T\,(e)$					81^2	43^2
$\not{p}_T\,(\mu)$						81^2

TABLE XIII: The complete covariance matrix for the m_T, p_T, and $\not{p}_T$ fits in the electron and muon decay channels, in units of MeV^2. The matrix is symmetric.

Distribution	m_W (GeV)	χ^2/dof
$m_T(e,\nu)$	$80.493 \pm 0.048 \pm 0.039$	86/48
$p_T(e)$	$80.451 \pm 0.058 \pm 0.045$	63/62
$\not{p}_T\,(e)$	$80.473 \pm 0.057 \pm 0.054$	63/62
$m_T(\mu,\nu)$	$80.349 \pm 0.054 \pm 0.027$	59/48
$p_T(\mu)$	$80.321 \pm 0.066 \pm 0.040$	72/62
$\not{p}_T\,(\mu)$	$80.396 \pm 0.066 \pm 0.046$	44/62

TABLE XII: The results of the fits for m_W to the m_T, p_T, and $\not{p}_T$ distributions in the electron and muon decay channels. The first uncertainty is statistical and the second is systematic.

χ^2 at least as large as this is 44%.

B. Cross-Checks

Figures 55-57 show the differences between data and simulation, divided by the statistical uncertainties on the predictions, for the m_T, p_T and $\not{p}_T$ distributions. Figures 58-60 show the variations

Correlation	$W \to \mu\nu$	$W \to e\nu$
$m_T - p_T$	70%	68%
$m_T - \not{p}_T$	72%	63%
$p_T - \not{p}_T$	38%	17%

TABLE XIV: The statistical correlations between the m_T, p_T, and $\not{p}_T$ fits in the electron and muon decay channels.
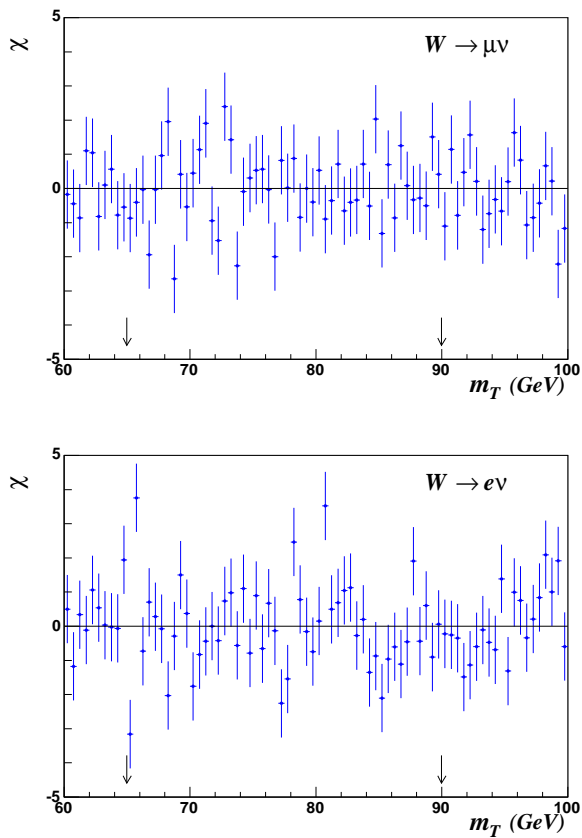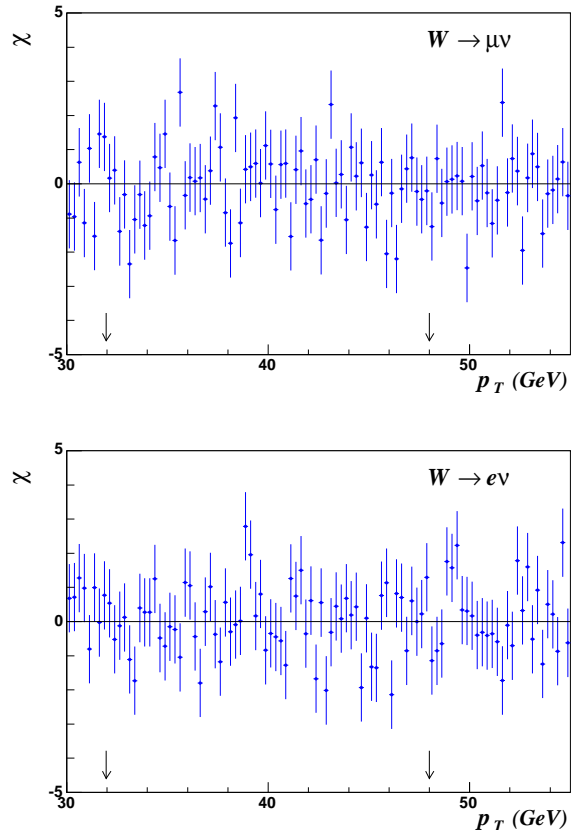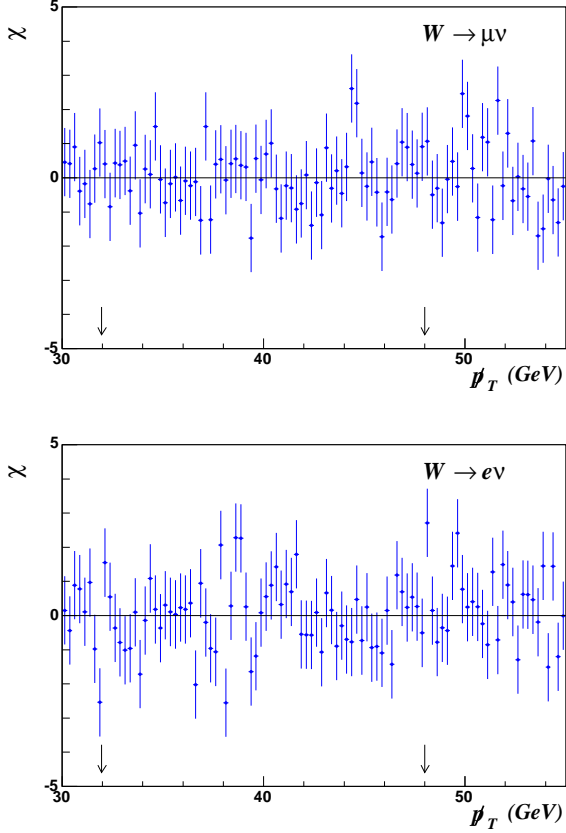

FIG. 55: The difference between the data and simulation, divided by the statistical uncertainty on the prediction, for the m_T distributions in the muon (top) and electron (bottom) channels. The arrows indicate the fit region.

of the fitted mass values, relative to the nominal results, as the fit regions are varied. These plots show variations consistent with statistical fluctuations.

The variation of the p_T fits with time, detector region, and lepton charge (Table XV) show no evidence of dependence on time or detector region. There is a difference between positive and negative lepton mass fits at the level of $\approx 2\sigma$ in each decay channel.

FIG. 56: The difference between the data and simulation, divided by the statistical uncertainty on the prediction, for the p_T distributions in the muon (top) and electron (bottom) channels. The arrows indicate the fit region.

The largest systematic uncertainty in this difference arises in the muon channel from the uncertainty on the alignment parameters a_0 and a_2 (Table III). The uncertainties on the mass difference due to these parameters are 49 MeV and 56 MeV, respectively, for a total uncertainty of 75 MeV. Any bias in these parameters affects the positive and negative lepton fits in opposite directions, and thus has a negligible net effect when the two are combined.

XI. SUMMARY

We have performed a measurement of the W boson mass using 200 pb^{-1} of data collected by the CDF II detector at $\sqrt{s} = 1.96$ TeV. From fits to m_T, p_T, and $\not{p}_T$ distributions of the $W \to \mu\nu$ and $W \to e\nu$ data

FIG. 57: The difference between the data and simulation, divided by the statistical uncertainty on the data points, for the $\not{p}_T$ distributions in the muon (top) and electron (bottom) channels. The arrows indicate the fit region.

Fit difference	$W \to \mu\nu$	$W \to e\nu$
$m_W(l^+) - m_W(l^-)$	286 ± 152	257 ± 117
$m_W(\phi_l > 0) - m_W(\phi_l < 0)$	0 ± 133	116 ± 117
$m_W(\text{Mar, 2002-Apr, 2003}) -$		
$m_W(\text{Apr, 2003-Sep, 2003})$	75 ± 135	-107 ± 117

TABLE XV: Differences of m_W in the p_T fits between positively and negatively charged leptons, leptons in the upper and lower halves of the detector, and early and late data. The units are MeV.

samples, we obtain

$$m_W = 80.413 \pm 0.048 \text{ GeV}, \qquad (50)$$

which is the single most precise determination of m_W to date. The uncertainty includes statistical and systematic contributions of 34 MeV each.
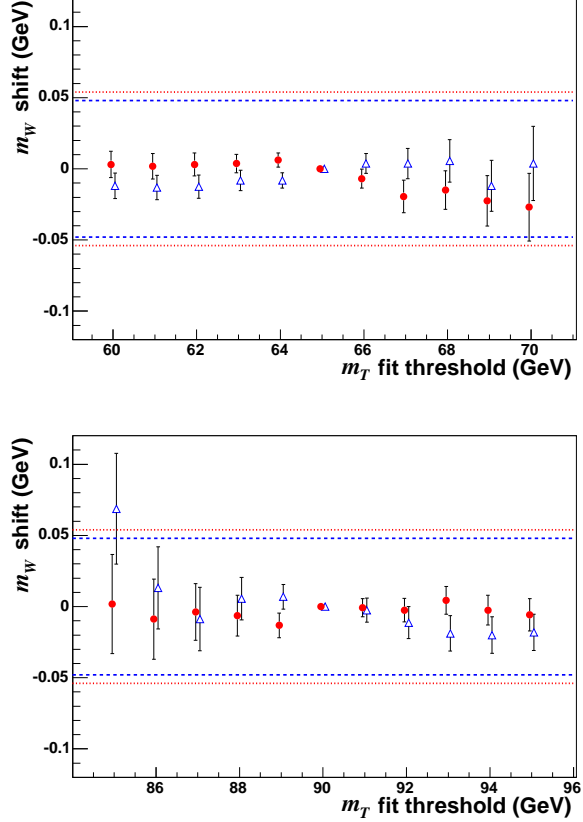
FIG. 58: The shifts in measured m_W for variations in the lower (top) and upper (bottom) edges of the m_T fit range. The electron channel is denoted by open triangles and the muon channel by solid circles. The error bars indicate the expected statistical variations from simulation pseudoexperiments. The dashed (dotted) lines indicate the statistical uncertainty on the m_W fit using the default fit range in the electron (muon) channel.

Combining this result with the Run I Tevatron measurements using the method in [76], we obtain a CDF Run I/II combined result of

$$m_W = 80.418 \pm 0.042 \text{ GeV}, \qquad (51)$$

and a combined Tevatron result of

$$m_W = 80.429 \pm 0.039 \text{ GeV}. \qquad (52)$$

In these combinations, we take the uncertainties due to PDFs and photon radiation to be fully correlated between our measurement and the previous Tevatron measurements. In the BLUE combination method [75], each uncertainty source contributes its covariance matrix, and all covariance matrices are summed
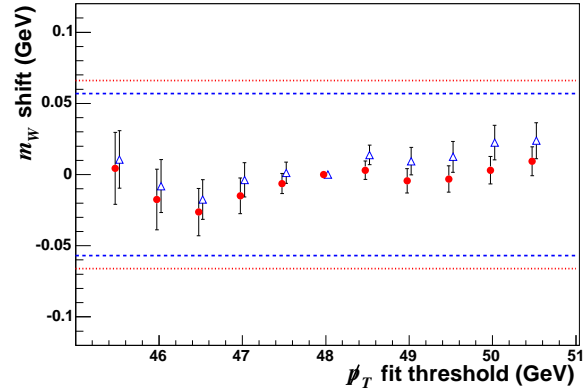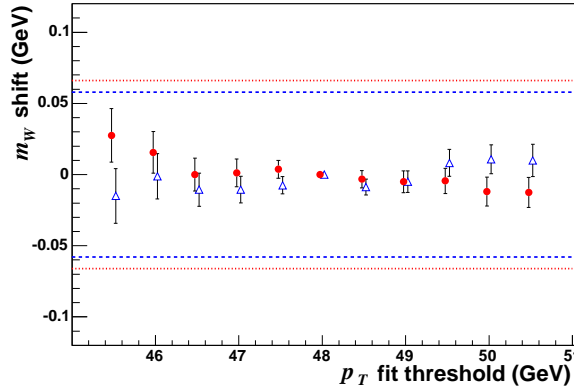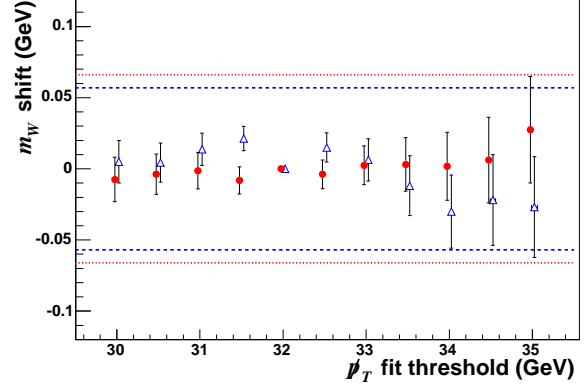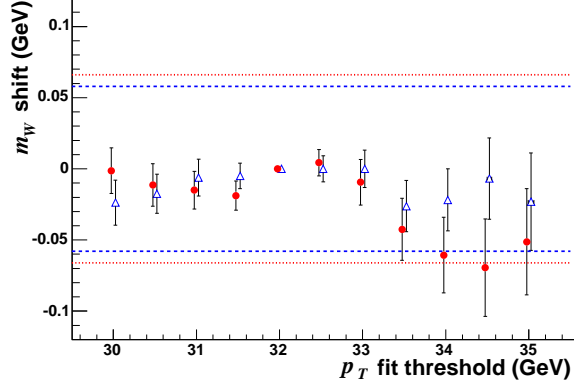
FIG. 59: The shifts in measured m_W for variations in the lower (top) and upper (bottom) edges of the p_T fit range. The electron channel is denoted by open triangles and the muon channel by solid circles. The error bars indicate the expected statistical variations from simulation pseudoexperiments. The dashed (dotted) lines indicate the statistical uncertainty on the m_W fit using the default fit range in the electron (muon) channel.

FIG. 60: The shifts in measured m_W for variations in the lower (top) and upper (bottom) edges of the $\not{p}_T$ fit range. The electron channel is denoted by open triangles and the muon channel by solid circles. The error bars indicate the expected statistical variations from simulation pseudoexperiments. The dashed (dotted) lines indicate the statistical uncertainty on the m_W fit using the default fit range in the electron (muon) channel.

to obtain the total covariance matrix. We evaluate an individual contribution to the uncertainty on our result by ignoring its respective covariance matrix and repeating the six-fold combination of our individual electron and muon channel m_T, p_T and $\not{p}_T$ fits. The difference in quadrature between the total uncertainty, including and excluding a given covariance matrix contribution, is taken to be the uncertainty due to that source. Following this procedure, we obtain the systematic uncertainty contributions due to PDFs and QED radiative corrections to be 12.6 MeV and 11.6 MeV respectively (Table XVI), for a combined uncertainty of 17.2 MeV.

Assuming no correlation between the Tevatron and LEP measurements, we obtain a new world average of

$$m_W = 80.398 \pm 0.025 \text{ GeV}. \qquad (53)$$

Our measurement reduces the world uncertainty to 31 parts in 10^5, and further constrains the properties of the Higgs boson and other new particles coupling to the W and Z bosons. Within the context of the standard model, fits made to high energy precision electroweak data in 2006 gave $m_H = 85^{+39}_{-28}$ GeV, with $m_H < 166$ GeV at the 95% confidence level [19]. The values used for the top quark and W boson masses in these fits were $m_t = (171.4 \pm 2.1)$ GeV and $m_W = (80.392 \pm 0.029)$ GeV, respectively. Updating these

52

Source	Uncertainty (MeV)
Lepton Scale	23.1
Lepton Resolution	4.4
Lepton Efficiency	1.7
Lepton Tower Removal	6.3
Recoil Energy Scale	8.3
Recoil Energy Resolution	9.6
Backgrounds	6.4
PDFs	12.6
W Boson p_T	3.9
Photon Radiation	11.6

TABLE XVI: Systematic uncertainties in units of MeV on the combination of the six fits in the electron and muon channels. Each uncertainty has been estimated by removing its covariance and repeating the six-fold combination.

fits with the most recent world average values of $m_t = (170.9 \pm 1.8)$ GeV and $m_W = (80.398 \pm 0.025)$ GeV [Eq. (53)], and using the methods and data described in [19] and [77], gives $m_H = 76^{+33}_{-24}$ GeV, with $m_H <$

144 GeV at the 95% confidence level. The effect of the new m_W value alone is to reduce the predicted value of the standard model Higgs boson mass by 6 GeV.

We anticipate a significant reduction in the uncertainty of future CDF m_W measurements using larger available data sets. The dominant uncertainties on this measurement are due to W boson statistics and to the lepton energy scale calibration (Table XVI), and will be reduced with increased statistics in the W boson and calibration data samples.

APPENDIX A: ELECTRON AND PHOTON INTERACTIONS

The simulation of electrons and photons (Section III B 2) uses the Bethe-Heitler differential cross sections for electron bremsstrahlung and photon conversion [48]. Defining y as the final state energy divided by the initial state energy, the bremsstrahlung cross section is:

$$\frac{d\sigma}{dy} = 4\alpha_{EM} r_e^2 \left[\left(\frac{4}{3y} - \frac{4}{3} + y \right) \psi_1(Z) + \left(\frac{1}{y} - 1 \right) \frac{\psi_2(Z)}{9} \right], \tag{A1}$$

where:

$$
\begin{aligned}
\psi_1(Z) &= Z^2[\ln(184.15 Z^{-1/3}) - f] + \\
&\quad Z \ln(1194 Z^{-2/3}), \\
\psi_2(Z) &= Z^2 + Z, \\
f &= a^2[(1+a^2)^{-1} + 0.20206 - 0.0369a^2 + \\
&\quad 0.0083a^4 - 0.002a^6],
\end{aligned} \tag{A2}
$$

and $a = \alpha_{EM} Z$. We define a material's radiation length X_0 according to [48]:

$$X_0^{-1} \equiv 4\alpha_{EM} r_e^2 N_A \rho \psi_1(Z)/A, \tag{A3}$$

where ρ is the density of the material. In terms of the radiation length, the cross section is

$$\frac{d\sigma}{dy} = \frac{A}{N_A X_0 \rho} \left[\left(\frac{4}{3} + C \right) \left(\frac{1}{y} - 1 \right) + y \right], \tag{A4}$$

where

$$C \equiv \frac{\psi_2(Z)/9}{\psi_1(Z)}. \tag{A5}$$

The conversion cross section takes a similar form, since the relevant Feynman diagram is a rotation of the bremsstrahlung process [48]:

$$\frac{d\sigma}{dy} = \frac{A}{N_A X_0 \rho} \left[1 - (4/3 + C)y(1-y) \right]. \tag{A6}$$

The Compton scattering cross section as a function of scattering angle is given by the Klein-Nishina formula [54]:

$$\frac{d\sigma}{d\Omega} = \frac{r_e^2}{2} \left[\frac{1 + \cos^2\theta}{[1 + k(1 - \cos\theta)]^2} + \frac{k^2(1 - \cos\theta)^2}{[1 + k(1 - \cos\theta)]^3} \right], \tag{A7}$$

where $k \equiv E_\gamma/m_e$. The scattering angle is kinematically related to the energy loss by [54]

$$y = k'/k = [1 + k(1 - \cos\theta)]^{-1}, \tag{A8}$$

where k' is the energy of the photon after scattering, in units of m_e. Using this equation, the differential cross section with respect to y can be written as [40]:

$$\frac{d\sigma}{dy} \propto 1/y + y, \tag{A9}$$

ignoring terms containing $1/k$.

ACKNOWLEDGMENTS

[1] G. Arnison *et al.* (UA1 Collaboration), Phys. Lett. B **122**, 103 (1983); M. Banner *et al.* (UA2 Collaboration), Phys. Lett. B **122**, 476 (1983); G. Arnison *et al.* (UA1 Collaboration), Phys. Lett. B **126**, 398 (1983); P. Bagnaia *et al.* (UA2 Collaboration), Phys. Lett. B **129**, 130 (1983).

[2] S. Glashow, Nucl. Phys. **22**, 579 (1961); S. Weinberg, Phys. Rev. Lett. **19**, 1264 (1967); A. Salam, *Elementary Particle Theory: Relativistic Groups and Analyticity (Nobel Symposium No. 8)*, edited by N. Svartholm (Almqvist and Wiksell, Stockholm), p. 367 (1968).

[3] W. J. Marciano, Phys. Rev. D **20**, 274 (1979); F. Antonelli, M. Consoli, and G. Corbo, Phys. Lett. B **91**, 90 (1980); M. Veltman, *ibid.*, 95 (1980).

[4] A. Sirlin, Phys. Rev. D **22**, 971 (1980).

[5] D. Acosta *et al.* (CDF Collaboration), submitted to Phys. Rev. Lett.

[6] D. C. Kennedy and B. W. Lynn, Nucl. Phys. **B322**, 1 (1989); M. B. Einhorn, D. R. T. Jones, and M. Veltman, Nucl. Phys. **B191**, 146 (1981).

[7] S. Heinemeyer *et al.*, J. High Energy Phys. **08**, 052 (2006).

[8] M. Awramik *et al.*, Phys. Rev. D **69**, 053006 (2004).

[9] E. Brubaker *et al.* (CDF and DØ Collaborations), hep-ex/0703034 (2007).

[10] H. Burkhardt and B. Pietrzyk, Phys. Rev. D **72**, 057501 (2005).

[11] W.-M. Yao *et al.*, J. Phys. G **33**, 1 (2006).

[12] S. Schael *et al.* (ALEPH Collaboration), Eur. Phys. J. C **47**, 309 (2006).

[13] G. Abbiendi *et al.* (OPAL Collaboration), Eur. Phys. J. C **45**, 307 (2006).

[14] P. Achard *et al.* (L3 Collaboration), Eur. Phys. J. C **45**, 569 (2006).

[15] J. Abdallah *et al.* (DELPHI Collaboration), submitted to Z. Phys. C.

[16] T. Affolder *et al.* (CDF Collaboration), Phys. Rev. D **64**, 052001 (2001).

[17] V. M. Abazov *et al.* (DØ Collaboration), Phys. Rev. D **66**, 012001 (2002); B. Abbott *et al.* (DØ Collaboration), Phys. Rev. D **58**, 092003 (1998).

[18] B. Abbott *et al.* (DØ Collaboration), Phys. Rev. D **62**, 092006 (2000).

[19] J. Alcarez *et al.* (LEP Collaborations), hep-ex/0612034 (2006).

[20] V. M. Abazov *et al.*, Phys. Rev. D **70**, 092008 (2004).

[21] O. Stelzer-Chilton, Ph. D. thesis, University of Toronto, Fermilab-Thesis-2005-71 (2005); I. Vollrath, Ph. D. thesis, University of Toronto, Fermilab-Thesis-2007-07 (2007).

[22] There is in principle a correlation due to final-state photon radiation and the W boson width, but these are sufficiently small that they are ignored when combining m_W measurements.

[23] A. D. Martin, R. G. Roberts, W. J. Stirling, and R. S. Thorne, Eur. Phys. J. C **28**, 455 (2003).

[24] J. Pumplin *et al.*, J. High Energy Phys. 0207, 012 (2002).

[25] P. Sutton, A. Martin, R. Roberts, and W. Stirling, Phys. Rev. D **45**, 2349 (1992); R. Rijken and W. van Neerven, Phys. Rev. D **51** 44 (1995); R. Harlander and W. Kilgore, Phys. Rev. Lett. **88**, 201801 (2002).

[26] A. Abulencia *et al.* (CDF Collaboration), hep-ex/0508029, submitted to J. Phys. G; D. Acosta *et al.* (CDF Collaboration), Phys. Rev. Lett. **94**, 091803 (2005).

[27] In order to obtain thesis results, two of the authors removed the blinding offset at two different points in the analysis. Access to these theses was denied to all authors outside of the University of Toronto.

[28] D. Acosta *et al.* (CDF Collaboration), Phys. Rev. D **71**, 032001 (2005);

[29] T. Affolder *et al.*, Nucl. Instrum. Methods Phys. Res. A **526**, 249 (2004).

[30] L. Balka *et al.*, Nucl. Instrum. Methods Phys. Res. A **267**, 272 (1988); K. Yasuoka *et al.*, Nucl. Instrum. Methods Phys. Res. A **267**, 315 (1988).

[31] S. Bertolucci *et al.*, Nucl. Instrum. Methods Phys. Res. A **267**, 301 (1988).

[32] M. Albrow *et al.*, Nucl. Instrum. Meth. Phys. Res. A **480**, 524 (2002); G. Apollinari *et al.*, Nucl. Instrum. Methods Phys. Res. A **412**, 515 (1998).

[33] G. Ascoli *et al.*, Nucl. Instrum. Methods Phys. Res. A **268**, 33 (1988).

[34] CDF Collaboration, Fermilab-Pub-96/390-E (1996).

[35] E. J. Thomson *et al.*, IEEE Trans. Nucl. Sc. **49**, 1063 (2002).

[36] For a small fraction of the data, only 10 hits out of 12 sense wires were required to create XFT segments.

[37] R. Downing *et al.*, Nucl. Instr. Methods Phys. Res. A **570**, 36 (2007).

[38] J. Elias *et al.*, Nucl. Instr. Methods Phys. Res. A **441**, 366 (2000).

[39] The underlying event refers to the spectator parton and additional inelastic $p\bar{p}$ interactions that produce low p_T particles roughly uniform in phase space.

[40] R. Brun and F. Carminati, CERN Program Library Long Writeup, W5013, 1993 (unpublished), version 3.15.

[41] E. Gerchtein and M. Paulini, physics/0306031 (2003).

[42] The map is divided into 333 longitudinal and 120-1000 azimuthal sections, with the number of azimuthal sections increasing as radius increases.

[43] G. R. Lynch and O. I. Dahl, Nucl. Instrum. Methods Phys. Res. B **58**, 6 (1991).

[44] D. Attwood *et al.* (MuScat Collaboration), Nucl. Instrum. Methods Phys. Res. B **251**, 41 (2006).

[45] The radial distribution of the hits has a small impact on parameter resolution, with the importance depending on the parameter. We do not attempt to model the radial hit distribution.

[46] C. Hays *et al.*, Nucl. Instrum. Methods Phys. Res. A **538**, 249 (2005).

[47] D. Acosta *et al.* (CDF Collaboration), Phys. Rev. D **71**, 052003 (2005).

[48] Y.-S. Tsai, Rev. Mod. Phys. **46**, 815 (1974).

[49] Increasing y_0 from 10^{-4} to 10^{-3} has about a 50 MeV effect on the E/p calibration for electrons from W boson decays; reducing it to 5×10^{-5} has less than a 5 MeV effect.

[50] P. L. Anthony *et al.*, Phys. Rev. Lett. **76**, 3550 (1996).

[51] A. B. Migdal, Phys. Rev. **103**, 1811 (1956); L. D. Landau and I. J. Pomeranchuk, Dokl. Akad. Nauk. SSSR **92**, 535 (1953); **92**, 735 (1953).

[52] S. Klein, Rev. Mod. Phys. **71**, 1501 (1999).

[53] M. L. Ter-Mikaelian, Dokl. Akad. Nauk. SSSR **94**, 1033 (1954).

[54] J. S. Hubbell, H. Gimm, and I. Øverbø, J. Phys. Chem. Ref. Data **9**, 1023 (1980).

[55] Because the model of the width of the E/p peak depends on the model of the momentum resolution, there is a 0.13% systematic uncertainty on κ associated with the momentum resolution model.

[56] F. Abe *et al.* (CDF Collaboration), Phys. Rev. D **52**, 2624 (1995).

[57] A. V. Kotwal, H. K. Gerberich, and C. Hays, Nucl. Instrum. Methods Phys. Res. A **506**, 110 (2003).

[58] K. Hagiwara *et al.*, Phys. Rev. D **66**, 010001 (2002).

[59] T. Sjöstrand, Comput. Phys. Commun. **82**, 74 (1994). We used version 6.129 for W and Z production, version 6.136 for Υ production, and version 6.157 for J/ψ production.

[60] R. Kleiss *et al.*, CERN 89-08, vol. 3, 1989 (unpublished).

[61] F. Landry, R. Brock, P.M. Nadolsky, and C.-P. Yuan, Phys.Rev. D **67**, 073016 (2003); C. Balazs and C.-P. Yuan, Phys.Rev. D **56**, 5558 (1997); G.A. Ladinsky and C.-P. Yuan, Phys.Rev. D **50**, 4239 (1994).

[62] U. Baur, S. Keller, and D. Wackeroth, Phys. Rev. D **59**, 013002 (1998).

[63] We do not require the correction factor for the number of radiation lengths $(0.4 \pm 0.9)\%$ to be the same as that for the ionization energy loss $(-6 \pm 2)\%$ because of our assumption that copper cable needs to be added to the GEANT simulation to model the radial distribution of photon conversions. Since the bremsstrahlung and conversion cross sections scale as $X_0^{-1} \propto Z^2$ (Appendix A) and the ionization energy loss scales as Z (Section III B 1), the correction factors can be different if the type of material is incompletely known.

[64] The statistical significance of the slope in the Z boson sample is 0.5σ. Averaging with the W boson sample results in zero slope.

[65] B. Abbott *et al.* (DØ Collaboration), Phys. Rev. D **61**, 072001 (2000).

[66] C. Peterson, T. Rögnvaldsson, and L. Lönnblad, Comput. Phys. Commun. **81**, 185 (1994).

[67] V. N. Gribov and L. N. Lipatov, Sov. J. Nucl. Phys. **15**, 438 (1972); G. Altarelli and G. Parisi, Nucl. Phys. **B126**, 298 (1977); Y. L. Dokshitzer, Sov. Phys. JETP **46**, 641 (1977).

[68] J. M. Campbell, J. W. Huston, and W. J. Stirling, Rep. Prog. Phys. **70**, 89 (2007).

[69] J. C. Collins, D. Soper, and G. Sterman, Nucl. Phys. **B250**, 199 (1985).

[70] J. C. Collins and D. E. Soper, Phys. Rev. D **16**, 2219 (1977).

[71] E. Mirkes, Nucl. Phys. **B387**, 3 (1992).

[72] J. Strologas and S. Errede, Phys. Rev. D **73**, 052001 (2006).

[73] W. T. Giele, E. W. N. Glover, and D. A. Kosower, Nucl. Phys. **B403**, 633 (1993).

[74] C. M. Carloni Calame, G. Montagna, O. Nicrosini, and M. Treccani, Phys. Rev. D **69**, 037301 (2004).

[75] L. Lyons, D. Gibaut, and P. Clifford, Nucl. Instrum. Methods Phys. Res. A **270**, 110 (1988).

[76] V. M. Abazov *et al.* (CDF and DØ Collaborations), Phys. Rev. D **70**, 092008 (2004).

[77] P.B. Renton, Rep. Prog. Phys. **65**, 1271 (2002).